10-23-2020 9:30 AM

Chronic Neurological Impairment in Patients with Thrombotic Thrombocytopenic Purpura: Findings in Quantitative MRI

Jeffrey Hamilton, *The University of Western Ontario*

Supervisor: Huang, Susan S.H., *The University of Western Ontario*
Joint Supervisor: Thiessen, Jonathan D., *The University of Western Ontario*
A thesis submitted in partial fulfillment of the requirements for the Master of Science degree in Medical Biophysics

Abstract

Thrombotic thrombocytopenic purpura (TTP) is a life-threatening, microvascular blood disorder that affects approximately 5 people per million per year. The disorder is characterized by insufficient activity in ADAMTS13 (a disintegrin-like and metalloprotease with thrombospondin type 1 repeats 13), which is an important enzyme in hemostasis because it prevents thrombosis. Along with blood clotting, other predominant symptoms are fever, anaemia, kidney failure, and neurological changes. Neurological changes may include confusion and decreased levels of consciousness, as well as depression and increased risk of seizures or stroke. However, little is known about the general pathology of these neurological changes and this forms the motivation for this research. An observational study using a comprehensive MRI protocol was evaluated in 13 patients and compared to results from assessments of depression and cognition. Despite prolonged remission, there is evidence of persistent neurocognitive decline as manifested in higher scores of depression and widespread white matter lesions.

Keywords: thrombotic thrombocytopenic purpura, atypical haemolytic uremic syndrome, chronic neurological impairment, human brain imaging, quantitative magnetic resonance imaging, myelin water fraction, white matter

Résumé

Le purpura thrombotique thrombocytopénique (PTT) est une maladie du sang microvasculaire potentiellement mortelle qui affecte environ 5 personnes par million par an. La maladie est caractérisée par une activité insuffisante d'ADAMTS13 (*a disintegrin-like and metalloprotease with thrombospondin type 1 repeats 13*), qui est une enzyme importante dans l'hémostase parce qu'elle prévient la thrombose. Outre que la coagulation sanguine, d'autres symptômes prédominants sont la fièvre, l'anémie, l'insuffisance rénale et les changements neurologiques. Les changements neurologiques peuvent inclure de la confusion et une diminution des niveaux de conscience, ainsi que la dépression et un risque accru de convulsions ou d'accident vasculaire cérébral. Cependant, la pathologie générale de ces changements neurologiques est mal comprise, donc c'est la motivation de cette recherche. Une étude observationnelle utilisant un protocole IRM approfondi a été évaluée chez 13 patients et comparée aux résultats d'évaluations de la dépression et de la cognition. Malgré une rémission prolongée, il existe des preuves d'un déclin neurocognitif persistant qui se manifeste par des scores plus élevés de dépression et des lésions répandues de la substance blanche.

Mots-clés : purpura thrombotique thrombocytopénique, syndrome hémolytique et urémique atypique, atteinte neurologique chronique, imagerie cérébrale humaine, imagerie par résonance magnétique quantitative, myéline, substance blanche

Lay Summary

This project is driven by the poorly-understood neurological findings in the rare, life-threatening blood disorder called thrombotic thrombocytopenic purpura (TTP). The disorder is manifested by spontaneous blood clotting throughout the body. Other symptoms include fever and kidney failure. Furthermore, neurological impairment has been well-documented in the literature, but few studies have thoroughly investigated how the brain is affected as a result of TTP. Neurological impairment includes increased risk of having a stroke or a seizure, as well as depression and confusion. These persist despite the the most effective treatments.

This is an observational study to evaluate brain health over time in patients at various stages of the disorder from soon-after their first episode to remission to several years without relapse. The following thesis presents results from 13 patients at the first timepoint. Primary testing was conducted through a comprehensive, 65-minute magnetic resonance imaging (MRI) protocol. MRI is a widely-used imaging modality that offers great flexibility in the types of images that can be acquired. The acquistion includes five qualitative sequences, which are viewed by a neuroradiologist, and three novel, quantitative sequences. The principle quantitative imaging sequence in this thesis is called myelin water imaging (MWI). It is a technique to quantify myelin, one of the characteristic features of white matter. Secondary testing is conducted through online cognitive testing and a depression assessment completed in a clinical interview with a nurse. Both were completed as close to the date of the MRI scan as possible.

The objective of this thesis is to show and explain the differences between and within brains of patients with TTP using both qualitative MRI and MWI to quantify changes in brain white matter. Even though the sample size is small and there are no controls at this point in the longitudinal study, several interesting results are reported which help elucidate the poorly understood long-term impact of thrombotic thrombocytopenic purpura. These include higher scores of depression and widespread white matter damage.

Acknowledgments

None of this work would be possible without the support and guidance of the large research team I am fortunate to have been part of over the last two years. This primarily includes my supervisors, Dr. Jonathan Thiessen and Dr. Susan Huang, who have been strong mentors for my scientific pursuits in graduate school. I came to Western for the unparalleled opportunities in exciting clinical research where I could contribute to an original brain imaging study and be involved with the patients for which the research is ultimately for. My experiences exceeded my expectations. In addition to my supervisors, I give thanks to my advisory committee members, Dr. Jean Théberge and Dr. Jennifer Mandzia; my past and present lab members, particularly Rick Sugden who was pivotal in developing our analysis workflow; and our clinical collaborators, including Kerri Gallo and Dr. Michael Jurkiewicz, with whom I thoroughly enjoyed my clinical days. Furthermore, our imaging technicians, John Butler and Heather Biernaski, turn our ideas to reality and I am grateful for their constant collaboration throughout this research. Most importantly, I extend my gratitude to my parents and sisters, who have been here for me every step of the way.

For Mom and Dad,

Both my number one

Contents

List of Figures

List of Tables

List of Abbreviations

ADAMTS13 a disintegrin-like and metalloprotease with thrombospondin type 1 repeats 13

ADC apparent diffusion coefficient

aHUS atypical haemolytic uremic syndrome

ANOVA analysis of variance

ASL arterial spin labeling

BBB blood brain barrier

BBB-P blood brain barrier permeability

bSSFP balanced steady-state free precession

CBF cerebral blood flow

CBS Cambridge Brain Sciences

CSF cerebrospinal fluid

CTP computed tomography perfusion

DESPOT1 driven equilibrium single pulse observation of T_1

DESPOT2 driven equilibrium single pulse observation of T_2

DICOM digital imaging and communications in medicine

DTI diffusion tensor imaging

DWI diffusion-weighted imaging

FA flip angle

FA fractional anisotropy

FOV field of view

FSL FMRIB Software Library

GM grey matter

HUS haemolytic uremic syndrome

LDH lactate dehydrogenase

MADRS Montgomery-Åsberg Depression Rating Scale

MAHA microangiopathic haemolytic anaemia

mcDESPOT multicomponent driven equilibrium single pulse observation of T_1 and T_2

MPRAGE magnetization-prepared rapid gradient echo

MRI magnetic resonance imaging

MWF myelin water fraction

MWI myelin water imaging

NIfTI neuroimaging informatics technology initiative

PLEX plasma exchange

QUIT Quantitative Imaging Tools

RESOLVE readout segmentation of long variable echo trains

RF radiofrequency

ROI region of interest

SPGR spoiled gradient recalled echo

SWI susceptibility-weighted imaging

T2FLAIR T_2-weighted fluid-attenuated inversion recovery

T_2 transverse relaxation time constant

T_1 longitudinal relaxation time constant

TE echo time

TI inversion time

TMA thrombotic microangiopathy

TOF MRA time-of-flight magnetic resonance angiography

TR repetition time

TTP thrombotic thrombocytopenic purpura

vWF von Willebrand factor

WM white matter

WMH white matter hyperintensity

Chapter 1

Introduction

1.1 Thrombotic Thrombocytopenic Purpura

Thrombotic thrombocytopenic purpura (TTP), first described in a case study by Moschcowitz in 1924 [1], is a rare, life-threatening blood disorder characterized by insufficient activity in *a disintegrin-like and metalloprotease with thrombospondin type 1 repeats 13* (ADAMTS13). This protein functions to prevent thrombosis, the process of blood clotting. Consequently, TTP results in spontaneous thrombosis throughout the microvasculature. Thrombocytes and fibrin strands obstruct blood flow, depriving downstream tissues of oxygen and other nutrients, leading to tissue damage and death. The disorder is a form of thrombotic microangiopathy (TMA), which is the manifestation of both microangiopathic haemolytic anaemia (MAHA), the destruction of red blood cells; and thrombocytopenia, abnormally low levels of platelets. TTP is a medical emergency and >90% of patients die without treatment within 30 days of diagnosis [2]. This section describes the presentation, management, and outcomes of TTP.

1.1.1 Epidemiology

TTP typically affects 5–10 people per million per year, however there is varying geographical incidence of 1–13 cases per million per year [3]. Women are affected approximately twice as

often as men [4]. Figure 1.1 shows the types of TTP, of which there are two: congenital TTP (also known as inherited TTP or Upshaw-Schulman syndrome) and immune-mediated TTP (also known as acquired TTP); which is secondary or idiopathic. Congenital TTP accounts for <5% of TTP cases [5] and it follows autosomal recessive inheritance for variant forms of the ADAMTS13-encoding gene. Multiple mutations and polymorphisms are responsible for impaired activity and decreased secretion of ADAMTS13 [6]. In a 2012 study by Moatti-Cohen *et al.* [7], 10 different mutations were seen in 10 patients. Congenital TTP onset varies from infancy to the sixth decade of life [8]. Immune-mediated TTP accounts for >95% of TTP cases [5] and occurs by autoantibody inhibition of ADAMTS13. These individuals have a normal ADAMTS13-encoding gene and the median age of diagnosis is 42 years [9]. Within cases of immune-mediated TTP, 30% are secondary and 70% are idiopathic [10]. Secondary TTP may be attributed to bone marrow transplantation [3], cancer [3], the use of non-steroidal anti-inflammatory drugs [11], pregnancy [7], human immunodeficiency virus (HIV) [4], or autoimmune diseases such as systemic lupus erythematosus [12]. Idiopathic TTP occurs independently from any explainable causes.

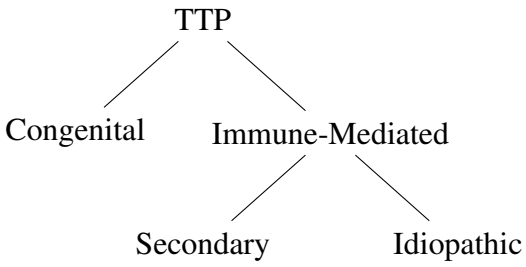

Figure 1.1: Types of TTP

1.1.2 Other Causes of Thrombotic Microangiopathy

The other quintessential presentation of TMA is haemolytic uremic syndrome (HUS). This disease primarily affects children and is often caused by gastrointestinal infection from the toxin-producing bacteria *Escherichia coli* O157:H7, [13, 14]. Another rare type of TMA is called

atypical HUS (aHUS), which occurs due to genetic mutation affecting the complement pathway [15]. Occasionally it is caused by an inhibitor to one of the complement regulators [16]. Unlike TTP, HUS and aHUS are presented with normal to moderately reduced ADAMTS13 activity [17]. Despite similar presentations of TMA, appropriate diagnosis is paramount because treatments differ. Patients with aHUS are included in this study.

1.1.3 Pathophysiology

To illustrate the unique and constitutive role of the immune system, Varela [18] said "the immune system is the body's brain". It provides protection against pathogens such as bacteria, parasites, and viruses. There are cells specific to rid these pathogens, which act in different stages depending on the severity of the threat. Autoimmune conditions occur when the body targets something from itself for destruction as if it is a pathogen. Almost all cases of TTP are immune-mediated and these cases are incurred by autoantibodies against ADAMTS13 [10, 19]. Immune-mediated TTP occurs from autoantibody inhibition of ADAMTS13 and congenital TTP occurs from mutated ADAMTS13 proteins. However, both types involve a mechanism with insufficient activity in ADAMTS13. The protein belongs to the ADAMTS protease family of enzymes which have key roles in inflammation, angiogenesis, and coagulation [20].

ADAMTS13, discovered in the late nineties [21, 22], is a constantly released protein necessary for maintaining hemostasis because it limits platelet aggregation and microthrombi formation. The protein-encoding exons are located on the long arm of chromosome 9 [23] and the resulting protein contains 1427 amino acids [8]. Synthesis occurs primarily in the liver [24] and there is evidence that it also takes place in endothelial cells [25]. Insufficient ADAMTS13 activity, due to mutated ADAMTS13 (congenital TTP) or autoantibody inhibition of ADAMTS13 (immune-mediated TTP), induces spontaneous clots throughout the microvasculature. These thrombocytes consume platelets and reduce platelet circulation in the blood, giving rise to thrombocytopenia. During an episode, the platelet count may be reduced by 70–90% [9]. The spreading of thrombi can affect the brain, kidneys, heart, and other major organs.

Figure 1.2[1] outlines a general mechanism of thrombosis in TTP [26]. There are approximately seven hundred proteins involved in hemostasis [27] and this depiction focuses on the key elements involved in TTP. One of the largest proteins in hemostasis is von Willebrand factor (vWF) which is released from endothelial cells to play a vital role in coagulation. Monomers of vWF spontaneously aggregate to form large multimers of up to 80+ monomers, known as ultra-large vWF, which trap platelets. The smaller multimers are unable to trap platelets. A protein on platelets called glycoprotein 1b is the binding site between the platelet and the vWF multimer. ADAMTS13 functions to cleave long chains of vWF between tyrosine 1605 and methionine 1606, in the A2 domain, to generate smaller multimers [26]. Without ADAMTS13, the peptide bond between these amino acids is inaccessible due to coverage within the core beta sheet. Insufficient ADAMTS13 activity permits long chains of vWF to grow and capture platelets. Blood clotting is an integral process for hemostasis in the presence of a vascular injury where ADAMTS13 is temporarily inhibited, specifically at the site of injury. In TTP, it is as if ADAMTS13 is perpetually inhibited and spontaneous, widespread clotting occurs.

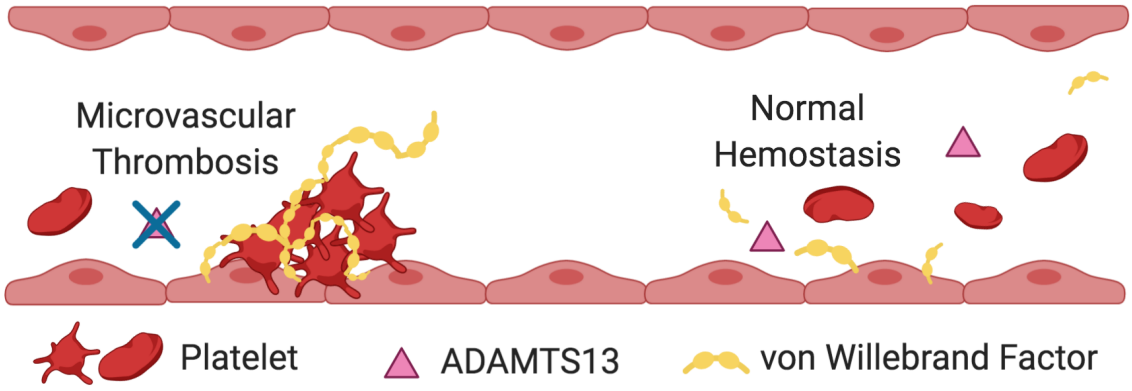

Figure 1.2: General mechanism of TTP. Microvascular thrombosis (left) occurs in congenital and immune-mediated TTP because large multimers of von Willebrand factor grow without being cleaved by ADAMTS13 [26]. Under normal hemostasis (right), ADAMTS13 cleaves von Willebrand factor and blood flow continues unimpeded [26].

[1]This original figure was produced using icons from BioRender.com.

1.1.4 Symptoms

TTP is presented in a multitude of ways and symptoms are broad due to the underlying pathophysiology influencing the circulatory, cardiovascular, and nervous systems. Impacts on the gastrointestinal and musculoskeletal systems occur but they are less common. Symptoms are initially non-specific, including fever or flu. However, they eventually become bleeding-related, such as thrombocytopenia and purple rashes known as purpura, leading to renal failure [28], stroke [29], and cardiac involvement such as heart attack [30, 31]. Non-specific symptoms include pallor, jaundice, and fatigue. Symptoms are similar in patients of all ages [32].

The Classic Pentad

TTP has been identified by five predominant symptoms, known as the classic pentad: fever, MAHA, renal failure, thrombocytopenia, and neurological findings. However, not all are required for the diagnosis and it is rare for patients to have all five symptoms [22]. Accordingly, this classification may provide guidance towards a diagnosis, but is not conclusive and may be misleading. Low ADAMTS13 with appropriate clinical presentation will help with clinical diagnosis. It is more important to identify how each patient is uniquely presenting TTP, addressing individual symptoms as they pertain to the kidneys, heart, or brain.

Neurological Impairment

Spontaneous, widespread thrombosis affects blood flow to the brain; resulting in headaches, confusion, and disturbed vision [33]. Additionally, brain scans may indicate swelling [28] and seizures [34] may occur. The increased risk of stroke in patients with TTP is associated with lower ADAMTS13 activity [29] and across all brain-related symptoms, memory is perhaps most affected [35]. Depression and cognitive deficits are present in two thirds of patients [36]. The timing for the onset of neurological impairment varies. These manifestations continue long term and they are poorly understood.

1.1.5 Diagnosis

TTP is a clinical diagnosis. Bruising and neurological symptoms may be the initial signs, though due to the rarity of the disorder, and despite potential evidence from available blood tests, the diagnosis of TTP may initially be overlooked. TTP masquerades as stroke [37, 38] and may be misdiagnosed as another typical presentation of TMA, aHUS. The hallmark identifier of TTP is insufficient ADAMTS13 activity. Consequently, blood tests and measurements of ADAMTS13 activity are required to confirm the diagnosis.

Blood Tests

There are a variety of blood biomarkers that may be indicative of TTP. The presence of fragmented red blood cells, known as schistocytes, in a blood film indicates MAHA. Red blood cells are sheared by the web of long monomers of vWF with platelets, depicted in microvascular thrombosis in Figure 1.2. Creatinine and urea in the blood are indicators of renal function and they are elevated. Lactate dehydrogenase (LDH), an enzyme which turns glucose into energy, is elevated. This indicates tissue breakdown. The concentration of haemoglobin the blood, normally 125–170 g/L for males and 115–155 g/dL for females [41, 39], is decreased [40]. Platelet count is normally 150–450$\times 10^9$ platelets/L [42] and thrombocytopenia is defined by a count <150$\times 10^9$ platelets/L. Page *et al.* [40] reported median platelet counts during an episode of 9$\times 10^9$ platelets/L in patients with no inhibitor (range 4–101), and 11$\times 10^9$ platelets/L in patients with a strong inhibitor (range 5–63).

Although these results in blood tests are indicative of TTP, they are not conclusive to establish the diagnosis. TTP is the presentation of MAHA and thrombocytopenia, excluding other diagnoses, with low levels of the vWF-cleaving protease, ADAMTS13. Consequently, the hallmark identifier of ADAMTS13 must be evaluated, by measuring ADAMTS13 activity and measuring the inhibitor, to conclude the diagnosis of TTP.

Measuring ADAMTS13

TTP is diagnosed for activity of ADAMTS13 <10% of normal [43]. The assessment is dependent on the assay, where ADAMTS13 activity ranges from 50–160% within healthy individuals [44]. After low ADAMTS13 activity is detected, the presence of anti-ADAMTS13 autoantibodies may be established. The presence of this inhibitor distinguishes immune-mediated TTP from congenital TTP and states of endothelial cell dysfunction [8].

ADAMTS13 activity may be measured directly or indirectly. Direct activity is measured by detecting vWF cleavage products. The approaches include gel electrophoresis followed by a Western blot [44] and fluorescence resonance energy transfer (FRET) involving a chemically modified A2 domain of vWF [45]. Indirect activity is measured by detecting the A2 domain of vWF cleave products. The approaches include collagen binding assays and functional enzyme-linked immunosorbent assays (ELISA) [46].

Anti-ADAMTS13 autoantibodies act in two processes. Neutralizing autoantibodies inhibit ADAMTS13 activity by binding to the functional regions and non-neutralizing autoantibodies accelerate the clearance of ADAMTS13. The measurement involves clearing ADAMTS13 and then detecting it with Western blot [47] or ELISA [48]. The autoantibody may be low or undetectable in acute phase [48].

Denaturing reagents used in tests may affect the activity measurements. Furthermore, these tests are performed under static conditions and are not necessarily representative of *in vivo* activity. It is important to measure ADAMTS13 and anti-ADAMTS13 autoantibodies prior to intervention because treatments aim to restore hemostasis by introducing and maintaining healthy levels of ADAMTS13.

1.1.6 Management

TTP is a medical emergency and >90% of patients die without treatment within 30 days of diagnosis [2]. It is often presented acutely and it must be treated quickly because symptoms worsen without appropriate intervention. The standard treatment for both types of TTP be-

gins with plasma exchange therapy (PLEX) [49]. Novel approaches including the emerging treatment of recombinant ADAMTS13 [50] show promising results for maintaining healthy ADAMTS13 levels in congenital and acquired TTP. The timing of treatment varies between patients and facilities. Similarly, the timing of follow-up appointments vary. If patients feel unwell between scheduled follow-ups, they are directed to get a blood test. Low ADAMTS13 levels are predictive of relapse.

TTP and aHUS involve thrombocytopenia; renal failure; and neurological complications including confusion, seizures, or stroke [51]. However, they differ in mechanism, as outlined in subsection 1.1.2 and subsection 1.1.3, and these life-threaning conditions require different interventions. The common treatment for aHUS is a drug called eculizumab [51]. Relapses in aHUS are common and careful monitoring is required.

Congenital TTP

Autosomal recessive inheritance for mutated ADAMTS13 protein-encoding genes results in ADAMTS13 proteins unable to cleave vWF multimers. Intervention aims to introduce functioning ADAMTS13 from donor plasma to restore hemostasis through PLEX with plasma-derived factor VIII containing normal ADAMTS13 [52]. Initial acute TTP episodes in congenital TTP patients are treated with plasma exchange where there is the added benefit of the removal of ultra-large vWF multimers. However, these patients are prone to relapse and require lifelong plasma infusion as maintenance therapy

Immune-Mediated TTP

Providing the blood with functioning ADAMTS13 may not work in immune-mediated TTP as the only treatment. PLEX restores hemostasis however the patients continue to produce ADAMTS13 autoantibodies. The added benefit of PLEX over plasma infusion is the removal of ultra-large vWF multimers and autoantibodies present in the blood. If the patient does not respond to PLEX or various drug interventions, the spleen may be surgically removed as a

rescue therapy. However, this is a seldom used therapy due to management improvement in the recent era. With the availability of rituximab, the relapsing rate has significantly reduced [53]. Strokes from TTP can be successfully treated with thombolytic therapy, however it is not a standard approach [54]. Treatment for immune-mediated TTP typically includes rituximab, steroids, and PLEX.

Drugs suppress the immune system to slow ADAMTS13 autoantibodies. Glucocorticoids, a class of corticosteroids, such as prednisolone [55] are used to reduce inflammatory activity. Chemotherapy drugs such as cyclophosphamide [56], vincristine [57], and bortezomib [58] may also be used. Immunosuppressants, such as rituximab [53] and cyclosporine A [59], are preferred over chemothearpy drugs. Rixuximab is an anti-CD20 monoclonal antibody that depletes B-lineage cells to prevent autoantibody activity and cyclosporine A is a calcineurin inhibitor. Though cyclosporine A is an option, it is not used as much because its relapse rates are higher than rituximab [60]. Caplacizumab, an anitbody to the A1 domain of vWF, has been demonstrated to increase the platelet recovery much sooner and reduce the PLEX sessions during acute episodes [61, 62].

1.1.7 Outcomes

Persistent low ADAMTS13 and/or detectable ADAMTS13 autoantibodies are associated with higher rate of relapse. Relapses typically occur within 1–2 years after the initial episode, though up to 30 years have been reported, and they occur in 30–50% of patients [63]. Careful monitoring is required. Remission is typically defined by normalization of platelets, normalization of LDH, and lack of clinical signs of microvascular injury for 30 days. The use of glucocorticoids and rituximab has been the potential reason for a decrease in plasma exchange therapy (PLEX) related major complications [64]. However, up to 20% of patients die despite the best of treatment [10]. Quality of life is affected following TTP as patients get tired more easily and deal with persistent neurological complications that may be related to cognitive decline and changes in the blood brain barrier.

Cognitive Decline

Neurological complications are common throughout all cases of TTP, acute and chronic. These include depression, confusion, headaches, and an increased risk of stroke and seizure. However, there is a dearth of research that focuses on brain imaging of such complications. A magnetic resonance imaging (MRI) study from 1999 [33] reveals similar pathology to stroke. This agrees with findings in case studies from 2006 [37] and 2019 [38]. However, despite decades of improvement in management, TTP still masquerades as stroke, which can lead to patient death. Preliminary work at our site investigated the central nervous system of patients with TTP using computed tomography perfusion (CTP) imaging.

Blood Brain Barrier Permeability

A preliminary investigation using CTP evaluated cerebral blood flow (CBF) and blood brain barrier permeability (BBB-P) using a 256-slice dynamic CT acquisition (GE Discovery RCT, Chicago, USA) and an iodinated contrast agent [65]. The brain-time density curves were analyzed with the Johnson-Wilson-Lee model to measure CBF and BBB-P [66]. Across 8 patients in hematological remission, CBF was measured with mean 50.19 ± 3.53 mL/100g/min. This is comparable to CBF in healthy brains [67]. Interestingly, permeability surface area-product, a measure of BBB-P, across these 8 patients was measured with mean 0.63 ± 0.25 mL/100g/min. A healthy brain does not permit the permeability of the contrast agent so a value of 0 mL/100g/min is expected [68]. These findings suggest a compromised blood brain barrier in TTP despite normal blood flow throughout the brain. The primary consequence of a compromised BBB is neuroinflammation [69]. Research and clinical findings suggest that vascular injury leads to stress on the circulatory system which compromises the BBB, leading to neuroinflammation [70, 71]. In turn, neuroinflammation can lead to widespread changes in the brain, including altered white matter integrity. This thesis focuses on the neurological outcomes of this progression including the changes in tissue and cognition.

1.1.8 Study Motivation

Management involving plasma exchange therapy and certain drugs improve the devastating outcomes of TTP. However, neurological changes persist despite these treatments and there is little research that documents how TTP affects the brain. Preliminary work using CTP, demonstrating a compromised blood brain barrier despite healthy cerebral blood flow, motivated a comprehensive observational study using MRI in addition to the assessment of depression and cognition. Importantly, MRI allows us to acquire a variety of image contrasts and quantitative measures that relate to white matter integrity. These approaches aim to elucidate how TTP affects the brain in prolonged remission. The following section introduces MRI and how it applies to this research project.

1.2 Magnetic Resonance Imaging

MRI was first documented in 1973 by Lauterbur [72] and the first image in a human was reported in 1977 by Hinshaw *et al.* [73]. MRI has since become an indispensable and ubiquitous tool in modern science and medicine. It is a widely available modality that is non-invasive and does not require the use of contrast agents or ionizing radiation. MRI is a powerful tool for imaging the brain, with a wide variety of tissue-dependent image contrasts and excellent spatial resolution. In the scope of this research, MRI can provide valuable insight into the impact of TTP on the brain.

1.2.1 Principles of MRI

The magnetic field, B_0, runs through the bore of the scanner and parallel to the floor. A radiofrequency (RF) field, B_1, is applied perpendicular to the magnetic field and used to generate signal in MRI. To understand how images are produced; the concepts of spin, signal, and pulse sequence parameters must be discussed. We begin with some definitions and notation.

Spin

Nuclei with spin-$\frac{1}{2}$ (or odd multiples of $\frac{1}{2}$) are susceptible to a magnetic field due to their inherent paramagnetism or diamagnetism. Hydrogen nuclei (^{1}H) are diamagnetic, spin-$\frac{1}{2}$ atoms with one proton and one electron, which exist as 99.99% of hydrogen isotopes. They are traditionally chosen as the nuclei of excitation in MRI because of their abundance in the human body. Hydrogen is predominantly found in water and fat where the body is about 60% water and 25% fat. Hydrogen nuclei are like little bar magnets in that they possess a magnetic moment (μ) (Equation 1.1) and the nuclei rotate about the axis of the dipole with quantized angular momentum (Figure 1.3a). The magnetic moment is determined by the gyromagnetic ratio (γ) and Planck's constant ($\hbar$). The gyromagnetic ratio of the nuclei and external magnetic field strength (B_0), measured in Tesla (T), determine the angular precessional frequency (ω), known as the Larmor frequency, of the nuclei (Equation 1.2).

$$\mu = \gamma \times \frac{\hbar}{2} \tag{1.1}$$

$$\omega = \gamma \times B_0 \tag{1.2}$$

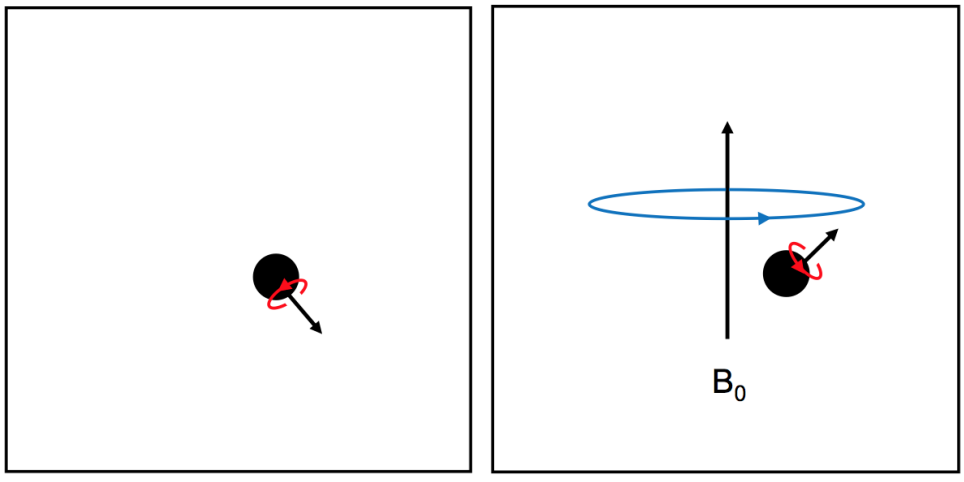

(a) No external field (b) External field

Figure 1.3: Single proton with and without an external magnetic field

The gyromagnetic ratio is unique to each species of nuclei and it is 42.58 MHz/T for hydrogen. Thus, the Larmor frequency of hydrogen at 3T is 127.74 MHz. This is the frequency in which hydrodgen nuclei precess about B_0 (Figure 1.3b).

In the absence of an external magnetic field, the dipoles point in random directions. The net magnetization (M_0), the vector sum of the magnetization of each nuclei, is zero. The magnet of the MRI scanner introduces an external magnetic field. When hydrogen nuclei are in the magnetic field, the net magnetization is in the direction of the MRI magnetic field B_0. Nuclei align parallel or antiparallel to B_0 at nearly equal proportions, although the much larger thermal energy of molecules ensures that most spins are randomly oriented. The slight preference for parallel alignment, on the order of 10 parts per million at 3T, results in a small M_0 in the direction of B_0. The magnetization vector precesses about the B_0 axis at the Larmor frequency.

Signal

An RF excitation pulse applied at the Larmor frequency tips the magnetization vector into the transverse plane, which is perpendicular to B_0. When the RF pulse is turned off, there is a return to the equilibrium of the magnetization vector to the direction of B_0. A time changing magnetic field induces a time changing electric field which generates a current, detected as the signal in the receive coils. Magnetic field gradient pulses, applied during the application and detection of RF pulses, encodes the signal with phase and frequency information that depends on the spatial location of nuclei. After acquisition, the fast Fourier transform (FFT) produces an image in Cartesian space from an image in k-space which is described by the frequency-encoding and phase-encoding domains.

Pulse Sequence Parameters

In MRI, the combination and repetition of RF and gradient pulses to create an image is known as a pulse sequence. Unlike other widely used medical imaging techniques, the signal in MRI is arbitrary and depends on the pulse sequence parameters. Contrast in MRI is controlled by

modifying pulse sequence parameters used to acquire an image. Repetition time (TR) is the time between the first RF excitation pulses of a repeated pulse sequence, as multiple excitations are typically required to spatially encode the signals used to form an image. The echo time (TE) is the time between the first RF excitation pulse and the signal acquisition by the receive coil. Flip angle (FA) is the angle from the z-axis that an RF pulse flips the magnetization vector. With FA = 90°, the magnetization flips directly into the transverse plane. Three principle characteristics of the magnetization vector are longitudinal relaxation time (T_1), transverse relaxation time (T_2), and proton density (PD). In a spin echo image, TR and TE give a particular weighting to the resulting images (Table 1.1). For example, an image with contrast that is sensitive to underlying T_1 relaxation time is called a T_1-weighted image. Similarly, contrast in T_2-weighted images is sensitive to underlying T_2 relaxation times and PD-weighted images to proton densities. Despite their names, it is important to recognize that signal in T_1-, T_2-, and PD-weighted images is always a mixture of the underlying tissue-dependent magnetization vector characteristics.

	Short TR	Long TR
Short TE	T_1-weighted	PD-weighted
Long TE	*Poor contrast*	T_2-weighted

Table 1.1: Influence of acquisition parameters on the weighting of spin echo MRI. Long TR or TE means 3–5 $\times$ T_1 or T_2 and short TR or TE means much less than the T_1 or T_2.

1.2.2 Relaxometry

In MRI, contrast from T_1- and T_2-weighted images is used to visualize differences between tissue and to assess anatomy and pathology. However, T_1- and T_2-weighted images are fundamentally qualitative and depend on the chosen pulse sequence parameters. A more quantitative measure of tissue characteristics would be measurements of T_1 and T_2 relaxation times. If the signal of a pulse sequence can be described as a function of TE, TR, and/or FA, then the underlying relaxation times can often be determined by varying the acquisition parameters and fitting to the signal equation. In this way, rather than T_1- and T_2-weighted images, T_1 and T_2

relaxation time maps can be generated. T_1 and T_2 are influenced by water content, magnetization exchange, and paramagnetic content such as iron [74]. Additionally, T_1 is sensitive to lipid, protein and macromolecule content as well as temperature and T_2 is sensitive to pH and tissue microstructure [74]. From the work of Stanisz, 2005 [74], Table 1.2 outlines T_1 and T_2 at 3T for white matter and grey matter, however, values may vary depending on the technique and scanner manufacturer [75]. The field strength will also influence these time constants.

Tissue	T_1	T_2
White Matter	1084	69
Grey Matter	1920	99

Table 1.2: Longitudinal and transverse relaxation time constants by tissue (ms) at 3T

Longitudinal Relaxation

Longitudinal relaxation is also known as spin-lattice relaxation. T_1 is the time it takes for the magnetization along the z-axis (M_z) to recover to approximately 63% ($1 - 1/e$) of M_0 after a 90° RF pulse. The general signal equation for M_z as a function of M_0, time, and T_1 is described by Equation 1.3. After the RF pulse, M_z returns to M_0 as the nuclei realign with B_0.

$$M_z = M_0(1 - e^{-t/T_1}) \tag{1.3}$$

Transverse Relaxation

Transverse relaxation is also known as spin-spin relaxation due to the interaction between nuclei. T_2 is the time it takes for the magnetization in the xy-plane (M_{xy}) to decay to approximately 37% ($1/e$) of M_0 after a 90° RF pulse. The general signal equation for M_{xy} as a function of M_0, time, and T_2 is described by Equation 1.4. M_{xy} goes to zero as magnetization disperses in the transverse plane.

$$M_{xy} = M_0 e^{-t/T_2} \tag{1.4}$$

1.2.3 Myelin Imaging with MRI

Unlike most biological membranes, which have a high ratio of proteins to lipids, the dry mass of myelin is 70–85% lipid and just 15–30% protein [76]. Myelin is the characteristic feature of white matter and is integral for brain function. It is the fatty tissue that wraps around axons of neurons throughout the nervous system to provide insulation of action potentials and help propagate signals. In the central nervous system, myelination is performed by oligodendrocytes; and in the peripheral nervous system, it is performed by Schwann cells. There is little myelination in grey matter. Brain function is affected by changes in myelin composition, which makes myelin an important biomarker. Along with T_1 and T_2, measurements of myelin content may be useful for diagnosis and management of white matter disease.

Myelin-Associated Diseases

The total volume of brain white matter increases until the middle of the fifth decade of life [77] and accelerated rates of atrophy occur beginning in the eighth decade of life [78]. Otherwise, changes in myelin are gradual. Accordingly, beyond the natural cycles of myelination and demyelination, persistent changes through one of the following three processes are indicative of disease.

Demyelination is the most common of the three processes. It is the loss of myelin and it is seen in dementia, mild cognitive impairment, multiple sclerosis (MS), and stroke. The breakdown of myelin varies with density of the beta amyloid peptide in dementia and mild cognitive impairmment [79]. MS involves demyelination among the pathological processes of chronic inflammation, edema, gliosis, oligodendrocyte loss, and axonal loss. Hypermyelination is the gain of myelin and this may include mis-myelinating diseases such as traumatic brain injury (TBI) and concussion [80]. Dysmyelination is the rarest of the three processes and these conditions are called leukodystrophies, such as metachromatic leukodystrophy [81], which involves a genetic predisposition.

It is not known how myelin changes in the brains of patients with TTP or if myelination

follows one of these three processes. Given the evidence of cognitive decline and compromised BBB, it is reasonable to predict that increased neuroinflammation may lead to demyelination and white matter disease in patients with TTP. Myelin water imaging (MWI) using MRI provides the opportunity to address these questions. The following subsection describes the theory of MWI before applying ideas from MRI throughout this section to the research project.

Myelin Water Imaging

Conventional MRI is not specific to myelin. The primary measurement in myelin water imaging is the myelin water fraction (MWF), which is the ratio of signal of protons in myelin water divided by sum of total signal from all protons in water throughout the voxel. In the brain, water is found in four primary compartments: cerebrospinal fluid (CSF), intracellular water, extracellular water, and the lipid bilayer. Even within a 1 mm isotropic voxel there may be different water compartments contributing to different behaviour of proton relaxation and the MWF teases out the contribution of myelin within the voxel. The compartments are illustrated in a hypothetical sub-voxel cross section in Figure 1.4 based on transmission electron microscopy from MacKay and Laule, 2016 [82]. Layers of myelin wrap around a single neuron, contributing nearly half of the radius of the full white matter neuronal cell.

MWI is an extension of relaxometry in that it utilizes the information from T_1 and T_2 individually or together to quantify myelin. There are four predominant approaches for MWI. The gold standard is multi-echo T_2 relaxation [83]. This relies on a multiple spin echo sequence consisting of a 90-degree RF pulse followed by a series of 180-degree RF pulses, with signal measured at the interleaved echo times (typically measured over 32 echoes). The resulting T_2 decay curve is the sum of exponential decays of different compartments. The T_2 of myelin water is assumed to be 10–40 ms and for intracellular and extracellular water it is assumed to be 40–200 ms. The T_2 components of myelin water and intracellular/extracellular water are fit to a multi-compartment version of the signal equation describing transverse relaxation in the previous subsection. Although accurate, scan times are typically long. The second approach

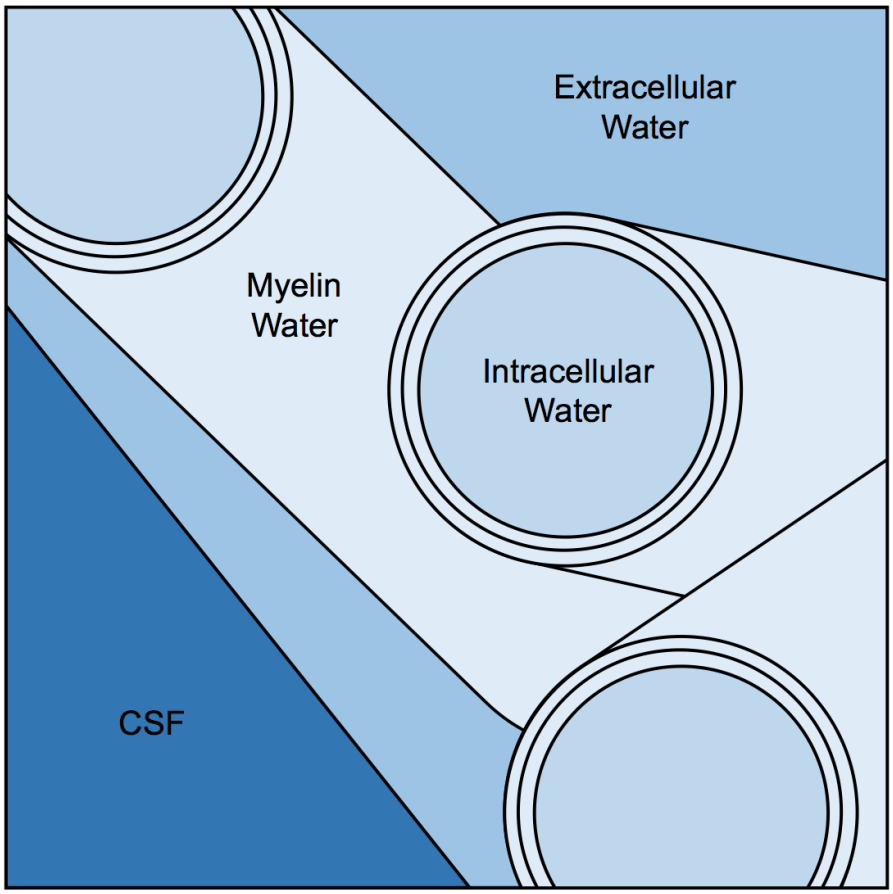

Figure 1.4: Four compartments of water in a hypothetical sub-voxel cross section

uses a gradient echo decay curve measurement of the T_2* decay curve. It is a similar approach to the first, however the T_2* decay curves are steeper [84]. The third approach focuses on T_1 acquisitions between components of T_1 of myelin assumed to be 150–200 ms and of intracellular/extracellular water assumed to be 1–1.5 s [85]. The final approach is the use of fast gradient echo incorporating information from both T_1 and T_2. This includes gradient and spin echo (GRASE), short transverse relaxation time component (ViSTa) [86, 87], and multi-component driven equilibrium single pulse observation of T_1 and T_2 (mcDESPOT) [88]. mcDESPOT has been shown to be a direct and specific method for measuring myelin [79], and was chosen to measure the T_1, T_2, and MWF in patients with TTP. Confounding factors in MWI include myelin debris and magnetization transfer. The magnetization in the tissue from spatially encoded RF excitation pulses does not necessarily remain in the targeted voxel, altering signal

detection in other voxels; and myelin debris in the extracellular space falsely increases the MWF estimate. Despite these potential confounds, MWF agrees with histologic myelin verified by Luxol fast blue (LBF) [89], making MWI a promising tool to better understand myelin integrity in patients with TTP.

1.3 Objectives

The central aim of this thesis is to report on how neurological changes persist despite treatment and prolonged remission in thrombotic microangiopathy. Patients with either TTP or aHUS are studied in this research project due to the rarity of each condition and to the similarities in the poorly understood neurological changes both conditions present. MRI is a non-invasive imaging modality with a wide variety of sequences for varying contrasts and measurements. Assessments of depression and cognition can be evaluated on the same day as the MRI scan.

The central aim is evaluated using the following three objectives:

1. Assess depression; cognition; and both qualitative and quantitative MRI findings
2. Compare the differences in these assessments between TTP and aHUS
3. Correlate the findings within patients between all measurements

1.4 Thesis Overview

Chapter 1 has introduced TTP and motivated a pilot study to observe the impact of TTP on the brain. Chapter 2 outlines the methodology: namely the assessments for depression and cognition; and the approaches in MRI, both qualitative and quantitative. Due to the rarity and similarities of the presentations of thrombotic microangiopathy, both patients with TTP and patients with aHUS are included in this study. Chapter 3 presents the respective results for each

methodology with separate sections addressing depression scores; cognitive scores; findings in qualitative MRI across five sequences; and measurements in quantitative MRI in longitudinal relaxation time (T_1), transverse relaxation time (T_2), and myelin water fraction. Additionally, there is a section focusing on the agreement between the results from each approach. Chapter 4 discusses the key findings of this thesis and describes the next steps for this research.

Chapter 2

Methods

2.1 Study Design

This is a multi-centre cohort observational study at London Health Sciences Centre (LHSC) including patients and healthy controls from: LHSC, London; University Health Network, Toronto; and St. Michael's Hospital, Toronto. The study was approved by the Western University Research Ethics Board (project ID: 108273). The work presented in this thesis focuses on findings in a small group of patients; predominantly from Southwestern Ontario; in relation to assessments of depression, cognitive testing, and a comprehensive MRI protocol.

Participants

A total of 13 patients (mean age 45.5 years; 5 male, 8 female) were recruited following their visit to the clinic: 9 have been diagnosed with thrombotic thrombocytopenic purpura (TTP) and 4 have been diagnosed with atypical haemolytic uremic syndrome (aHUS) (Table 2.1). Though treatment and pathology differs between these two microvascular conditions, neurocognitive outcomes are similar and are poorly understood. Patients with TTP or aHUS are typically seen by the same teams of healthcare professionals, which made it possible to recruit patients with either diagnosis.

Patient	Age	Sex	Diagnosis	Time
1	35	F	TTP	3 months
2	32	F	TTP	3 months
3	20	F	aHUS	10 months
4	58	M	TTP	3 years
5	60	M	TTP	15 years
6	51	F	TTP	9 months
7	64	M	TTP	6 months
8	23	F	TTP	10 months
9	73	M	aHUS	2 years
10	43	F	aHUS	2 years
11	48	F	TTP	17 years
12	28	F	TTP	4 months
13	47	M	aHUS	2 months

Table 2.1: Age (years), sex, diagnosis, and time by patient. Time (months or years) indicates the duration between the date of diagnosis and the date of the first MRI scan.

Participants were included based on the following criteria: adults over 18 years of age, diagnosis of idiopathic TTP or aHUS, plasma exchange treatment with or without other therapies, currently in remission, and meet all diagnostic criteria for idiopathic TTP or aHUS. Remission is defined by normalization of platelets and LDH with no clinical signs or symptoms of microvascular injury for more than 30 days. The diagnostic criteria for immune-mediated TTP is: thrombocytopenia, under 150×10^9 platelets/L; MAHA, evidenced by schistocytes on blood film; elevated LDH, 1.25 $\times$ upper limit of normal (approximately 190 units/L); and no other explainable causes. Participants were excluded based on the following criteria: diagnosis of HUS or disseminated intravascular coagulation; an abnormal internal normalized ratio at the time of presentation; malignant hypertension at the time of presentation; on following drugs within 90 days of presentation: ticlopidine, clopidogrel, mitomycin C, gemcitabine, cyclosporine A, or quinine; history of hematopoietic stem cell transplantation; history and/or diagnosis of vasculitis, systemic lupus erythematosus, scleroderma, rheumatoid arthritis, antiphospholipid antibody syndrome, or HIV/AIDS; history of solid-organ malignancy within 5 years of presentation such as lung, breast, gastric, colon, pancreatic, prostate, or liver; or pregnant.

Image analysis development was completed in three healthy volunteers (mean age 23 years, 3 male) between December 2018 and August 2019. The methodology was applied to the patient data while the results from the volunteers were excluded from the analysis. Patients were scanned between September 2019 and February 2020. The COVID-19 pandemic delayed the recruitment of controls and additional patients. Consequently, this thesis focuses on neurocognitive outcomes in patients with TTP or aHUS at the first timepoint in the longitudinal study.

Protocol

Figure 2.1[1] depicts the timeline of the study. At each timepoint patients complete: a clinical interview to evaluate depression, cognitive testing, and a comprehensive MRI scan. Detailed methodology for each of these aspects is described in the following sections. Statistical tests were evaluated using GraphPad Prism 8.4.3 (La Jolla, California, USA) considering a type I error rate of $\alpha = 0.05$. Computed tomography perfusion and echocardiography were also acquired on the same day as the MRI scan, but these results are not considered in this thesis.

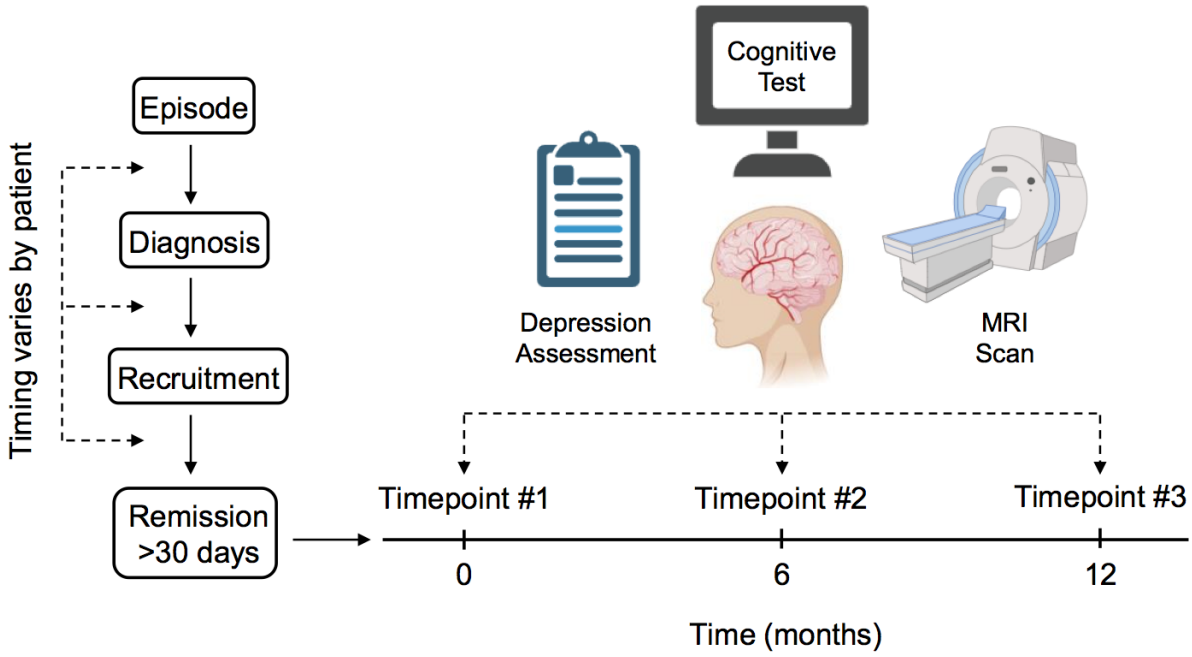

Figure 2.1: Protocol timeline

[1]This original figure was produced using icons from BioRender.com.

2.2 Depression Scoring

The standard rating scale for depression is the Hamilton Rating Scale, however the Montgomery-Åsberg Depression Rating Scale (MADRS) is more sensitive to changes from treatment [90]. A score of depression using the MADRS was assessed in a clinical interview within one week of the MRI scan. Ten assessments, each ranked on a scale from 0–6, comprise the MADRS, for a maximum potential score of 60. The ten assessments are: apparent sadness, reported sadness, inner tension, reduced sleep, reduced appetite, concentration difficulty, lassitude, inability to feel, pessimistic thoughts, and suicidal thoughts. This assessment incorporates answers from the perspectives of both the patient and the nurse. Typical thresholds for scores are: normal (0–6), mild depression (7–19), moderate depression (20–34), and severe depression (>34) [91].

Statistics

Welch's two-tailed t-tests were conducted to evaluate differences in depression score between male and female, and between patients with TTP and aHUS. Throughout the data analysis in this thesis, Welch's t-test was used where applicable over Student's t-test due to its robustness where fewer assumptions are made about the data. Furthermore, if the data meet the criterion for Student's t-test, Welch's t-test provides the same test statistic and P value [92]. A one-way Brown-Forsythe ANOVA was conducted on the mean score, over the ten assessments, between patients. Dunnett's T3 multiple comparisons test was conducted if $P < 0.05$. A one-way Brown-Forsythe ANOVA was conducted on mean score, over the 13 patients, between the ten assessments. Dunnett's T3 multiple comparisons test was conducted if $P < 0.05$. A chi-square test was conducted to evaluate the differences between the number of non-zero scores by assessment. Multiple comparisons test by Fisher's exact test was conducted using a Bonferroni correction if $P < 0.05$. Spearman's rank correlation was evaluated between depression score and other quantitative metrics.

2.3 Cognitive Testing

Cambridge Brain Sciences (CBS) [93] is a battery of 12 online cognitive tests to assess cognition across three domains: reasoning, memory, and verbal [94]. Respectively, these domains assess the user's cognitive abilities to problem solve, utilize short term memory, and understand language. The twelve tests are called: digit span, spatial span, grammatical reasoning, polygons, odd one out, rotations, spatial search, paired associates, feature match, double trouble, monkey ladder, and spatial planning. There are levels increasing in difficulty in each assessment: if the user is correct they move up a level, and if they are incorrect they move down a level. The user has three strikes before moving to next test. Users typically complete the testing in 40–60 minutes. Scores by test are compared to the database of >10,000 participants [93] to generate a percentile based on an age- and sex-matched healthy control comparison.

Statistics

Welch's two-tailed t-tests were conducted to evaluate differences in cumulative mean cognitive percentiles between male and female, and between patients with TTP and aHUS. A Student's t-test was conducted between the mean cognitive percentile of patients with the age-matched healthy population from the CBS database (mean 50 ± 34.1%). One-way ANOVA tests were conducted to evaluate differences between cognitive percentiles between patients, tests, and categories of tests. Tukey's multiple comparison test was conducted if $P < 0.05$. Spearman's rank correlation was evaluated between cognitive percentile and other quantitative metrics.

2.4 MRI Overview

A 3T MRI (Siemens Biograph mMR, Munich, Germany) was used with a 32-channel head-only receive coil to scan patients at St. Joseph's Hospital in London. The total acquisition time was 65 minutes and the breakdown of the imaging timeline is outlined in Figure 2.2. Including the setup time, where it is ensured that the patient feels comfortable, they are lying down in

the supine position for approximately 75 minutes. Details of the sequences are described in further detail in following sections. A continuous scan is paramount to reduce motion differences between sequences in the image analysis. Patients were given the opportunity to use a restroom prior to the scan and using the intercom, a technologist checked in with the patient every 5–10 minutes. All 13 patients completed the full MRI scan and all but one patient completed the scan without any pauses. Due to the lack of previous imaging in TTP and aHUS, and the similarities between these diseases and stroke; an MRI protocol to image stroke [95] was used as the foundation to select the sequences for the study. This protocol was enhanced to include three novel quantitative MRI techniques: myelin water imaging (MWI) using multi-component driven equilibrium single pulse observation of T_1 and T_2 (mcDESPOT); diffusion tensor imaging (DTI) using two-dimensional echo planar multi-directional diffusion weighted imaging (EP2D MDDW); and arterial spin labeling (ASL) using two-dimensional echo planar pseudo-continuous ASL (EP2D PCASL). MWI is used to quantity white matter myelin content by measuring the MWF, DTI is used to quantify the integrity of white matter by measuring the directionality and magnitude of water diffusion in tissue microstructure, and ASL is used to quantify cerebral blood flow. The results presented here pertain to those from the five qualitative sequences and MWI. Results from DTI and ASL are not presented, however they are mentioned in the discussion. No contrast agents were used and the images do not differ between sleeping and awake states. All images are presented throughout this thesis following standard radiology convention. Representative images, in the same planes of imaging, from the same healthy volunteer are shown throughout this chapter.

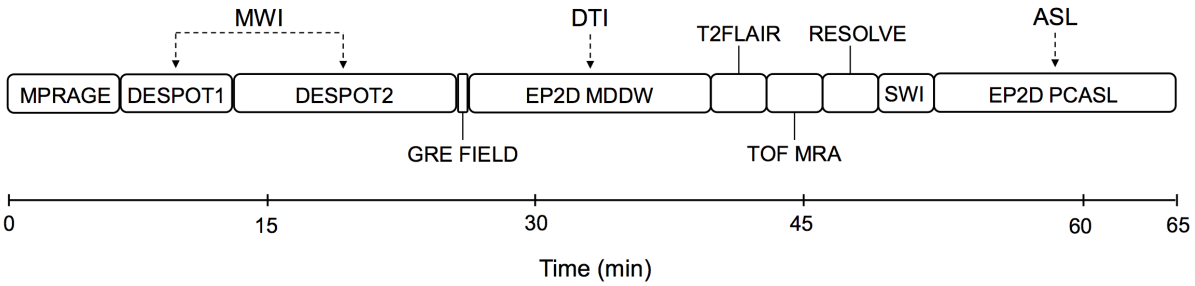

Figure 2.2: MRI acquisition timeline

2.5 Qualitative MRI

A single neuroradiologist was blinded to whether the dataset under review was of a patient or volunteer. They only knew the age of the individual. The five qualitative sequences were viewed on RadiAnt Viewer (Poznań, Poland) 1–2 times for each patient in the following order of sequences: T_1-weighted, diffusion-weighted, angiography, susceptibility-weighted, and T_2-weighted. The respective names for these sequences on Siemens scanners are: MPRAGE, RESOLVE, TOF MRA, SWI, and T2FLAIR. Sequence-specific parameters and representative images are described in the following five subsections. Signal intensity is relative and window level and window width are adjusted accordingly throughout the methods and results.

2.5.1 T_1-Weighted Imaging

A magnetization-prepared rapid acquisition with gradient echo (MPRAGE) sequence was acquired in the sagittal plane with TR = 2000 ms, TE = 4.18 ms, FA = 9°, TI = 900 ms, bandwidth = 150 Hz/pixel, and 1 mm isotropic voxel resolution. The field of view (FOV) includes the whole brain with 176 slices over 176 × 256 mm × 256 mm. MPRAGE is a T_1-weighted acquisition to assess general anatomy such as the detection of atrophy [96] and it is acquired in approximately 6 minutes. Representative images by plane are depicted in Figure 2.3.

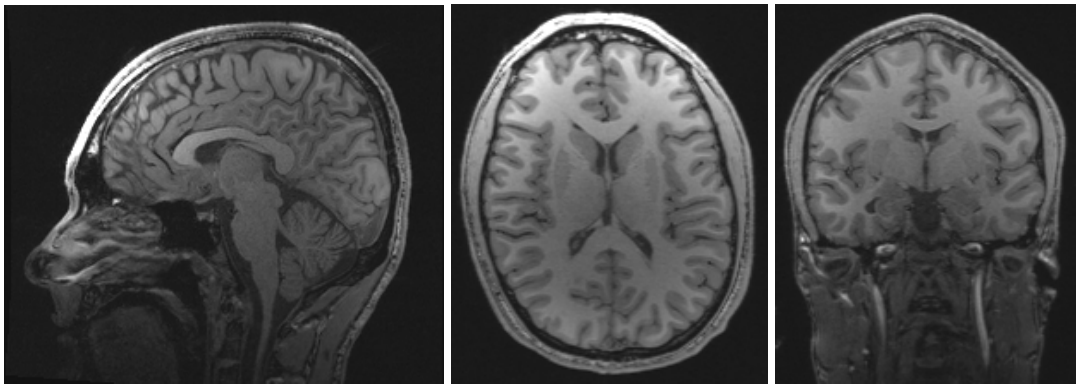

(a) Sagittal (b) Axial (c) Coronal

Figure 2.3: Representative T_1-weighted images of a healthy volunteer

2.5.2 Diffusion-Weighted Imaging

A readout segmentation of long variable echo trains (RESOLVE) sequence was acquired in the axial plane with TR = 5000 ms, TE = 72 and 122 ms, bandwidth = 620 Hz/pixel, and 1.0 mm × 1.0 mm × 4.0 mm voxel resolution. Apparent diffusion coefficient (ADC) and trace image volumes are produced from 4 diffusion directions and 2 diffusion weightings at b-values of 0 and 1000 s/mm^2. ADC represents the mean diffusivity in mm^2/s and trace represents the sum of the diffusion-weighted images. RESOLVE ADC maps and and diffusion-weighted images are used to assess acute pathological changes [97] and it is acquired in approximately 3 minutes. In imaging stroke, diffusion-weighted imaging is important in identifying ischemic lesions, which show decreased ADC and elevated trace in acute ischemic tissue, and elevated ADC and decreased trace in chronic ischemic tissue [95]. Representative images for ADC and trace are depicted in Figure 2.4.

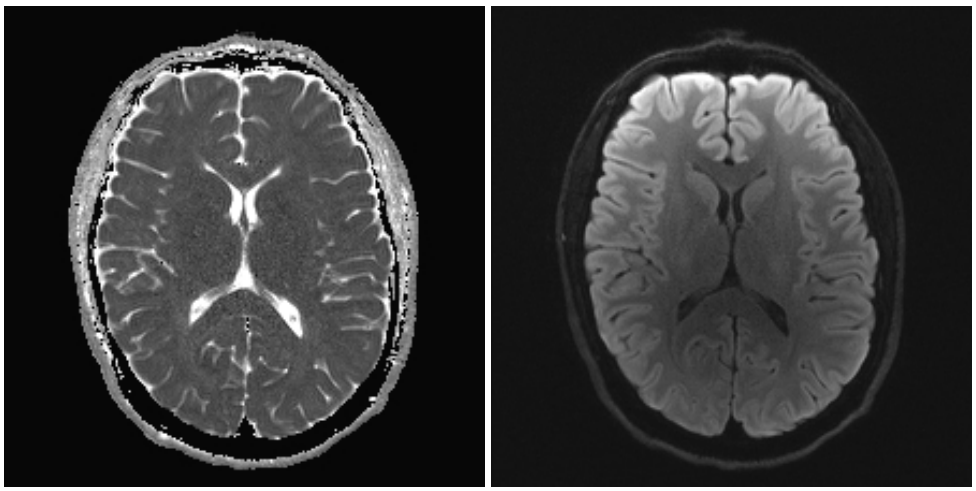

(a) Apparent Diffusion Coefficient (b) Trace

Figure 2.4: Representative ADC map (a) and trace-weighted image (b) in the axial plane of a healthy volunteer

2.5.3 Magnetic Resonance Angiography

Time-of-flight magnetic resonance angiography (TOF MRA) was acquired in the axial plane with TR = 22 ms, TE = 3.6 ms, FA = 18°, bandwidth = 186 Hz/pixel, an acceleration factor

of 2, and 0.4 mm × 0.4 mm × 0.8 mm voxel resolution. The FOV includes the mid-neck to the Sylvian fissures with 40 slices. The TOF MRA acquisition is used to assess vasculature without the use of a contrast agent [98] and it is acquired in approximately 5 minutes. Representative images by plane are depicted in Figure 2.5.

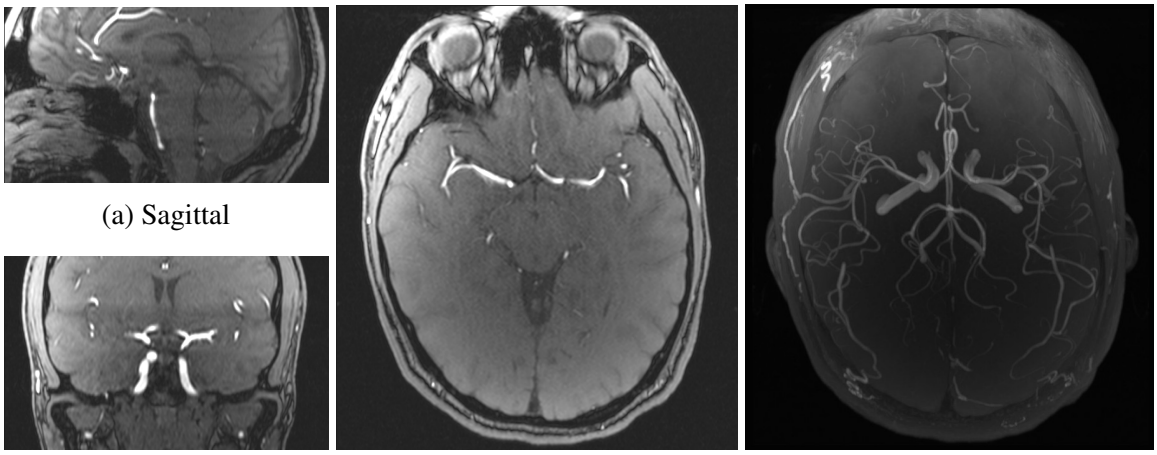

(a) Sagittal

(b) Coronal (c) Axial (d) MIP

Figure 2.5: Representative angiography images of a healthy volunteer. Blood accumulates phase as it flows perpendicular to the imaging plane into the brain, resulting in brightness in the vasculature. The maximum intensity projection (MIP) (d) illustrates the vasculature in 3D.

2.5.4 T_2-Weighted Imaging

A T_2-weighted fluid-attenuated inversion recovery (T2FLAIR) sequence was acquired in the sagittal plane with TR = 5000 ms, TE = 386 ms, FA = 120°, TI = 1800 ms, bandwidth = 751 Hz/pixel, an acceleration factor of 2, and 1 mm isotropic voxel resolution. The FOV includes the whole brain with 192 slices over 192 mm × 256 mm × 256 mm. The T2FLAIR acquisition reveals acute and chronic pathology such as in white matter hyperintensities [99], and it is acquired in approximately 3 minutes. The Fazekas system [100] was used for assessing periventricular hyperintensity and deep white matter hyperintensity. Representative images by plane are depicted in Figure 2.6.

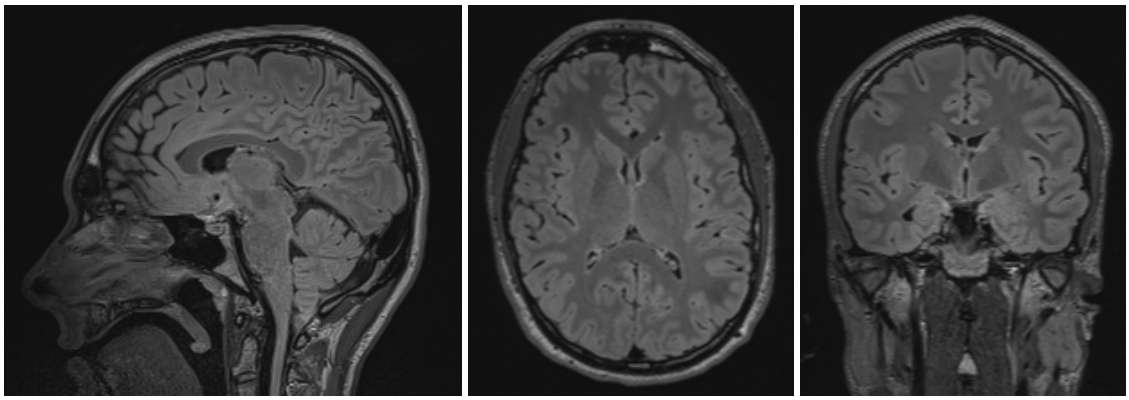

(a) Sagittal (b) Axial (c) Coronal

Figure 2.6: Representative T_2-weighted images of a healthy volunteer

2.5.5 Susceptibility-Weighted Imaging

Susceptibility-weighted images (SWI) were acquired in the axial plane with TR = 27 ms, TE = 20 ms, FA = 15°, bandwidth = 120 Hz/pixel, an acceleration factor of 2, and 0.9 mm × 0.9 mm × 2.8 mm voxel resolution. The FOV includes the whole brain with 56 slices over 230 mm × 173 mm × 173 mm. SWI is a T_2*-weighted acquisition used to visualize regions of abnormal susceptibility such as in microbleeds [101] and it is acquired in approximately 3 minutes. Representative images are depicted in Figure 2.7.

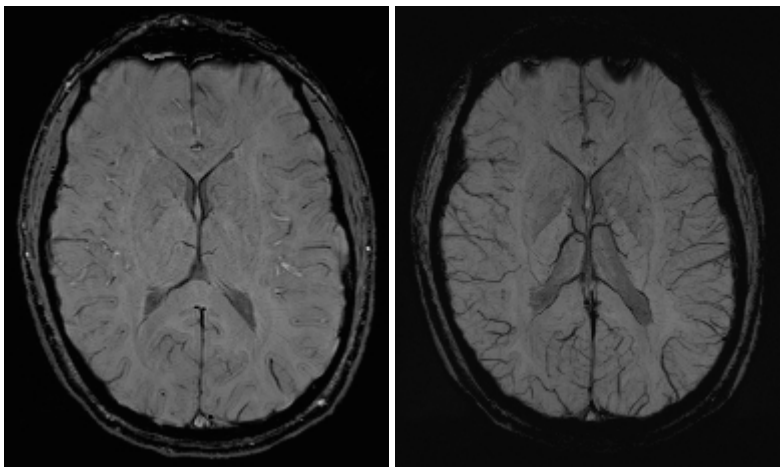

(a) Single Slice (b) mIP

Figure 2.7: Representative susceptibility-weighted images in the axial plane of a healthy volunteer. Minimum intensity projection (mIP) (b) is produced to visualize the trajectory of low intensities over several slices.

2.6 Quantitative MRI

Myelin water imaging was conducted using multi-component driven equilibrium single pulse observation of T_1 and T_2 (mcDESPOT) [88]. This involves driven equilibrium single pulse observation of T_1 (DESPOT1) and driven equilibrium single pulse observation of T_2 (DESPOT2). Voxels in DESPOT space are approximately 1.6 mm $\times$ 2.2 mm $\times$ 2.2 mm in a FOV of 190 mm $\times$ 190 mm $\times$ 215 mm over 80 slices. The sequences are used to generate quantitative maps for T_1, T_2, and MWF; which are all in DESPOT space. A flowchart summarizing how these quantitative maps are produced is depicted in Figure 2.8 and representative maps of T_1, T_2, and MWF are respectively shown in Figure 2.12, Figure 2.14, and Figure 2.15.

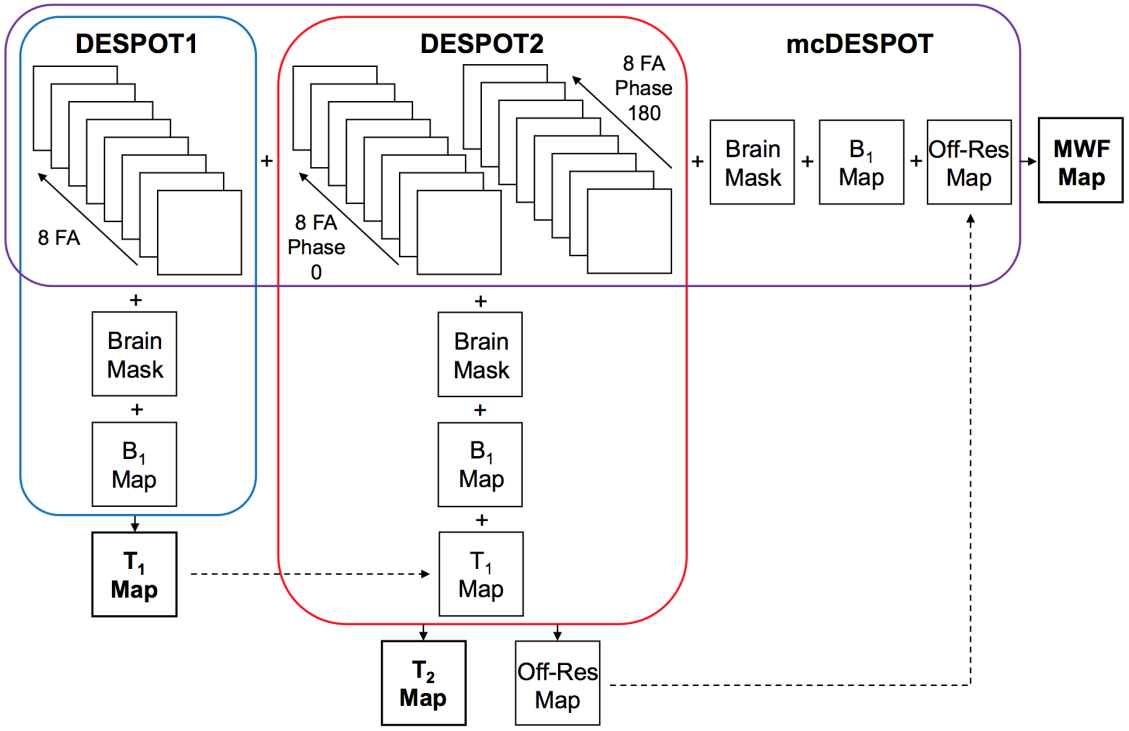

Figure 2.8: Quantitative image processing. Each square represents one volume in DESPOT space. DESPOT images are shown in Figure 2.11 and Figure 2.13. Brain mask, B_1 map, and off-resonance map are shown in Figure 2.9, Figure 2.10, and Figure 2.13. Outputs of T_1 map, T_2 map, and MWF map are shown in Figure 2.12, Figure 2.14, and Figure 2.15.

Preprocessing steps include: converting the images from DICOM to NIfTI format; extracting the brain from surrounding tissue; masking the brain to isolate brain-only voxels; convert-

ing the image volumes to the the same imaging space; and resampling the images to the same voxel resolution. DICOM volumes were converted to 4D NIfTI by dcm2nii on MRIcron [102] and volumes not in DESPOT space (such as the MPRAGE and B_1 map) were resampled using the BRAINS tool on 3D Slicer 4.10.2 [103]. Processing steps included the production of the three quantitative maps using Quantitative Imaging Tools (QUIT) [104] 2.0.1 for Linux. Post-processing steps focused on the statistics of the respective measurements by tissue and subregion. Masks of white matter, grey matter, and CSF were applied to the resulting quantitative maps to produce measurements by tissue. Regions of interest outlined by the neuroradiologist, from the qualitative MRI sequences, were identified within a predetermined list of subregions.

Brain Mask

Brain masks (Figure 2.9), to decrease image processing time, were obtained from the first volume of DESPOT1 (Figure 2.11) using the robust brain extraction tool (BET) [105] on FSL 5.0 [106]. The same brain mask was applied to each avenue of image processing. Additional masks for white matter, grey matter, and CSF were obtained from the T_1-weighted image (MPRAGE) using the FMRIB's automated segmentation tool (FAST) on FSL [107]. The tissue-specific masks were applied to the resulting quantitative maps.

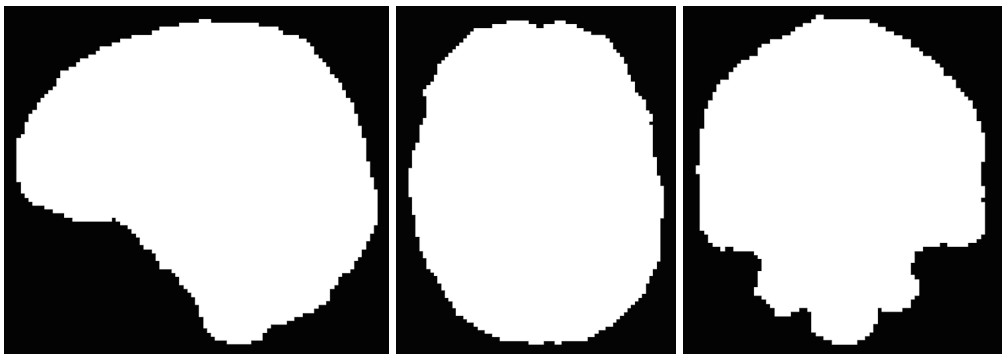

(a) Sagittal (b) Axial (c) Coronal

Figure 2.9: Brain mask of a healthy volunteer

B_1 Map

Although B_1^+ corresponds to the transmit field coil and B_1^- corresponds to the receive field coil; for simplicity in documentation, B_1 signifies the B_1^+ transmit field map throughout this thesis. Due to inhomogeneities in the magnetic field, the flip angles resulting from the transmit coil are not homogeneous throughout the brain and a B_1 map sequence is acquired to correct this inhomogeneity. Two volumes with different repetition times and a flip angle of 8 degrees are acquired in 30 seconds. The ratio of these two images indicates the fraction of one required to correct B_1 inhomogeneities in other acquisitions, notably DESPOT1 and DESPOT2 [104] . A value lower than one indicates that the voxel is receiving a lower flip angle than intended while a value higher than one indicates the voxel is receiving a higher flip angle than intended. A representative B_1 map is shown in Figure 2.10. The same B_1 map was applied to each avenue of image processing.

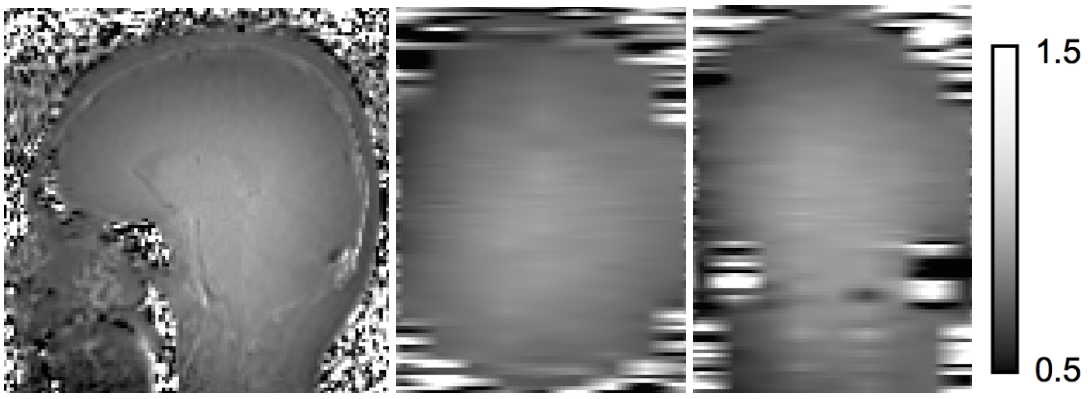

(a) Sagittal (b) Axial (c) Coronal

Figure 2.10: B_1 map of a healthy volunteer

2.6.1 T_1 Mapping

Image processing for T_1 mapping is outlined in blue in Figure 2.8. DESPOT1 uses a spoiled-gradient echo sequence (SPGR) acquired in the sagittal plane with TR = 6.9 ms, TE = 2.9 ms, and bandwidth = 350 Hz/pixel. Eight SPGR volumes (Figure 2.11) are acquired at varying flip angles: 2.67, 3.56, 4.44, 5.33, 6.22, 8, 11.55, and 16 degrees. The SPGR images acquired

for DESPOT1 are T_1-weighted and they are acquired in approximately 6 minutes. The eight SPGR volumes, brain mask, and B_1 produce a T_1 map (Figure 2.12) in under one minute using the non-linear least squares algorithm on QUIT [104]. T_1 is calculated for each voxel using the relative signal as a function of flip angle (α) over the eight volumes [108]. Equation 2.3 and Equation 2.4 display these signal equations to obtain the T_1 within each voxel.

$$S_{SPGR} = \frac{M_o(1 - E_1)\sin(\alpha)}{1 - E_1\cos(\alpha)} \tag{2.1}$$

$$E_1 = \exp(-TR/T_1) \tag{2.2}$$

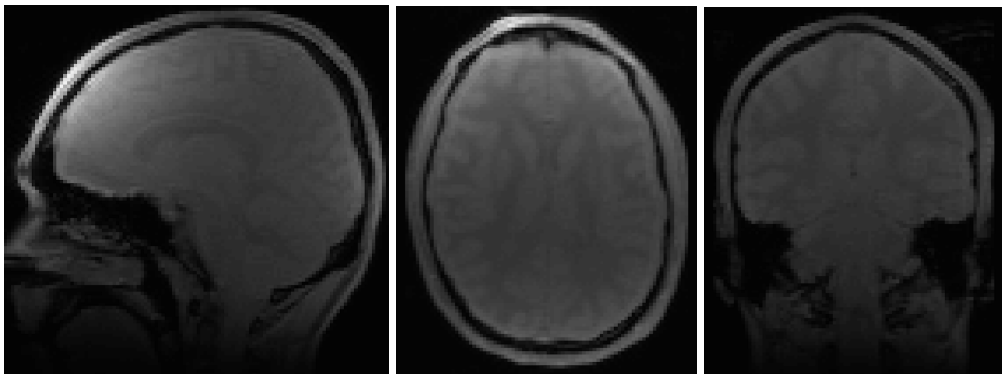

(a) Sagittal (b) Axial (c) Coronal

Figure 2.11: Slices from the first SPGR volume, for T_1 mapping, of a healthy volunteer

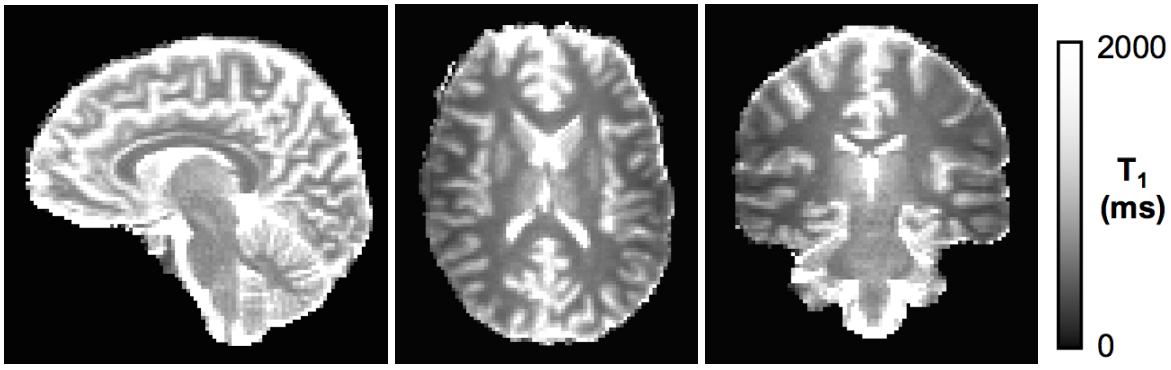

(a) Sagittal (b) Axial (c) Coronal

Figure 2.12: T_1 map of a healthy volunteer

2.6.2 T_2 Mapping

Image processing for T_2 mapping is outlined in red in Figure 2.8. DESPOT2 uses a balanced steady-state free precession (bSSFP) sequence acquired in the sagittal plane with TR = 6.0 ms and TE = 2.9 ms. Eight bSSFP volumes are acquired at varying flip angles: 10, 13.33, 16.67, 20, 23.33, 30, 40.33, and 60 degrees. However, unlike SPGR images, a banding artifact occurs in bSSFP images, as seen in the first two rows of Figure 2.13. This is resolved by acquiring two sets of bSSFP volumes; one at a phase increment of 180 degrees and the other at a phase increment of 0 degrees. This variation between the two bSSFP acquisitions produces banding artifacts that are spatially offset. It is corrected analytically with at least two flip angles and at least two phase offsets [109] as the difference between the two phase offsets amounts to an off-resonance map. The full model for DESPOT2 (DESPOT2-FM) corrects the banding artifact using the off-resonance map between imaging volumes at varying phase increments [110]. The bSSFP images acquired for DESPOT2 are T_1- and T_2-weighted. The two sets are acquired in approximately 12 minutes. The sixteen bSSFP volumes, brain mask, B_1 map, and T_1 map produce a T_2 map (Figure 2.14) and an off-resonance map (Figure 2.13) in one to two minutes using QUIT [104]. T_2 is calculated for each voxel using the relative signal as a function of flip angle (α) of the eight volumes [108] in the banding-corrected images. Equation 2.3 and Equation 2.4 display the signal equations to obtain the T_2 within each voxel.

$$S_{bSSFP} = \frac{M_o(1 - E_1)\sin(\alpha)}{1 - E_1E_2 - (E_1 - E_2)\cos(\alpha)} \tag{2.3}$$

$$E_2 = \exp(-TR/T_2) \tag{2.4}$$

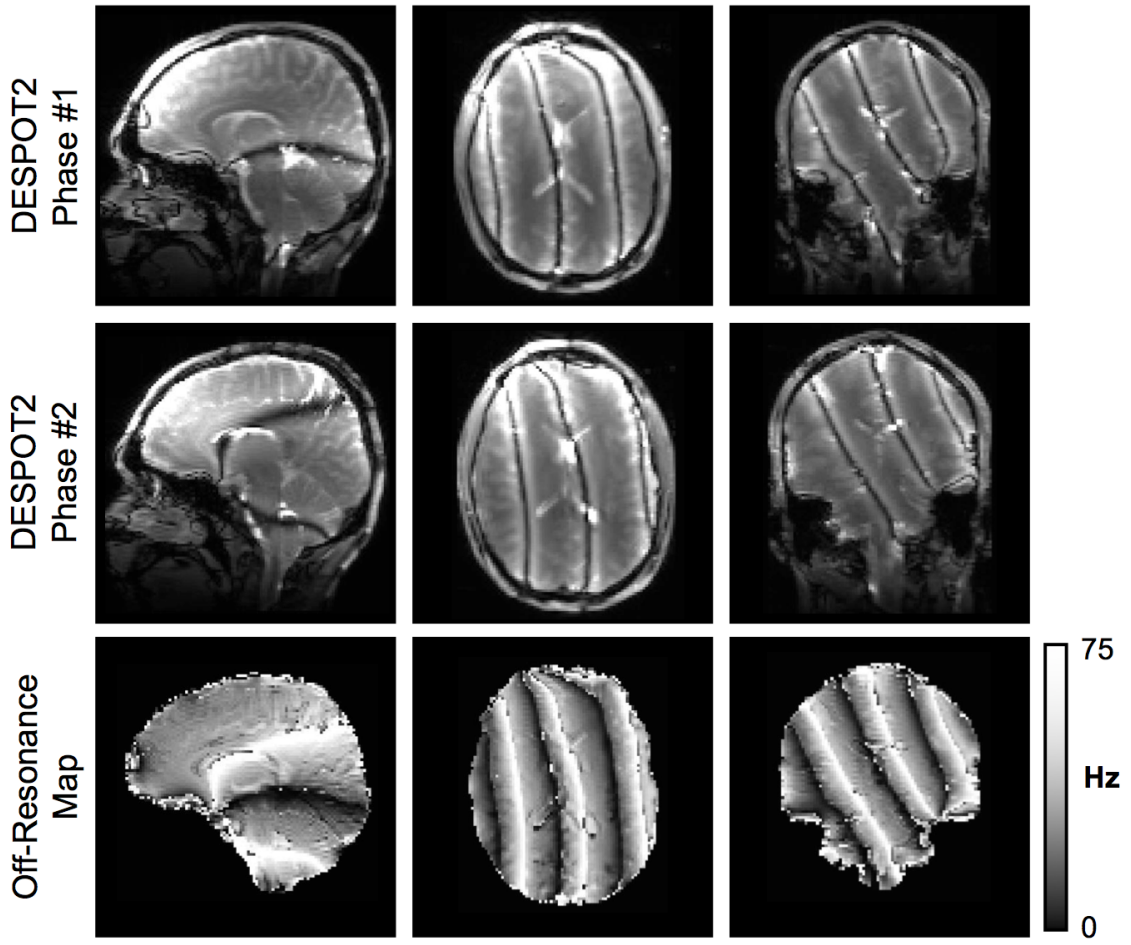

Figure 2.13: Slices from bSSFP acquisitions, at each phase increment and resulting off-resonance map, of a healthy volunteer

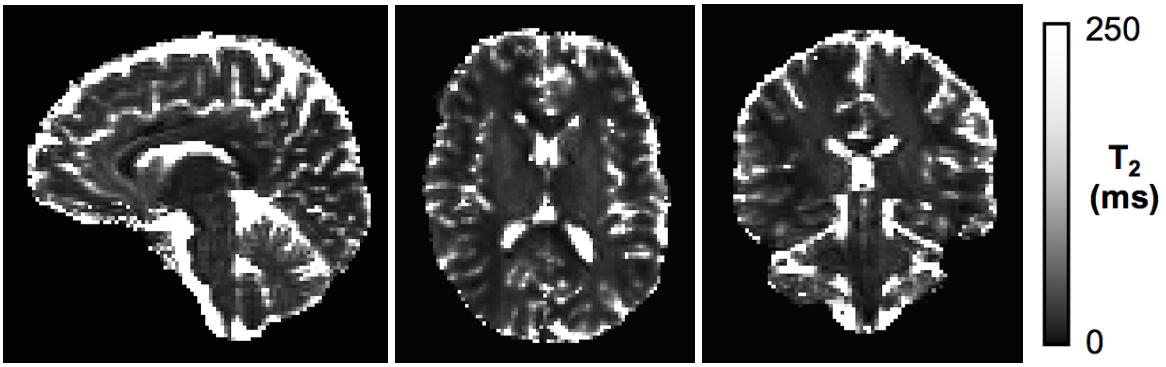

(a) Sagittal (b) Axial (c) Coronal

Figure 2.14: T_2 map of a healthy volunteer

2.6.3 Myelin Water Fraction Mapping

Image processing for MWF mapping is outlined in purple in Figure 2.8. The technique of mcDESPOT was chosen because it is widely used in human studies, artifact resistant, available on the Siemens scanner, and clinically feasible with a total acquisition of 18 minutes (Figure 2.2). Myelin water imaging by mcDESPOT provides a sensitive measure of white matter integrity through combining data from the T_1- and T_2-weighted volumes acquired for DESPOT1 and DESPOT2 [88].

The estimation of MWF involves a complicated model with assumptions which may bias the MWF measurement [111]. This motivates consistency in methodology when drawing comparisons between studies that use mcDESPOT. The three compartment model was used, which consists of myelin water, intracellular and extracellular water, and CSF [112]. Exchange between compartments was also included in the model. Parameter estimates in each voxel were obtained using a stochastic region contraction approach with four iterations [113]. These steps follow the recommended guidelines in the literature [111] and were used for the MWF fitting throughout the analysis, giving internally consistent datasets.

The signal equations for mcDESPOT assume fast and slow relaxing compartments representing myelin and intracellular/extracellular water compartments, respectively. Equation 2.5, Equation 2.6, and Equation 2.7 represent the multi-compartment signal equation for the SPGR sequence (DESPOT1). Parameters include a factor proportional to the longitudinal magnetization (ρ), volume fractions of fast and slow relaxing compartments (f_F and f_S), exchange rates between fast and slow relaxing compartments (k_{FS} and k_{SF}), and T_1 relaxation times of the fast and slow relaxing compartments ($T_{1,F}$ and $T_{1,S}$).

$$M^{SS}_{SPGR} = M_{SPGR}(I - e^{A_{SPGR}TR})\sin(\alpha) \times (1 - e^{A_{SPGR}TR}\cos(\alpha))^{-1} \tag{2.5}$$

$$M_{SPGR} = \rho \begin{bmatrix} f_F & f_S \end{bmatrix}^r \tag{2.6}$$

$$A_{SPGR} = \begin{bmatrix} -\frac{1}{T_{1,F}-k_{FS}} & k_{SF} \\ k_{FS} & -\frac{1}{T_{1,S}} - k_{SF} \end{bmatrix} \tag{2.7}$$

Equation 2.8, Equation 2.9, and Equation 2.10 represent the multi-compartment signal equation for the bSSFP sequence (DESPOT2). Additional parameters include a rotation matrix describing the RF pulse ($R(\alpha)$), a 6×6 identity matrix (I), off-resonance effects of the fast and slow relaxing compartments ($\Delta\omega_F$ and $\Delta\omega_S$), and T_2 for the fast and slow relaxing compartments ($T_{2,F}$ and $T_{2,S}$). In this formulation, the MWF is equivalent to the volume fraction of the fast relaxing compartment.

$$M^{SS}_{bSSFP} = (e^{A_{bSSFP}TR} - I)A^{-1}_{bSSFP}C \times [I - e^{A_{bSSFP}TR}R(\alpha)]^{-1} \tag{2.8}$$

$$A_{bSSFP} = \begin{bmatrix} -\frac{1}{T_{2,F}} - k_{FS} & k_{SF} & \Delta\omega_F & 0 & 0 & 0 \\ k_{FS} & -\frac{1}{T_{2,S}} - k_{SF} & 0 & \Delta\omega_S & 0 & 0 \\ -\Delta\omega_F & 0 & -\frac{1}{T_{2,F}} - k_{FS} & k_{SF} & 0 & 0 \\ 0 & -\Delta\omega_S & k_{FS} & -\frac{1}{T_{2,S}} - k_{SF} & 0 & 0 \\ 0 & 0 & 0 & 0 & -\frac{1}{T_{1,F}} - k_{FS} & k_{SF} \\ 0 & 0 & 0 & 0 & k_{FS} & -\frac{1}{T_{1,S}} - k_{SF} \end{bmatrix} \tag{2.9}$$

$$C = \rho \begin{bmatrix} 0 & 0 & 0 & 0 & \frac{f_F}{T_{1,F}} & \frac{f_S}{T_{1,S}} \end{bmatrix} \tag{2.10}$$

The eight volumes of DESPOT1, sixteen volumes of DESPOT2, brain mask, B_1 map, and off-resonance map produce the MWF map (Figure 2.15) using QUIT [104]. However, unlike the fast image processing for quantitative maps of T_1 and T_2, the MWF map is produced in four to five hours. Pipeline development was evaluated using a single slice of the brain in approximately ten minutes.

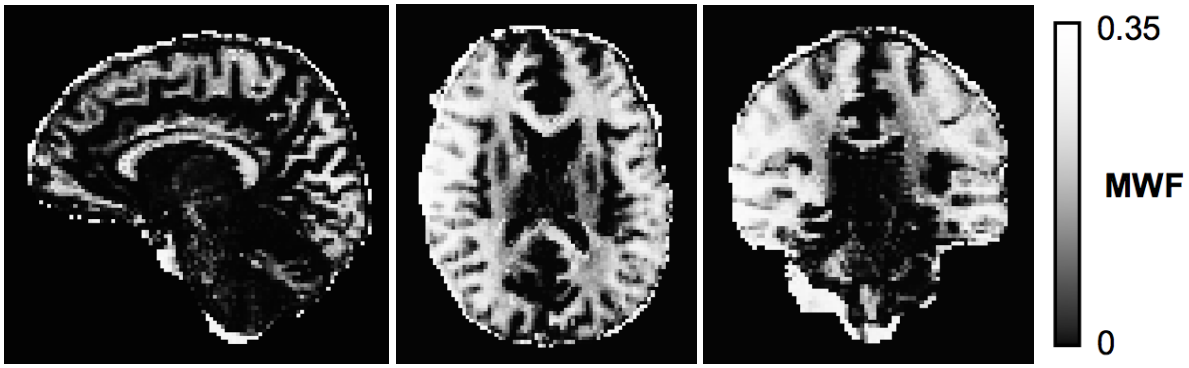

(a) Sagittal (b) Axial (c) Coronal

Figure 2.15: Myelin water fraction map of a healthy volunteer

2.7 Qualitative MRI Analysis

No abnormalities were detected in the volunteer brain presented throughout this chapter. Abnormalities in the brains of the 13 patients were documented during the neuroradiologist viewing with a focus on documenting atrophy, infarcts, points of abnormal susceptibility, and white matter hyperintensities; as guided by the limited literature on brain imaging in TMA, described in subsection 1.1.7. Findings in T2FLAIR were used to select the regions of interest for subregion analysis with quantitative MRI measurements. Regions of white matter hyperintensity were labeled as ipsilateral, contralateral, or bilateral. Otherwise, regions remained as left or right for control comparisons. There is no objective way to rank the severity of brain health based on the neuroradiologist reads for comparison to quantitative rankings. To mitigate bias in comparing qualitative findings with quantitative measurements, a binary classification for neuroradiologist findings was considered: few to no findings, or many findings.

Statistics

Chi-square tests were conducted to compare the number of white matter hyperintensities in regions of interest; left versus right side, and unilateral versus bilateral. Two-tailed t-tests were evaluated between quantitative measurements; depression score, cognitive score, and quantitative white matter measurements; based on the binary classification of the neurologist findings.

2.8 Quantitative MRI Analysis

FSL was used to upper threshold quantitative maps: T_1 to 15,000 ms, T_2 to 10,000 ms, and MWF to 1. These T_1 and T_2 thresholds were beyond three standard deviations of the mean T_1 and T_2 in their respective quantitative maps. Additionally, a MWF >1 is meaningless and voxels with values >1 were eliminated. Thresholding removed only 10–100 voxels out of more than 100,000 in the brain. Values above the respective thresholds were zeroed. Statistics of mean, standard deviation, and volume by tissue in T_1, T_2, and MWF were obtained in non-zero voxels using FSL.

Regions of Interest

The qualitative findings in T2FLAIR guided the subregion quantitative analysis. Regions of interest, the lesions outlined by the neuroradiologist in T2FLAIR sequences, were identified by overlaying the T2FLAIR on white matter parcellation from FreeSurfer [114]. The registration to the FreeSurfer brain space was done using the MPRAGE dataset because it is higher spatial resolution than the DESPOT1 dataset. Subsequently, the registered MPRAGE volume was brought into DESPOT space.

A total of 28 subregions, 13 left-right and 2 non left-right, were chosen based on a literature search for where brain white matter hyperintensities most often occur in vascular-related diseases due to a gap in brain imaging literature specific to TMA. These white matter subregions (column 1 of Table 2.2) were in the cerebellum [115], thalamus [115, 116], caudate [115, 116], pallidum [115], hippocampus [117], centrum semiovale [116], frontal lobe [115, 118, 116], and brain stem [115]. Additional subregions in the other three lobes and corpus callosum were added for completeness of white matter regions throughout the brain. Segmentation of subregions was completed in 3D Slicer using thresholds for the values specified by the FreeSurfer parcellation lookup table (column 2 of Table 2.2). Small island voxels fewer than five were removed. Using the resulting segmentation file, segment statistics on 3D Slicer were applied

to each quantitative map for mean, standard deviation, and volume within subreregion. Measurements of T_1, T_2, and MWF in ipsilateral and contralateral subregions for regions of interest outlined by the neuroradiologist were normalized to the respective subregion mean across all 13 patients to account for variability between subregions.

Subregion	Label
Cerebellum WM	6, 49
Thalamus	10, 49
Caudate	11, 50
Pallidum	13, 52
Hippocampus	17, 53
Centrum semiovale	5001, 5002
Caudal middle frontal WM	3003, 4003
Lateral orbitofrontal WM	3012, 4012
Precentral frontal WM	3024, 4024
Rostral middle frontal WM	3027, 4027
Lateral occipital WM	3011, 4011
Superior temporal WM	3030, 4030
Supramarginal parietal WM	3031, 4031
Corpus callosum	251–255
Brain stem	16

Table 2.2: Subregions from FreeSurfer parcellation with label by lookup table (left, right)

Statistics

Welch's two-tailed t-test was conducted on MRI measurements of T_1, T_2, and MWF between male and female, and between patients with TTP and aHUS. A one-way ANOVA test was conducted for left-right comparisons within the 13 left-right subregions in T_1, T_2, and MWF. Tukey's multiple comparison test was conducted for subregions $P < 0.05$. Welch's two-tailed t-test was conducted for ipsilateral-contralateral comparisons of MRI measurements. Welch's one-tailed t-tests were conducted for ipsilateral-contralateral comparisons within increases and decreases of MRI measurements in regions of interest. The chi-square test was conducted for ipsilateral versus contralateral counts in increases and decreases for each of T_1, T_2, and MWF. All unilateral subregions were applied to T_1 and T_2 comparisons, while unilateral subregions

omitting mostly grey matter regions were applied to MWF comparisons. Pearson correlations were evaluated for T_1, T_2, and MWF within grey matter and white matter while Spearman correlations were evaluated for all ten measurements: T_1, T_2, and MWF in white matter and grey matter; depression score; cognitive percentile; age; and time with diagnosis. Lastly, a Friedman test for mean ranking across each of the ten measurements by patient was evaluated to investigate agreement between the quantitative measurements. Table 2.3 demonstrates the directionality for the ranks of each measurement.

Measurement	Value	Ranking
MADRS	Depression score	High → low
CBS	Cognitive percentile	Low → high
T_1 WM	T_1 white matter (ms)	High → low
T_2 WM	T_2 white matter (ms)	High → low
MWF WM	MWF white matter	Low → high
T_1 GM	T_1 grey matter (ms)	High → low
T_2 GM	T_2 grey matter (ms)	High → low
MWF GM	MWF grey matter	Low → high
Time	Diagnosis date to scan	High → low
Age	Age at scan	High → low

Table 2.3: Ten measurements with corresponding directionality of rank

Chapter 3

Results

3.1 Depression Scores

All 13 patients completed the Montgomery-Åsberg Depression Rating Scale (MADRS), which was administered in a clinical interview by a nurse.

Scores by Patient

Figure 3.1 shows the total depression score for each patient by MADRS. Considering the mean and standard deviation of scores over the 10 assessments, a one-way ANOVA using the Brown-Forsythe test shows a significant difference between scores of the patients ($P < 0.0001$). The Brown-Forsythe test was used because the data is not Gaussian and skewed to the left. Dunnett's T3 multiple comparisons test indicates 5 significant pairwise differences. These are between the scores of patients of the two highest scores (patients 2 and 10) with 5 patients of the seven lowest scores (patients 1, 4, 5, 6, and 12). Figure 3.2 shows depression scores by sex and diagnosis. There are no significant differences between the scores of male and female patients ($P = 0.0784$) or between patients with TTP and patients with aHUS ($P = 0.4602$). Following the thresholds by scores [91] for normal, mild depression, moderate depression, and severe depression, Table 3.1 shows the number of patients that fall under each category.

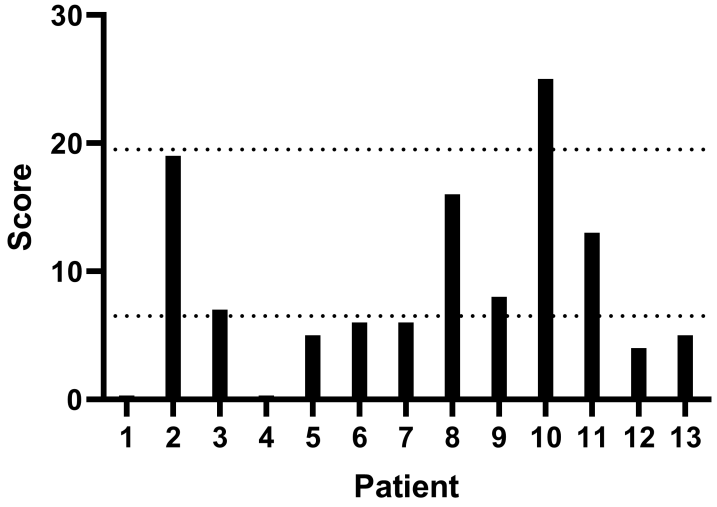

Figure 3.1: Depression scores by patient on the Montgomery-Åsberg Depression Rating Scale. Dashed lines represent thresholds for mild and moderate depression. The range of possible scores is 0–60.

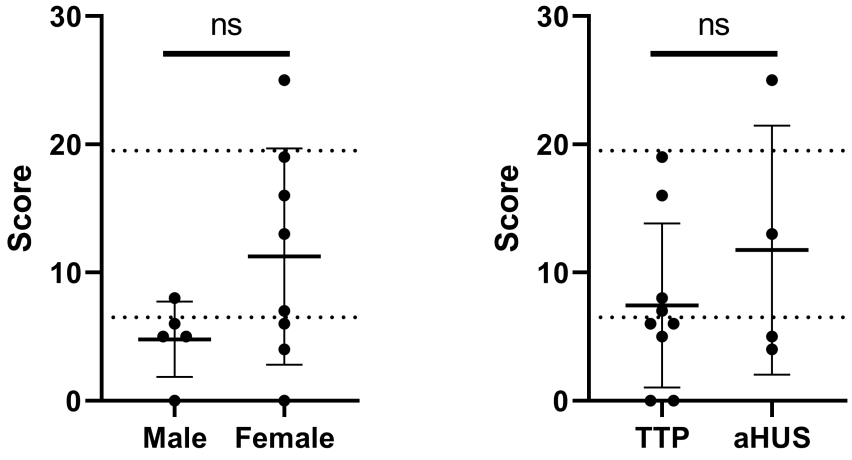

(a) Sex

(b) Diagnosis

Figure 3.2: Depression scores ± standard deviation by sex and diagnosis. Dashed lines represent thresholds for mild and moderate depression. The range of possible scores is 0–60

Score	Classification	Count
0–6	Normal	7
7–19	Mild depression	5
20–34	Moderate depression	1
>34	Severe depression	0

Table 3.1: Patients by type of depression. Count represents number of patients within corresponding range of scores. Normal indicates symptoms of depression are absent.

Scores by Assessment

Table 3.2 shows the average score by assessment ranked from highest to lowest; from highest indication of depression to lowest indication of depression. There is a significant difference in response by assessment through one-way ANOVA using the Brown-Forsythe test ($P < 0.0001$). Dunnett's T3 multiple comparisons test indicates significant differences in concentration difficulties and: reduced appetite ($P = 0.0088$), inability to feel ($P = 0.0088$), pessimistic thoughts ($P = 0.0049$), and suicidal thoughts ($P = 0.0029$). Furthermore, a chi-square test for the number of non-zero scores per assessment shows significance ($P = 0.0059$). However, multiple comparisons by Fisher's exact test using a Bonferroni correction does not indicate any significant pairwise differences.

Rank	Assessment	Score	Count
1	Concentration Difficulties	2.3 ± 1.3	11
2	Inner Tension	1.3 ± 1.3	8
3	Lassitude	1.2 ± 1.1	9
4	Reduced Sleep	1.0 ± 1.4	6
5	Apparent Sadness	0.8 ± 1.3	5
5	Reported Sadness	0.8 ± 1.1	6
7	Reduced Appetite	0.4 ± 0.8	3
7	Inability to Feel	0.4 ± 0.8	3
9	Pessimistic Thoughts	0.3 ± 0.6	3
10	Suicidal Thoughts	0.2 ± 0.4	3

Table 3.2: Mean depression score ± standard deviation by assessment, ranked highest to lowest. Count represents the number of participants with a score greater than zero. The range of possible scores for each assessment is 0–6.

3.2 Cognitive Scores

All 13 patients completed the cognitive assessment through the online platform, Cambridge Brain Sciences (CBS). The average number of valid scores over the 12-test battery was 11 out of 12, with three patients with 7–10 valid scores and ten patients with 11 or 12 valid scores. The online platform indicates whether a score is valid or invalid based on the user's interaction with the test. Invalid scores are considered meaningless as the patient may have misunderstood the task and these scores are omitted from the analysis. Cognitive scores are represented by percentiles which have been age- and sex-matched to a healthy control population of >10,000 participants.

Scores by Patient

Cognitive scores by patient are shown in Figure 3.3. The average score was 50.2 ± 19.8% across the 13 patients. There is no significant difference from the age- and sex-matched control population in the CBS database ($P = 0.9301$). The mean score of each patient is within one standard deviation of the age- and sex-matched population mean. A one-way ANOVA between the mean scores of each patient indicates significance ($P < 0.0001$). Tukey's multiple comparisons test indicates 19 significant pairwise differences between the scores of patients of the six highest scores and patients of the four lowest scores. Figure 3.4 shows cognitive percentiles by sex and diagnosis. There is a significant difference between the cognitive scores of male and female patients ($P = 0.0207$), but not between patients with TTP and patients with aHUS ($P = 0.7683$).

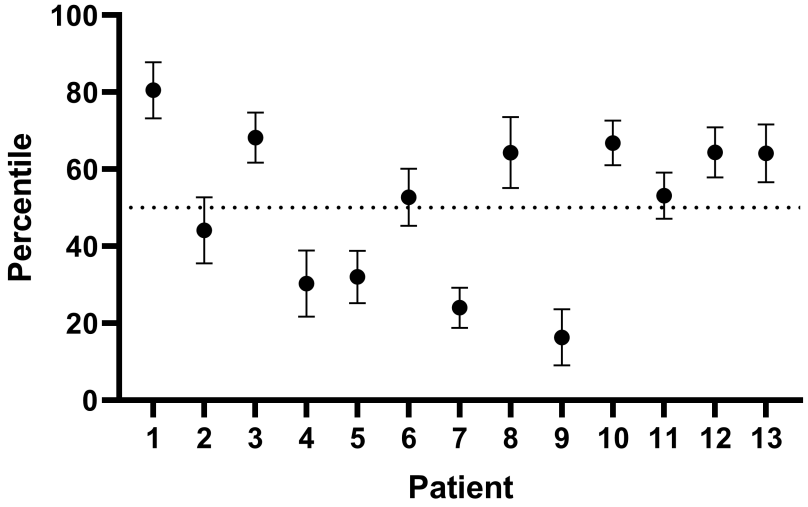

Figure 3.3: Cognitive percentiles ± standard error. Dashed line represents the 50th percentile.

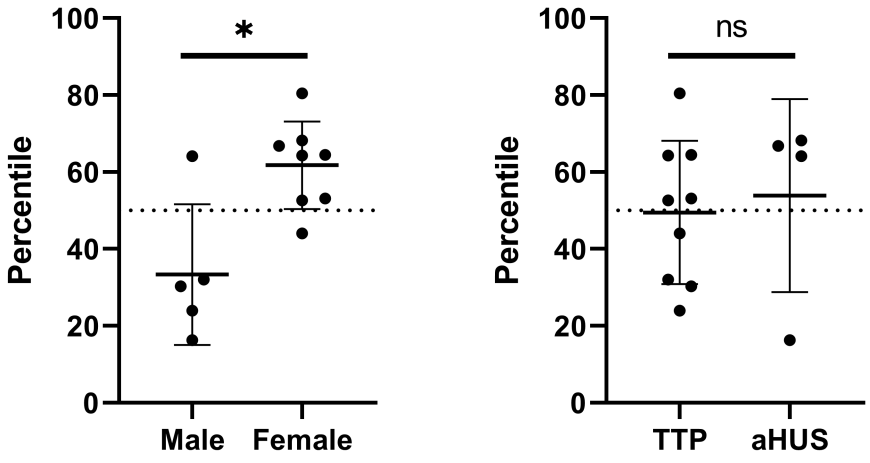

(a) Sex

(b) Diagnosis

Figure 3.4: Mean cognitive percentiles ± standard deviation by sex and diagnosis. Dashed line represents the 50th percentile.

Scores by Test and Category

Each of the 12 tests in the cognitive assessment falls into one of three categories: verbal, reasoning, and memory. Table 3.3 shows the mean score by test across all patients and the scores are ranked from lowest to highest; from highest level of cognitive impairment to lowest level of cognitive impairment. A one-way ANOVA indicates no significant differences between mean scores by test (P = 0.9796). A one-way ANOVA between the three categories indicates no significant differences (P = 0.8958). The same conclusion is drawn regardless of which category polygons is placed into.

Rank	Test	Percentile	Category
1	Double Trouble	45.2 ± 28.0	Verbal
2	Odd One Out	47.3 ± 27.7	Reasoning
3	Polygons	49.1 ± 24.8	Reasoning/Memory
4	Rotations	49.1 ± 29.3	Memory
5	Digit Span	50.5 ± 32.4	Verbal
6	Spatial Span	51.2 ± 35.6	Memory
7	Paired Associates	53.8 ± 28.5	Memory
8	Feature Match	54.0 ± 32.5	Reasoning
9	Grammatical Reasoning	54.2 ± 38.0	Reasoning
10	Token Search	57.0 ± 27.3	Verbal
11	Monkey Ladder	60.0 ± 26.0	Reasoning
12	Spatial Planning	61.7 ± 28.1	Memory

Table 3.3: Mean cognitive percentiles ± standard deviation by test and corresponding category. Percentiles ranked from highest to lowest level of cognitive impairment.

3.3 Qualitative MRI

3.3.1 Representative Findings

MPRAGE (T_1-weighted), RESOLVE (diffusion-weighted), TOF MRA (angiography), SWI (susceptibility-weighted), and T2FLAIR (T_2-weighted) were assessed in each patient by a blinded neuroradiologist. Although no control data is presented in this thesis, there were datasets from three healthy volunteers mixed in with the patient datasets which blinded the

neuroradiologist to patient versus control. They only knew the age of the subject they were viewing. Table 3.4 highlights the findings by qualitative sequence. Figure 3.5 depicts representative findings by sequence in axial slices throughout patients with detected abnormalities. Negative findings for each acquisition are comparable to the representative images presented of the healthy volunteer throughout section 2.5.

Patient	MPRAGE	RESOLVE	TOF MRA	SWI	T2FLAIR
1	-	-	-	-	Spots (3)
2	-	-	-	-	-
3	-	-	-	-	Spots (5)
4	-	-	Thrombus	-	Spot
5	Plaques (2), infarct	Chronic blood products	Poor PICA and AICA	-	Spots (10–15)
6	Spots (5)	-	-	Point	Infarct, spots (15–20)
7	Atrophy	-	-	-	Infarcts (3)
8	-	-	-	-	-
9	Atrophy	-	-	Points (10+)	Spots (25–30)
10	Infarcts (2)	-	-	-	Spots (5)
11	-	-	1 mm carotid cave, tight stenosis	Point	Infarcts (2), spots (5)
12	-	-	-	-	-
13	Atrophy	-	1 mm aneurysm	-	Spots (30–40)

Table 3.4: Summary of findings in qualitative MRI. MPRAGE: infarcts are chronic lacunar. TOF MRA: anterior inferior cerebellar artery (AICA) and posterior inferior cerebellar artery (PICA). SWI: points are punctate foci of abnormal susceptibility. T2FLAIR: spots are small non-specific regions of white matter hyperintensity while infarcts (chronic lacunar) are larger regions of white matter hyperintensity. Dash indicates no evidence of a finding. Patients with aHUS are patients 3, 9, 10, and 13.

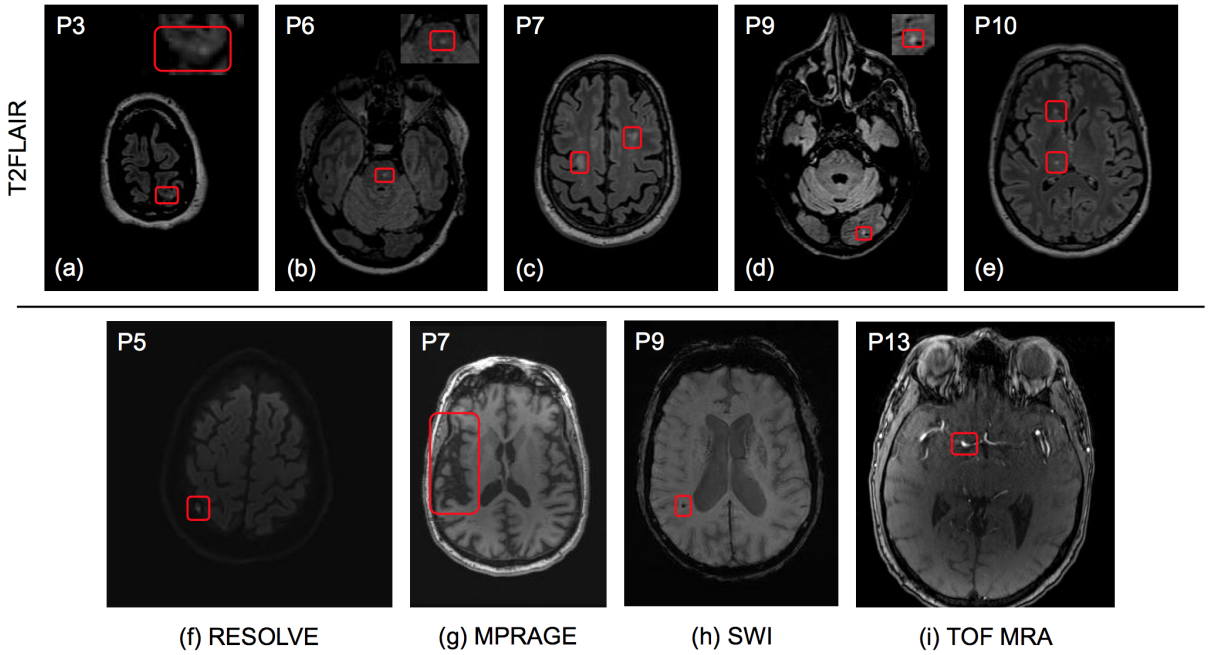

Figure 3.5: Axial images of representative findings in qualitative MRI, with regions of interest outlined in red boxes. (a)–(e) T2FLAIR: white matter hyperintensities were found throughout the brain; both unilaterally and bilaterally. (f) RESOLVE Trace: chronic blood products. (g) MPRAGE: atrophy in white matter. (h) SWI: point of abnormal susceptibility. (i) TOF MRA: 1 mm aneurysm.

3.3.2 Regions of Interest

Regions of interest were selected based only on findings in T2FLAIR. This was due to the nature of white matter hyperintensities directly relating to the central hypotheses of white matter damage in TTP and aHUS. Cumulatively, over the 10 patients with at least one abnormality in T2FLAIR, there were 32 ROIs in white matter. A total of 28 subregions (Table 2.2) with 13 left-right subregions and 2 non left-right subregions (corpus callosum and brain stem) were previously selected for subregion analysis. Using these 28 subregions, 87.5% (28/32) of ROIs outlined by the neuroradiologist were included. Of these included 28 ROIs in subsequent analysis, 23 were unilateral (5 were bilateral) and 10 were on the left side (13 were on the right side). Chi-square tests for differences in counts between unilateral versus bilateral and left versus right were significant (P = 0.0007) and non-significant (P = 0.5316), respectively.

3.4 Quantitative MRI

Quantitative MRI measurements of T_1, T_2, and MWF were obtained after fitting to DESPOT1 and DESPOT2 datasets. Whole brain volumes were measured to be 1489 ± 170 cm^3 after brain extraction and automated segmentation with FSL. The T_1, T_2, and MWF in CSF was obtained but not included in further analysis. Table 3.5 describes the volumes and quantitative measurements by tissue; white matter, grey matter, and CSF.

	White Matter	Grey Matter	CSF
Volume	674 ± 96	455 ± 56	360 ± 102
T_1	1057 ± 63	1504 ± 80	2174 ± 295
T_2	69 ± 17	179 ± 59	699 ± 192
MWF	0.211 ± 0.021	0.085 ± 0.018	0.091 ± 0.016

Table 3.5: Mean quantitative MRI measurements ± standard deviation by tissue. Volume is in cm^3, T_1 and T_2 are in ms, and myelin water fraction is unitless.

3.4.1 T_1 Maps

Figure 3.6 shows the mean T_1 in white matter and grey matter by sex and by diagnosis. There were no significant differences in mean T_1 of white matter by sex (P = 0.9325) or diagnosis (P = 0.3665), nor in mean T_1 of grey matter by sex (P = 0.9067) or diagnosis (P = 0.2835). Figure 3.7 shows the mean T_1 in the 13 left-right subregions. T_1 values for the non left-right subregions, brain stem and corpus callosum, are respectively 1261 ± 41 ms and 1249 ± 224 ms. Of the 23 unilateral regions of interest outlined by the neuroradiologist, 11 regions had increased T_1 and 12 had decreased T_1. By chi-square test, increased T_1 versus decreased T_1, this is not significant (P = 0.8348). Figure 3.8 shows the ipsilateral-contralateral comparison in these 11 regions of interest of increased T_1. T_1 values are normalized to the mean T_1 in the respective subregion across all 13 patients. The ipsilateral side is the unilateral region for which a lesion was observed. Under the demyelination hypothesis, increased ipsilateral T_1 is expected. There is no significant difference between the normalized T_1 in ipsilateral to contralateral.

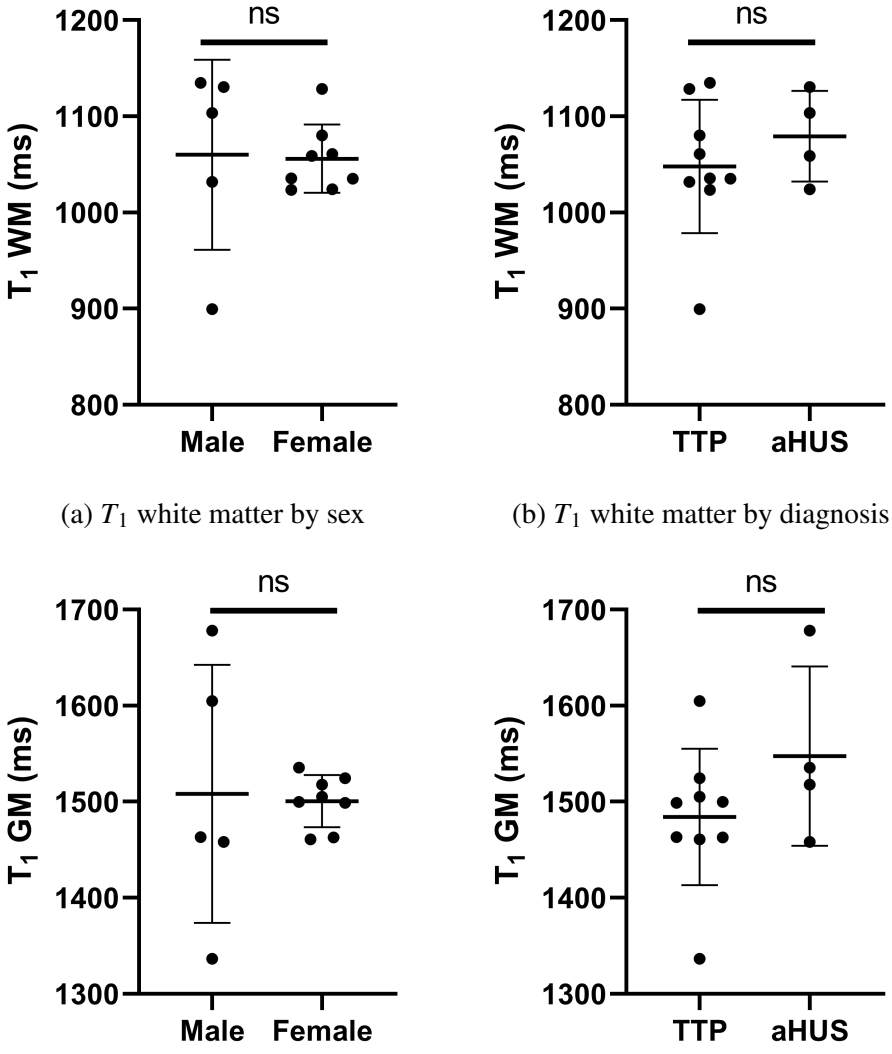

(a) T_1 white matter by sex

(b) T_1 white matter by diagnosis

(c) T_1 grey matter by sex

(d) T_1 grey matter by diagnosis

Figure 3.6: Mean T_1 ± standard deviation in white matter and grey matter by sex and diagnosis

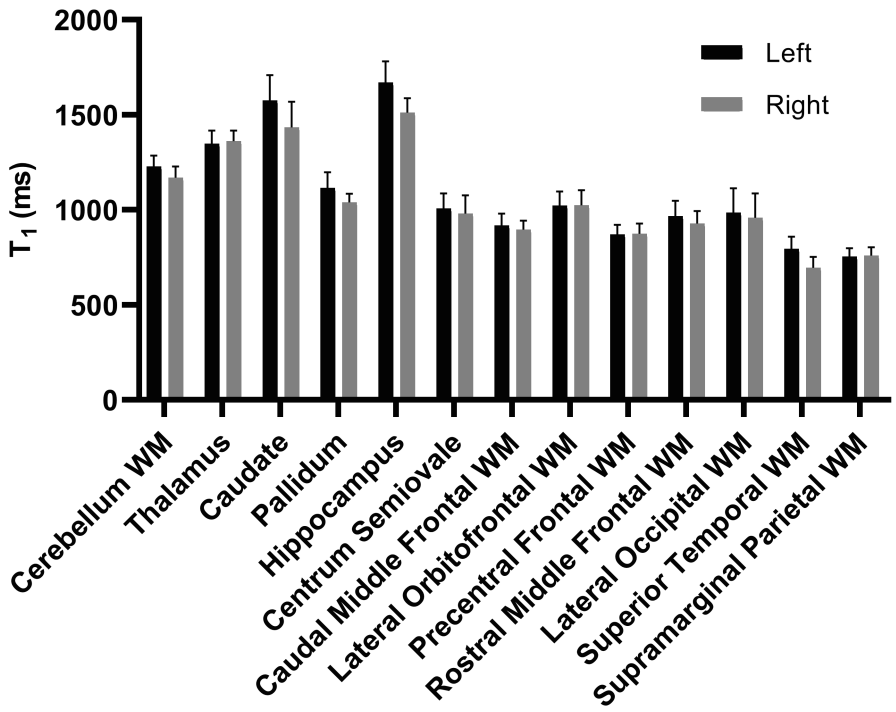

Figure 3.7: Mean T_1 ± standard deviation by subregion: left and right. Two left-right subregion comparisons were significantly different: hippocampus and superior temporal white matter.

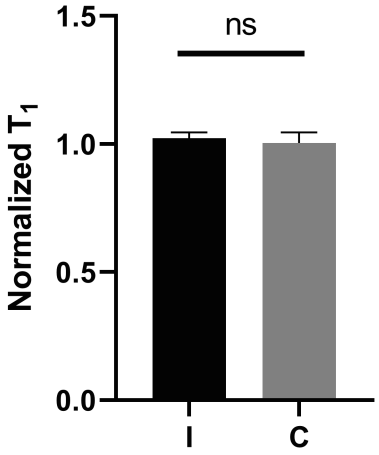

Figure 3.8: Mean T_1 ± standard deviation in lesions with increased ipsilateral T_1

3.4.2 T_2 Maps

Figure 3.9 shows the mean T_2 in white matter and grey matter by sex and by diagnosis. There were no significant differences in mean T_2 of white matter by sex (P = 0.1744) or diagnosis

(P = 0.1909), nor in mean T_2 of grey matter by sex (P = 0.1155) or diagnosis (P = 0.2502). Figure 3.10 shows the mean T_2 in the 13 left-right subregions. T_2 values for the non left-right subregions, brain stem and corpus callosum, are respectively 92 ± 14 ms and 139 ± 104 ms. Of the 23 unilateral regions of interest, 12 regions had increased T_2 and 11 had decreased T_2. By chi-square test, increased T_2 versus decreased T_2, this is not significant (P = 0.8348). T_2 values are normalized to the mean T_2 in the respective subregion across all 13 patients. Under the demyelination hypothesis, increased ipsilateral T_2 is expected. When considering the 12 regions of interest with increased T_2, there is a significant increase (Figure 3.11).

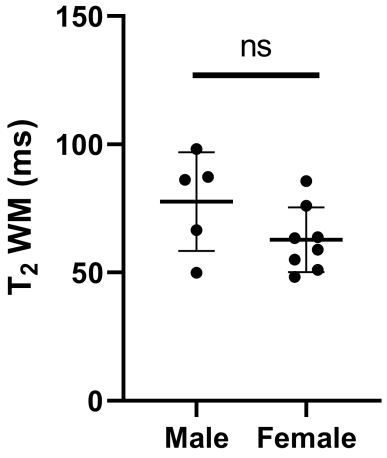

(a) T_2 white matter by sex

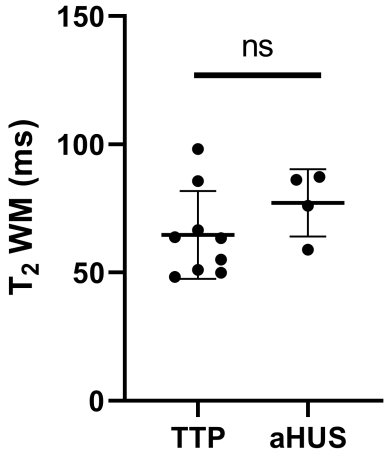

(b) T_2 white matter by diagnosis

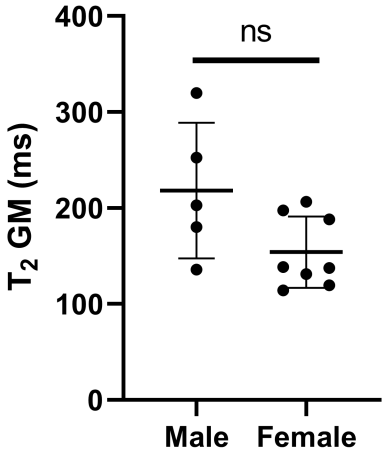

(c) T_2 grey matter by sex

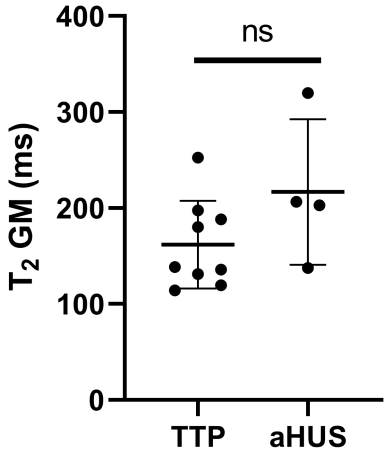

(d) T_2 grey matter by diagnosis

Figure 3.9: Mean T_2 ± standard deviation in white matter and grey matter by sex and diagnosis

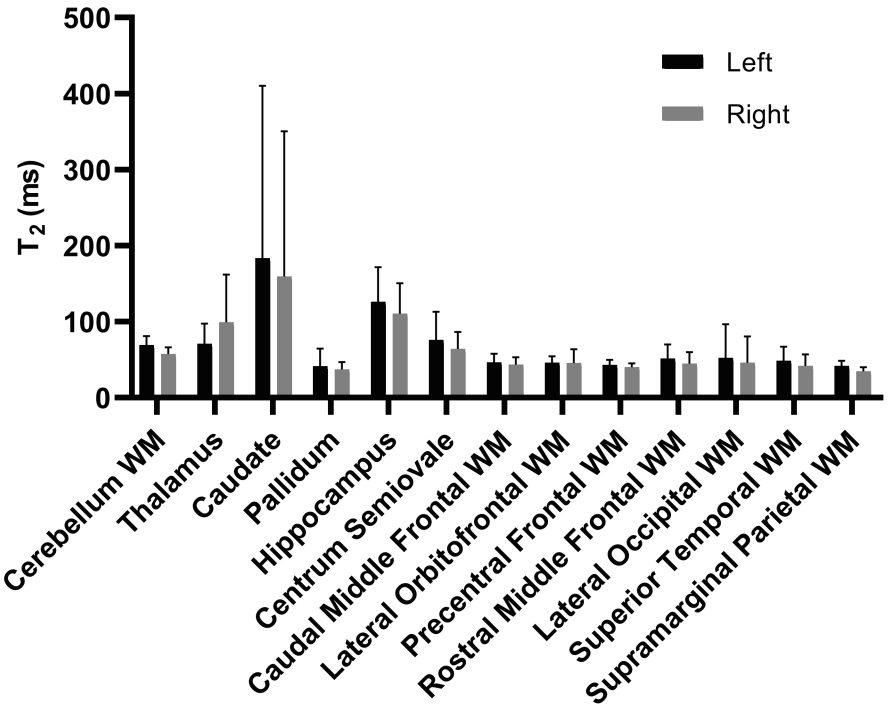

Figure 3.10: Mean T_2 ± standard deviation by subregion: left and right. No subregions were significantly different between left and right T_2.

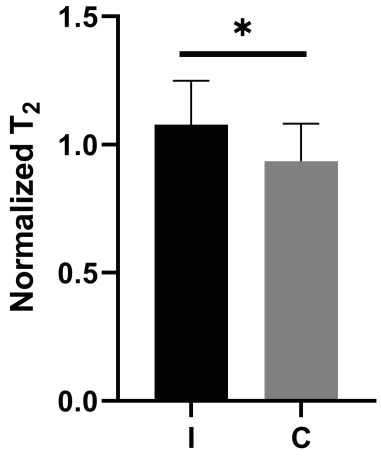

Figure 3.11: Mean T_2 ± standard deviation in lesions with increased ipsilateral T_2

3.4.3 Myelin Water Fraction Maps

Figure 3.12 shows the mean MWF in white matter and grey matter by sex and by diagnosis. There were no significant differences within white matter by sex (P = 0.9603) or diagnosis (P =

0.3877), nor within of grey matter by sex (P = 0.3578) or diagnosis (P = 0.7737). Figure 3.14 shows the mean MWF in the 13 left-right subregions. MWF values for the non left-right subregions, brain stem and corpus callosum, are respectively 0.158 ± 0.022 and 0.205 ± 0.041. Of the 20 unilateral regions of interest, omitting 3 regions of mostly grey matter, 14 regions had decreased MWF and 6 had increased MWF. By chi-square test, increase versus decrease in regions of interest is not significant (P = 0.073). Figure 3.14 shows the significant difference in the ipsilateral-contralateral comparison in the unilateral lesions which had decreased MWF.

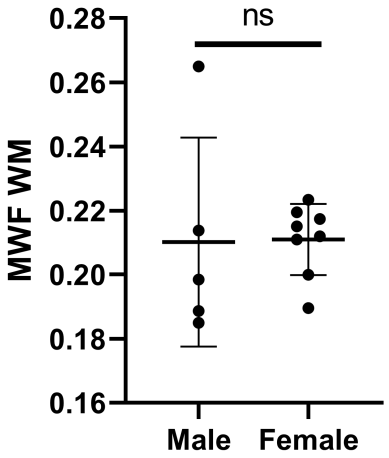

(a) MWF white matter by sex

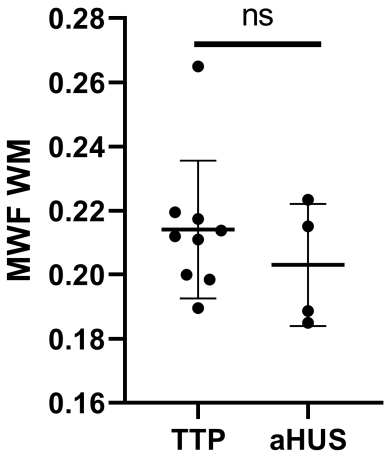

(b) MWF white matter by diagnosis

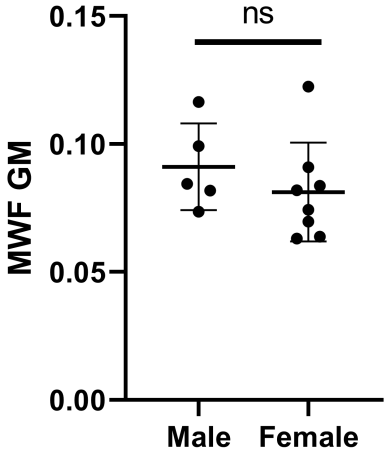

(c) MWF grey matter by sex

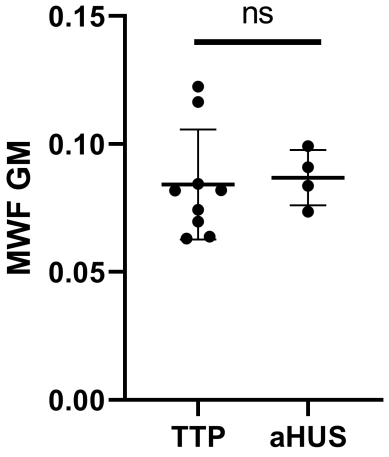

(d) MWF grey matter by diagnosis

Figure 3.12: Mean myelin water fraction ± standard deviation in white matter and grey matter by sex and diagnosis

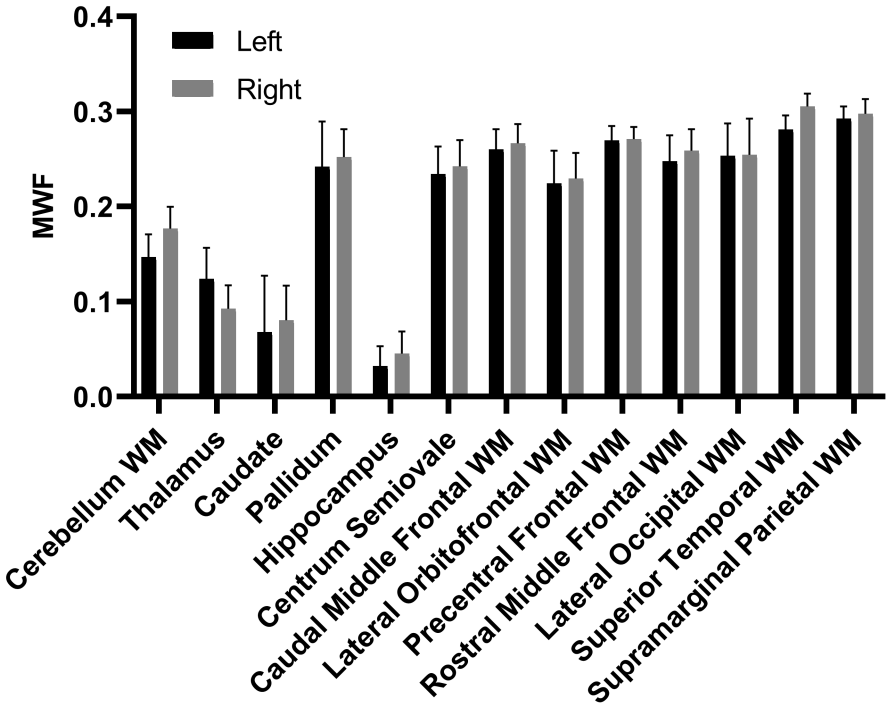

Figure 3.13: Mean myelin water fraction ± standard deviation by subregion: left and right. Two left-right subregions were significantly different: cerebellum white matter and superior temporal white matter.

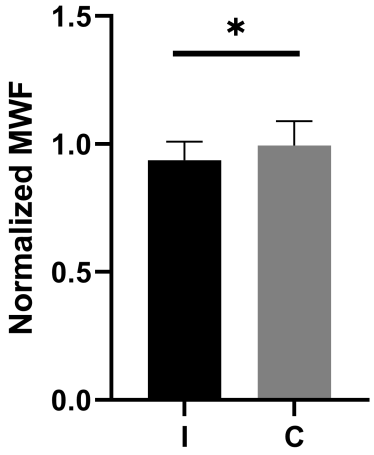

Figure 3.14: Mean myelin water fraction ± standard deviation by region of interest with decreased ipsilateral myelin water fraction.

3.5 Correlations Between Results

3.5.1 Quantitative MRI

Figure 3.15 summarizes the Pearson correlation values within and between; T_1, T_2, and MWF; in white matter and grey matter. Figure 3.16 depicts the Pearson correlation graphs of T_1, T_2, and MWF within white matter and within grey matter. These analyses were completed to validate internal consistency between the quantitative maps coming from the same DESPOT volumes. Table 2.3 summarizes the meaning of the shorthand notation for each measurement.

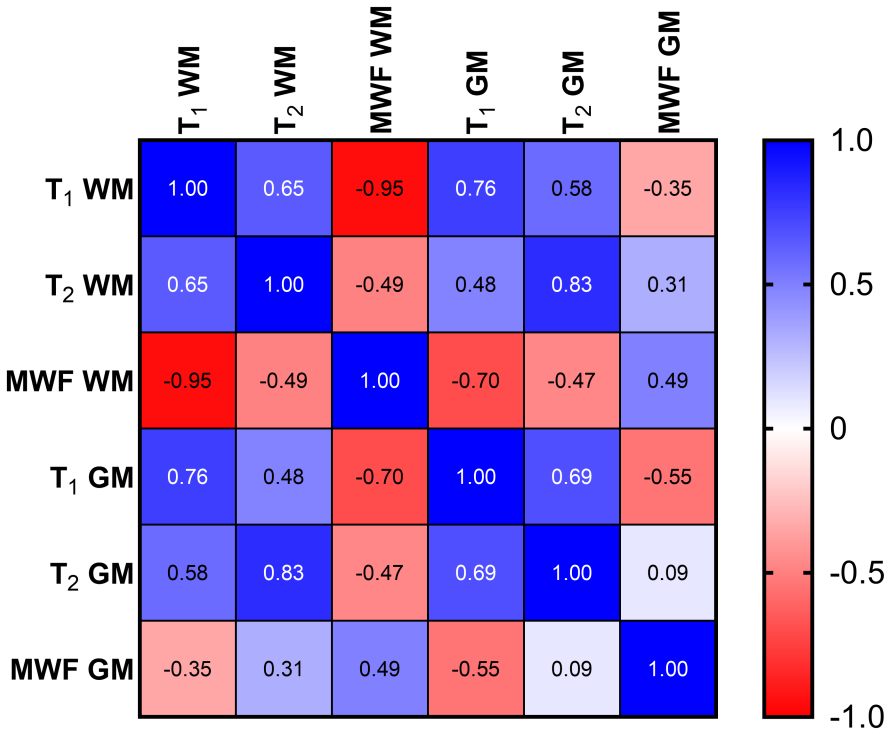

Figure 3.15: Pearson correlations within and between; T_1, T_2, and myelin water fraction; in white matter and grey matter

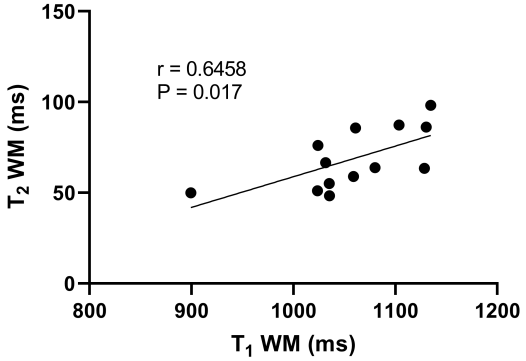

(a) T_2 white matter versus T_1 white matter

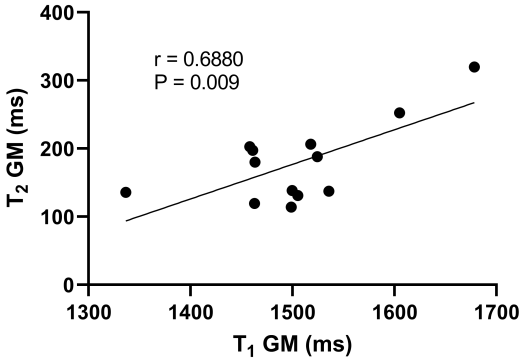

(b) T_2 grey matter versus T_1 grey matter

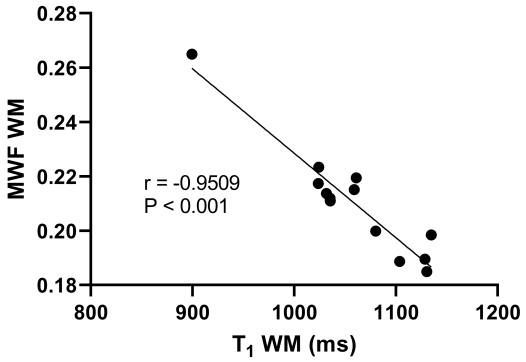

(c) MWF white matter versus T_1 white matter

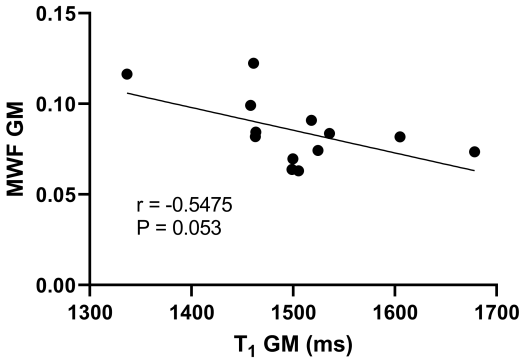

(d) MWF grey matter versus T_1 grey matter

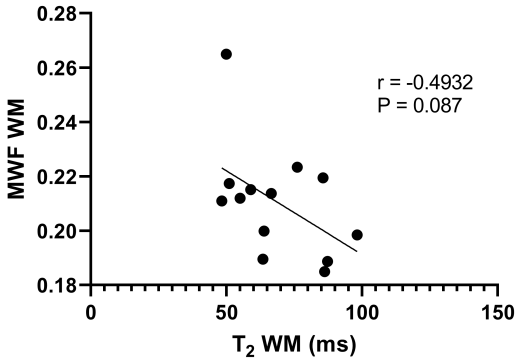

(e) MWF white matter versus T_2 white matter

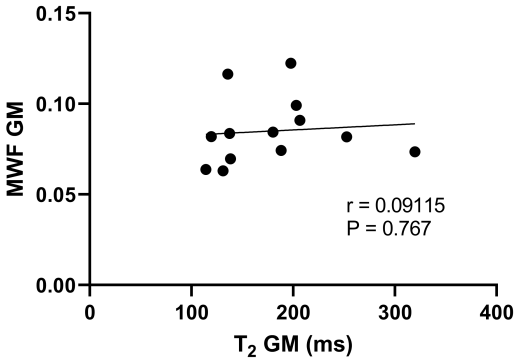

(f) MWF grey matter versus T_2 grey matter

Figure 3.16: Correlations in white matter and grey matter between T_1, T_2, and myelin water fraction

Quantitative MRI by Depression Score Threshold

A threshold of 7 on the Montgomery-Åsberg Depression Rating Scale yields 7 patients without evidence for depression and 6 patients with mild or moderate depression (Table 3.1). Welch's two-tailed t-tests for T_1, T_2, and MWF in white matter indicate no significant differences between patients above and below this depression score threshold.

Quantitative MRI by Cognitive Score Threshold

A threshold of 50 percent on the Cambridge Brain Sciences 12-test battery of tests yields 5 patients below and 8 patients above, based on their mean percentile (Figure 3.3). Welch's two-tailed t-tests for T_1, T_2, and MWF in white matter indicate no significant differences between patients above and below this threshold.

Measurements by Qualitative MRI Threshold

In accordance with Table 3.4, there are 6 patients with few to no findings (patients 1–4, 8, and 12) and 7 patients with many findings (patients 5–7, 9–11, and 13). A two-tailed t-test between depression scores of these two groups is not significant (P = 0.6412). Similarly, a two-tailed t-test between cognitive scores of these two groups is not significant (P = 0.2015). Furthermore, in quantitative MRI within white matter, two-tailed t-tests for T_1 (P = 0.2856), T_2 (P = 0.0947), and MWF (P = 0.2081) are not significant.

3.5.2 All Measurements

The Friedman test for agreement by ranking 1–13 across each measurement (Figure 3.17) was used following the ranking outlined in Table 2.3. The Friedman test indicates a significant difference between rankings by patient considering the 10 measurements (P = 0.0006). This indicates agreement between the rankings of measurement between patients. Figure 3.18 indicates the correlation by Spearman correlations between these 10 measurements.

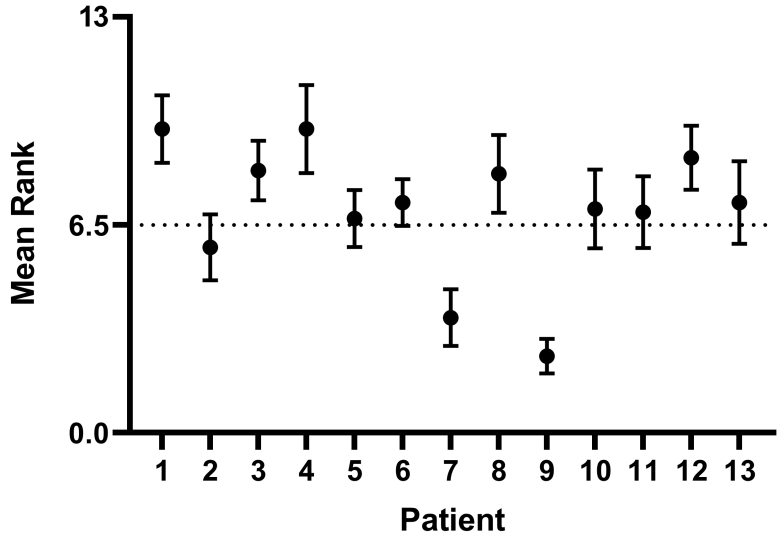

Figure 3.17: Mean rank of 10 measurements ± standard error by patient

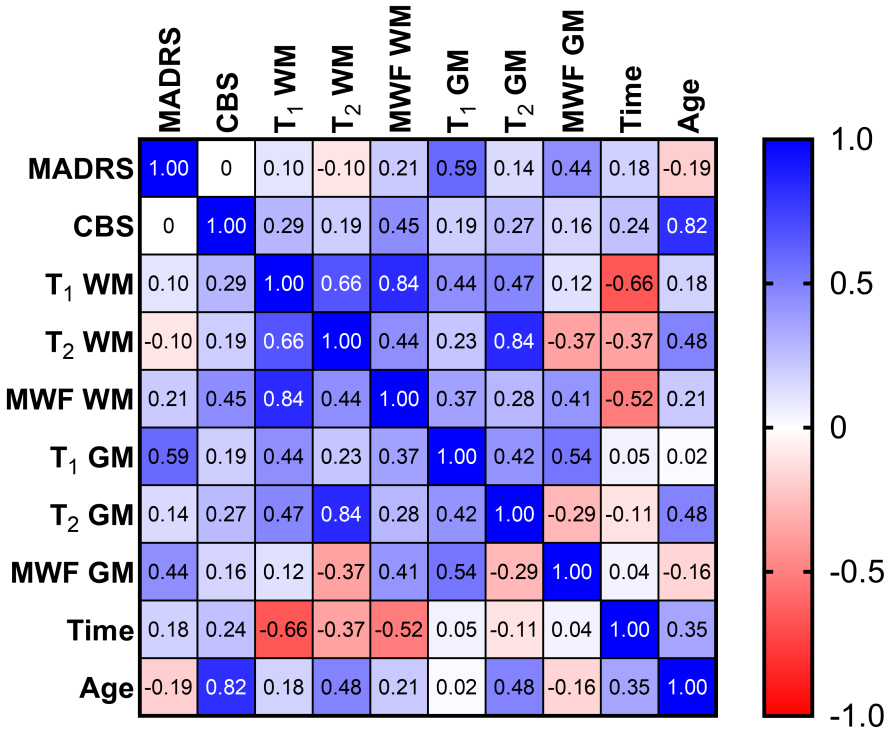

Figure 3.18: Spearman correlations between all 10 measurements

Chapter 4

Discussion

4.1 Summary

Across sixteen comparisons to evaluate differences in eight quantitative measurements by sex and by diagnosis, there is just one significant difference in measurements by sex and there are no significant differences in measurements by diagnosis. This gives confidence to consider all 13 patients together, independent of their sex or diagnosis, to better understand how TMA affects their brain health, despite prolonged remission, at different ages and durations of living with their vascular burden. Even though the sample size is small and there are no controls at this point in the longitudinal observational study, several interesting results are reported which help elucidate the poorly understood long-term impact of thrombotic thrombocytopenic purpura and atypical haemolytic uremic syndrome on the brain. The key findings of this thesis are highlighted in the following subsections.

4.1.1 Depression

According to Statistics Canada [119], 5.4% of Canadians experienced a mood disorder in the past 12 months with 4.7% being major depression. Furthermore, 11% of Canadians have met the criteria for major depression at some point in their lifetime [119]. In this study, using the

Montgomery-Åsberg Depression Rating Scale, nearly half of the participants (6/13) exhibited depression scores indicating mild or moderate depression (Table 3.1). This is in stark contrast to the incidence of depression in the Canadian population. When conducting a Fisher's exact test, considering a randomly selected group of 13 Canadians where 1 individual meets the criteria for mild, moderate, or severe depression, there is no significant difference for the incidence of depression in these patients (P = 0.073), however a larger sample size may be more conclusive. The Montgomery-Åsberg Depression Rating Scale is assessed from a clinical interview with the patient and the total score is the sum over the ten assessments. Consequently, the comparison of depression scores between patients may be limited by patient-specific sensitivity to expressing or not expressing how they feel. There was a significant difference in the mean scores by assessment which indicates a tendency for TTP or aHUS to affect the patients' mental health in specific ways. Specifically, the assessment, concentration difficulties, was the highest average score (2.3/6) and 84.6% of patients (11/13) reported non-zero scores (Table 3.2). The mean response in this assessment corresponds to the "worsening of occasional difficulties in collecting one's thoughts" [90].

4.1.2 Cognition

Considering the group of patients as a whole, there is no evidence of cognitive impairment in the 12-test battery by Cambridge Brain Sciences. There are 5 patients below the 50th percentile, but none of their mean percentiles lie outside one standard deviation of the age- and sex-matched population mean in the control database (Figure 3.3). There were no significant differences between percentiles by test or by category of test. This indicates that cognitive ability is no different among the three cognitive domains tested by Cambridge Brain Sciences. Conclusions from this cognitive testing in the correlation between results may be limited by the variation in time between the date of completing the assessment and the date of the MRI scan. Although the majority of patients completed the assessment within one week of the scan, there were three patients that completed the assessment beyond one month from the scan. The

comparison of cognitive percentile by sex yielded the only significant difference among the sixteen comparisons by sex and by diagnosis in the study. Since the percentiles are corrected for sex and age, it may be that cognition is more impaired in males than in females in patients with either of the two vascular conditions. These findings agree with the common symptom of confusion in both vascular conditions [36].

4.1.3 Qualitative MRI

Abnormalities in qualitative MRI were comparable in patients with TTP and patients with aHUS (Table 3.4). White matter abnormalities were observed in 46.1% of patients (6/13) in the MPRAGE acquisition (T_1-weighted), with atrophy being the most common finding. Our evidence of atrophy and lesions despite prolonged remission is in contrast to a study involving MRI in patients with TTP by Meloni *et al.*, 2001 [120] which reported that such abnormalities are infrequent and often reversible. Only one abnormality was observed in the RESOLVE acquisition (diffusion-weighted), which was the presence of chronic blood products; and abnormalities in vasculature observed in TOF MRA, including a thrombus and an aneurysm, were present in 30.1% of patients (4/13). Points of abnormal susceptibility were observed in 23.1% of patients (3/13) from SWI. Points of abnormal susceptibility may be microbleeds, which were reported in an MRI study with patients with TTP by Noorbakhsh-Sabet and Zand, 2016 [121]. Lastly, 76.9% of patients (10/13) had at least one abnormality in T2FLAIR (T_2-weighted). Abnormalities were presented by WMH ranging from small non-specific dots to larger infarcts. Our observations of WMH agree with an MRI case study from Sun *et al.*, 2005 [122]. Qualitative findings presented in this thesis agree with prior investigations and add further insight to how the brain is affected. To our knowledge, there has not been a study before this one that has investigated T_1, T_2, and MWF in the brains of individuals with TMA.

The anatomical regions of WMH detected in T2FLAIR defined the regions of interest for subregions in subsequent analysis with quantitative MRI. The regions of interest within the predetermined subregions provided a thorough perspective on WMH throughout the brain be-

cause the majority of findings were considered (87.5%). These regions of interest were selected based on where the white matter hyperintensity was present and there were 4 additional regions of interest not considered in the analysis. These were the precuneus, postcentral parietal lobe, pars triangularis, and putamen. Each of these regions were adjacent to the selected regions of interest in the analysis. Though the subregions were automatically parcellated, the identification of the subregion for each region of interest was manual. Furthermore, patient 5 was recently diagnosed with multiple sclerosis, so the conclusions drawn from this dataset are unclear whether the findings are attributed to MS, TTP, or both. The measurements are still considered in the overall comparisons, but findings from their brain are not considered for case by case comparison.

4.1.4 T_1, T_2, and Myelin Water Fraction

Quantitative techniques are capable of detecting changes that may not be observable in a clinical, qualitative MRI protocol. In this study, quantitative MRI to measure T_1, T_2, and MWF was utilized to verify findings in qualitative MRI sequences and to compare trends within all quantitative measurements including the scores of depression and cognition.

Three limitations must be addressed to the otherwise robust quantitative maps. Motion was not accounted for. Measurements of T_1, T_2, and MWF are determined from data collected from 6–18 minutes of scanning time. Correcting for slight motion over these 18 minutes may improve the findings from the resulting quantitative maps. Secondly, the quality of T_2, and MWF maps in patients 1 and 3 may be lower than those of other patients because two distinct phase increments were not used in the DESPOT2 acquisition. The same phase increment was erroneously repeated. Thirdly, despite its abilities to detect changes in myelination, mcDESPOT has been reported to overestimate MWF [111]. This motivates technique-specific comparisons in findings in myelin water imaging.

The reported values of T_1 and T_2 relaxation times vary by sequence used and manufacturer [75]. Nonetheless, this study demonstrated values of T_1 and T_2 in grey and white matter com-

parable to literature [74, 123], as seen between Table 1.2 and Table 3.5. Furthermore these values were consistent across participants in the study, using the same image analysis. With regards to the measurement of MWF, there is greater variability based on the sequence and analysis used [111] than there is with T_1 and T_2 due to the added complexity of fitting the multi-component model. Other studies using mcDESPOT for determining MWF have demonstrated comparable results [88]. In the model, exchange between intra- and extra-cellular water is considered however magnetization transfer is not. Grey matter MWF may be high due to the inability to model regions of inherently low myelin, like in CSF. Pearson correlations between these three measurements in white matter and grey matter, though generally significant, are not surprising due to the T_1, T_2, and MWF measurements coming from the same data. Interestingly, MWF in white matter was most strongly correlated with T_1 in the white matter (R^2 = 0.9025, $P < 0.001$). T_1 maps have also been proposed as a potential marker of myelin content based on shorter T_1 relaxation times in myelin water compared to axonal and extracellular water [124]. Although potentially less specific to myelin than MWF, T_1 maps have the advantage of significantly shorter acquisitions times (6 minutes versus 18 minutes).

T_1, T_2, and MWF in white matter were compared between patients based on the thresholds set in the qualitative MRI observations to evaluate agreement between qualitative findings and changes throughout white matter. All three of these comparisons by threshold in qualitative MRI were non-significant. With this sample size, there is no evidence that T_2 and MWF in white matter differ based on severity of qualitative MRI observations. However, T_2 in white matter shows some evidence of white matter changes based on the threshold (P = 0.0947). This may be because the most profuse findings in qualitative MRI came from T2FLAIR, a T_2-weighted image. The Spearman correlation between ranks from the Friedman test incorporating all ten measurements as outlined in Table 2.3, considering this binary classification in qualitative MRI observations, is significant with a moderate correlation (R^2 = 0.4354, P = 0.0141). An increased sample size will better elucidate the relationships between observations in qualitative MRI and quantitative MRI measurements throughout white matter.

Tissue Segmentation

T_1, T_2, and MWF were calculated by tissue; white matter, grey matter, and CSF. Conservative brain extractions and masks were produced using the first volume of DESPOT1 and tissue-specific masks were generated using MPRAGE to produce masks for white matter, grey matter, and CSF. Volumes of respective tissue (Table 3.5) somewhat agree with the literature [125] however CSF volume is overestimated due to some skull and neck incorporated in the mask beyond the fluid in the ventricles and subarachnoid space. White and grey matter masks from MPRAGE are more accurate than those from DESPOT1 or DESPOT2 due to a higher voxel resolution.

Subregion Segmentation

T_1, T_2, and MWF were calculated within the subregions outlined in Table 2.2. Consistency between left-right of subregions and variability between subregions for these measurements motivate the use of a well-established automatic segementation for subregion, such as the white matter parcellation produced from FreeSurfer. In left-right comparisons of T_1, T_2, and MWF by subregion, 87.2% (34/39) were not significantly different. In subregions that contained white matter hyperintensities and increased T_2, the increased T_2 was significantly larger than the contralateral ROI. Similary, in subregions that contained white matter hyperintensities and decreased MWF, the decreased MWF was significantly smaller than the contralateral ROI. This significant difference using the contralateral region in individual patients as an internal control suggests that both T_2 and MWF are capable of distinguishing white matter degradation in patients with TTP and aHUS. These are promising first results in anticipation of future analysis that includes age-matched healthy controls.

4.1.5 Correlations Between Results

The significant finding in the Friedman test indicates agreement between measurements based on the demyelination hypothesis. Restated, white matter is damaged due to TTP or aHUS, which increases T_1 and T_2, and decreases MWF. Additionally, the hypothesis is that these effects become worse with age and time living with the diagnosis despite prolonged remission. Furthermore, elevated depression scores and decreased cognitive scores are expected to occur. A total of ten measurements were included in this analysis and the corresponding ranking based on the demyelination hypothesis are outlined in Table 2.3. By the Friedman test, cognitive scores agree with the three MRI measurements in white matter (P = 0.0037). This is a greater agreement than depression scores with only the three MRI measurements in white matter (P = 0.0152). The three MRI measurements agree with each other when considering those in white matter and in grey matter (P = 0.0008). The best agreement between rankings, defined by the lowest P value, was all ten measurements excluding time (P = 0.0001). This may indicate that T_1, T_2, and MWF changes occur, but do not worsen over time.

Although there is agreement based on the demyelination hypothesis, there may be some patients who respond differently to TTP or aHUS. This is difficult to tease out in a small sample, however processes of dysmyelination and hypermyelination are also possible. Patient 4 is a potential case study for one of these latter two processes because their cognitive score is among the lowest (30%) while their MWF is the highest (0.25 in white matter). The strongest imaging correlates with depression score, cognitive score, time, and age were respectively T_1 in grey matter, MWF in white matter, T_1 in white matter, and T_2 in both grey matter and white matter. In most cases, the strongest correlate with each measurement was an imaging measurement. However, the strongest correlate with age was the cognitive score. Scores are sex- and age-matched to the database of healthy controls so this correlation may indicate that TTP and aHUS affects cognition more in older patients. This finding may be because older patients have lived with their diagnosis for longer, as summarized in Table 2.1. There are a few caveats that must be addressed in the ranking of measurements. Changes in white and grey

matter over lifetime are not linear as assumed by ranking. Rather, white matter peaks in fifth decade of life and grey matter declines [77]. Myelination follows a similar trend to white matter development, hence relaxation times and MWF may also be non-linear in nature. However, the rankings under the demyelination hypothesis indicate some interesting relationships for future investigation. The strongest correlation varying across imaging measurments motivates the use of all six quantitative MRI measurements in understanding how the brain is affected in TMA. This demonstrates the value of a multi-parametric approach that includes T_1, T_2, and MWF.

4.2 Next Steps

4.2.1 Controls

The goal is to recruit 30 patients in total and to have age-matched healthy controls for direct comparison using the same methodology. Healthy controls will be age-matched within two years of patients and they will be recruited following the same exclusion criteria. As presented in this thesis, the subregion analysis was limited to those regions of interest identified by the neuroradiologist and there may be additional regions of interest detected in these quantitative MRI approaches. Additional data in healthy controls will help elucidate natural left-right variations by subregion in quantitative MRI and may reveal additional abnormal subregions in patients. Statistical evaluation will be conducted by Welch's two-tailed t-tests between tissue- and subregion-specific quantitative measurements between patients and controls.

4.2.2 Follow-Up Scans

As depicted in the protocol timeline in Figure 2.1, patients will receive follow-up scans, along with repeated depression assessment and cognitive testing, at six and twelve months from their first timepoint. Cognitive testing will be evaluated within the same week of the MRI scan like the depression assessment. Though most patients completed their cognitive testing within

a week, there were a few that took 1–2 months. To best compare findings from cognitive testing and the MRI scans, it is important the brain is in the same state of health. This study was limited by assuming the brain was in the same state of health between cognitive testing and the MRI scan, despite up to two months of lag between. However, the full battery will continue to be implemented due to the occasional invalid scores in tests seen in this group of patients. If TTP or aHUS continues to worsen neurocognitive outcomes, different measures of white matter, such as decreased MWF in regions of interest, may be observable at each consecutive timepoint. Statistical evaluation will be conducted by repeated measures ANOVA of measurements (including MADRS score; CBS percentile; and T_1, T_2, and MWF in white matter and regions of interest).

4.2.3 Diffusion Tensor Imaging

Diffusion tensor imaging (DTI) relies on the diffusion of water molecules which behave differently by tissue based on how constrained the molecules are to freely move. Since the brain is mostly water, like the rest of the body, a strong understanding of tissue microstructure can be obtained based on the behaviour of water. One of the measurements in DTI is fractional anisotropy (FA), which is a unitless measurement (0–1) that indicates the directionality of water diffusion in tissue. Two extremes in the behaviour of water by tissue microstructure are demonstrated in the water within cerebral spinal fluid and in the water contained within the lipid bilayers of myelinated neurons. In CSF, such as in one of the four ventricles, water is not constrained and thus diffuses freely, resulting in a FA value approaching 0. Conversely, in the axon, water is constrained to flow in one direction, along the neuron, resulting in an FA value approaching 1.

Diffusion-weighted images for DTI have been acquired (Figure 2.2), but not yet considered to the extent of the other methodologies presented. There is not a significant linear correlation between MWF and DTI measurements [126] which motivates including both MWI and DTI in the study. Though both assess white matter microstructure, the measurements may vary

because the MWF is not altered by fibre orientation like fractional FA: perpendicular fibres in a given voxel may reduce FA, however the MWF will not change. The added value of DTI over MWI is that it can be used to generate white matter tracts. Tractography reveals pathways of white matter throughout the brain. Findings in RESOLVE (such as white matter regions of high diffusivity) and MPRAGE (such as regions of white matter atrophy) will be used to guide tractography. White matter trajectories may be impeded and FA may be decreased due to damaged white matter.

4.2.4 Arterial Spin Labeling

Arterial spin labeling (ASL) is another emerging quantitative MRI technique for clinical applications. It is commonly used to measure cerebral blood flow (CBF) (measured in ml/100g/min) in patients with stroke, dementia, epilepsy, and other psychiatric diseases [127]. Unlike other imaging modalities to evaluate CBF, no contrast agents or radiation are involved. Incoming arterial blood to the brain is tagged prior to splitting into smaller arteries. The water in this arterial blood is magnetically labelled by a 180-degree radiofrequency pulse. Phase is accumulated as the blood flows and diffuses throughout the brain. Faster flowing blood picks up more phase, and after a period of time called the transit time an image called the tag image is acquired where this tagged blood is now in the slice of interest. Another image called the control image is acquired in the same slice but without the 180-degree radiofrequency pulse. The control image is subtracted from the tag image and a CBF measurement can be calculated based on the amount of phase accumulated in the vasculature [128, 129].

A pseudo-continuous ASL (pCASL) for ASL has been acquired, but not yet considered to the extent of the other methodologies presented. The approach by pCASL provides higher signal-to-noise than pulsed arterial spin labeling (PASL) [130]. In patients with TTP and aHUS, who are in prolonged remission, significant differences in whole-brain CBF are not expected in comparison to healthy controls. However, there may be differences in CBF within subregions of the brain vasculature. Findings from TOF MRA (such as thrombi) and SWI (such

as microbleeds) will be used to guide region of interest analysis in ASL to compare ipsilateral-contralateral region-specific CBF. Additionally, future studies will compare ASL to findings in computed tomography.

4.2.5 Computed Tomography Perfusion

CTP has been acquired, but not yet considered to the extent of the other methodologies presented. Unlike the acquisitions in the comprehensive MRI protocol, CT perfusion is capable of measuring blood brain barrier permeability (BBB-P). Preliminary work [65] in a separate cohort of patients with TTP demonstrated a compromised BBB-P despite prolonged remission. This unexpected finding will be retested. BBB-P will be compared between patients and controls and it will be correlated with the established measurements including MWF in white matter and region of interest.

4.2.6 Future Direction

There are many interesting avenues for future work that we intend to pursue. Beyond the current scope of the study, the following four avenues could be investigated to enhance the understanding of neurocognitive outcomes in TTP and aHUS. 1) Additional MRI techniques: The existing MRI protocol could be expanded upon or modified to accommodate the following considerations: neurite orientation dispersion and density imaging (NODDI), to model axon density and dispersion in white matter [131]; and resting state functional MRI (fMRI), to evaluate functional networks and their relationship to neurocognitive findings. 2) PET/MR: Positron emission tomography (PET) is an imaging modality that can be added with no additional scanning time on systems that offer simultaneous PET/MR. Relevant radioactive tracers would include ^{11}C-UCB-J for synaptic density [132], ^{18}F-FEPPA for inflammation [133], and FDG for metabolism [134]. 3) Machine learning: A classifier could be established to evaluate whether or not patients and controls can be accurately identified based on features selected throughout the comprehensive MRI protocol. If the five strongest features are chosen, hypo-

thetically there might be one feature from RESOLVE, two from T2FLAIR, one from the T_1 map, and one from the MWF map. 4) Additional cognitive testing: The Montreal Cognitive Assessment (MoCA) is easy to administer and it can detect mild cognitive impairment and Alzheimer's disease [135].

Treatment Guidance

With a greater sample size, the effect of treatment on neurocognitive outcomes can be observed. Treatment of TTP primarily involves plasma exchange therapy in conjunction with various medications. Two novel medications of interest are recombinant ADAMTS13 [50] and caplacizumab [61, 62]. However, studies have not utilized a comprehensive protocol focusing on quantitative MRI, as presented in this thesis, and future work aims to replicate these findings to strengthen treatment guidance.

4.3 Conclusion

Persistent neurocognitive changes, despite prolonged remission, are not unique to thrombotic thrombocytopenic purpura and atypical haemolytic uremic syndrome. The protocol demonstrated in this study has the potential to elucidate the poorly-understood neurocognitive outcomes in other vascular and immunocompromised diseases; such as vasculitis and lupus. Each aspect of this investigation has contributed to a deeper understanding of how these two devistating manifestations of thrombotic microangiopathy impact the brain. The comprehensive MRI protocol can see things that cannot be detected in depression assessments, cognitive testing, or even routine MRI scans. Findings in quantitative MRI may preclude the worsening of neurocognitive outcomes measured by depression assessments, cognitive testing, and qualitative MRI. Agreement between the neuroradiologist observations and quantitative measurements strengthens our findings. These include higher incidence of depression, prevalence of white matter hyperintensities from small non-specific dots to larger infarcts, and decreased myelin

water fraction in regions of white matter hyperintensity. Patients with thrombotic thrombocytopenic purpura and atypical haemolytic uremic syndrome experience similar neurocognitive outcomes despite being in remission. Upcoming follow-up scans and comparisons to healthy controls aim to strengthen the findings presented in this thesis.

References

[1] Eli Moschcowitz. An acute febrile pleiochromic anemia with hyaline thrombosis of the terminal arterioles and capillaries: An undescribed disease. *Archives of Internal Medicine*, 36(1):89–93, 1925. ISSN 15383679. doi: 10.1001/archinte.1925.00120130092009. URL https://pubmed.ncbi.nlm.nih.gov/14631522/.

[2] Mark Levandovsky, Danielle Harvey, Primo Lara, and Ted Wun. Thrombotic thrombocytopenic purpura-hemolytic uremic syndrome (TTP-HUS): A 24-year clinical experience with 178 patients. *Journal of Hematology and Oncology*, 1(1), 2008. ISSN 17568722. doi: 10.1186/1756-8722-1-23. URL https://pubmed.ncbi.nlm.nih.gov/19046460/.

[3] David P. Miller, James A. Kaye, Kathleen Shea, Najat Ziyadeh, Clorinda Cali, Corri Black, and Alexander M. Walker. Incidence of Thrombotic Thrombocytopenic Purpura/Hemolytic Uremic Syndrome. *Epidemiology*, 15(2):208–215, Mar 2004. ISSN 10443983. doi: 10.1097/01.ede.0000113273.14807.53. URL https://www.ncbi.nlm.nih.gov/pubmed/15127914.

[4] Léanne Swart, Elise Schapkaitz, and Johnny N. Mahlangu. Thrombotic thrombocytopenic purpura: A 5-year tertiary care centre experience. *Journal of Clinical Apheresis*, 34:44–50, Feb 2019. ISSN 0733-2459. doi: 10.1002/jca.21673. URL https://www.ncbi.nlm.nih.gov/pubmed/30536422.

[5] Yoshihiro Fujimura and Masanori Matsumoto. Registry of 919 patients with throm-

botic microangiopathies across Japan: Database of Nara Medical University during 1998-2008. *Internal Medicine*, 49(1):7–15, 2010. ISSN 09182918. doi: 10.2169/internalmedicine.49.2706. URL https://pubmed.ncbi.nlm.nih.gov/20045995/.

[6] Barbara Plaimauer, Jakob Fuhrmann, Gabriele Mohr, Waltraud Wernhart, Katharina Bruno, Silvia Ferrari, Christian Konetschny, Gerhard Antoine, Manfred Rieger, and Friedrich Scheiflinger. Modulation of ADAMTS13 secretion and specific activity by a combination of common amino acid polymorphisms and a missense mutation. *Blood*, 107(1):118–125, 2006. ISSN 00064971. doi: 10.1182/blood-2005-06-2482. URL https://pubmed.ncbi.nlm.nih.gov/16160007/.

[7] Marie Moatti-Cohen, Céline Garrec, Martine Wolf, Pierre Boisseau, Lionel Galicier, Elie Azoulay, Alain Stepanian, Yahsou Delmas, Eric Rondeau, Stéphane Bezieau, Paul Coppo, and Agnès Veyradier. Unexpected frequency of Upshaw-Schulman syndrome in pregnancy-onset thrombotic thrombocytopenic purpura. *Blood*, 119(24):5888–5897, Jun 2012. ISSN 00064971. doi: 10.1182/blood-2012-02-408914. URL https://www.ncbi.nlm.nih.gov/pubmed/22547583.

[8] J. E. Sadler. Von Willebrand factor, ADAMTS13, and thrombotic thrombocytopenic purpura. *Blood*, 112(1):11–18, Feb 2008. ISSN 00064971. doi: 10.1182/blood-2008-02-078170. URL https://www.ncbi.nlm.nih.gov/pubmed/18574040.

[9] Marie Scully, Helen Yarranton, Ri Liesner, Jamie Cavenagh, Beverley Hunt, Sylvia Benjamin, David Bevan, Ian Mackie, and Samuel Machin. Regional UK TTP Registry: Correlation with laboratory ADAMTS 13 analysis and clinical features. *British Journal of Haematology*, 142(5):819–826, 2008. ISSN 00071048. doi: 10.1111/j.1365-2141.2008.07276.x. URL https://pubmed.ncbi.nlm.nih.gov/18637802/.

[10] Bérangère S. Joly, Paul Coppo, and Agnès Veyradier. Thrombotic thrombocy-

topenic purpura. *Blood*, 129(21):2836–2846, May 2017. ISSN 15280020. doi: 10.1182/blood-2016-10-709857. URL https://www.ncbi.nlm.nih.gov/pubmed/28416507.

[11] Karlos Z. Oregel, Jeremy Ramdial, and Stefan Glück. Nonsteroidal anti-inflammatory drug induced thrombotic thrombocytopenic purpura. *Clinical Medicine Insights: Blood Disorders*, 6:19–22, Nov 2013. ISSN 1179545X. doi: 10.4137/CMBd.s12843. URL https://www.ncbi.nlm.nih.gov/pubmed/25512716.

[12] K. Hamasaki, Toshim Mimura, H. Kanda, K. Kubo, K. Setoguchi, T. Satoh, Y. Misaki, and K. Yamamoto. Systemic lupus erythematosus and thrombotic thrombocytopenic purpura: A case report and literature review. *Clinical Rheumatology*, 22(4-5):355–358, 2003. ISSN 07703198. doi: 10.1007/s10067-003-0742-1. URL https://pubmed.ncbi.nlm.nih.gov/14579168/.

[13] Howard Trachtman, Catherine Austin, Maria Lewinski, and Rolf A.K. Stahl. Renal and neurological involvement in typical Shiga toxin-associated HUS. *Nature Reviews Nephrology*, 8(11):658–669, 2012. ISSN 17595061. doi: 10.1038/nrneph.2012.196. URL https://pubmed.ncbi.nlm.nih.gov/22986362/.

[14] Boldtsetseg Tserenpuntsag, Hwa Gan Chang, Perry F. Smith, and Dale L. Morse. Hemolytic uremic syndrome risk and Escherichia coli O157:H7. *Emerging Infectious Diseases*, 11(12):1955–1957, 2005. ISSN 10806059. doi: 10.3201/eid1112.050607. URL https://pubmed.ncbi.nlm.nih.gov/16485489/.

[15] Catherine Joseph and Jyothsna Gattineni. Complement disorders and hemolytic uremic syndrome. *Current Opinion in Pediatrics*, 25(2):209–215, 2013. ISSN 10408703. doi: 10.1097/MOP.0b013e32835df48a. URL https://pubmed.ncbi.nlm.nih.gov/23399570/.

[16] Mihály Józsi, Stefanie Strobel, Hans Martin Dahse, Wei Shih Liu, Peter F. Hoyer, Martin

Oppermann, Christine Skerka, and Peter F. Zipfel. Anti-factor H autoantibodies block C-terminal recognition function of factor H in hemolytic uremic syndrome. *Blood*, 110 (5):1516–1518, 2007. ISSN 00064971. doi: 10.1182/blood-2007-02-071472. URL https://pubmed.ncbi.nlm.nih.gov/17495132/.

[17] Shuju Feng, Stephen J. Eyler, Yuzhou Zhang, Tara Maga, Carla M. Nester, Michael H. Kroll, Richard J. Smith, and Vahid Afshar-Kharghan. Partial ADAMTS13 deficiency in atypical hemolytic uremic syndrome. *Blood*, 122(8):1487–1493, 2013. ISSN 15280020. doi: 10.1182/blood-2013-03-492421. URL https://pubmed.ncbi.nlm.nih.gov/23847193/.

[18] Francisco Varela. Immune system as the body's brain. In *Mind and Life III: Emotions and Health*, Dharamsala, India, 1990.

[19] Fabian C. Verbij, Rob Fijnheer, Jan Voorberg, and Nicoletta Sorvillo. Acquired TTP: ADAMTS13 meets the immune system. *Blood Reviews*, 28(6):227–234, 2014. ISSN 15321681. doi: 10.1016/j.blre.2014.07.004. URL https://www.ncbi.nlm.nih.gov/pubmed/25213289.

[20] Suneel S. Apte. A disintegrin-like and metalloprotease (reprolysin type) with thrombospondin type 1 motifs: The ADAMTS family. *International Journal of Biochemistry and Cell Biology*, 36(6):981–985, 2004. ISSN 13572725. doi: 10.1016/j.biocel.2004.01.014. URL https://pubmed.ncbi.nlm.nih.gov/15094112/.

[21] Kazuo Fujikawa, Hiroshi Suzuki, Brad McMullen, and Dominic Chung. Purification of human von Willebrand factor-cleaving protease and its identification as a new member of the metalloproteinase family. *Blood*, 98(6):1662–1666, 2001. ISSN 00064971. doi: 10.1182/blood.V98.6.1662. URL https://pubmed.ncbi.nlm.nih.gov/11535495/.

[22] Han Mou Tsai and Eric Chun Yet Lian. Antibodies to von Willebrand factor-cleaving protease in acute thrombotic thrombocytopenic purpura. *New England Jour-*

nal of Medicine, 339(22):1585–1594, Jul 1998. ISSN 00284793. doi: 10.1056/NEJM199811263392203. URL https://pubmed.ncbi.nlm.nih.gov/9828246/.

[23] Gallia G. Levy, William C. Nichols, Eric C. Lian, Tatiana Foroud, Jeanette N. McClintick, Beth M. McGee, Angela Y. Yang, David R. Siemieniak, Kenneth R. Stark, Ralph Gruppo, Ravindra Sarode, Susan B. Shurin, Visalam Chandrasekaran, Sally P. Stabler, Hernan Sabio, Eric E. Bouhassira, Jefferson D. Upshaw, David Ginsburg, and Han Mou Tsai. Mutations in a member of the ADAMTS gene family cause thrombotic thrombocytopenic purpura. *Nature*, 413(6855):488–494, 2001. ISSN 00280836. doi: 10.1038/35097008. URL https://pubmed.ncbi.nlm.nih.gov/11586351/.

[24] Masahito Uemura, Kouko Tatsumi, Masanori Matsumoto, Masao Fujimoto, Tomomi Matsuyama, Masatoshi Ishikawa, Taka Aki Iwamoto, Toshio Mori, Akio Wanaka, Hiroshi Fukui, and Yoshihiro Fujimura. Localization of ADAMTS13 to the stellate cells of human liver. *Blood*, 106(3):922–924, 2005. ISSN 00064971. doi: 10.1182/blood-2005-01-0152. URL https://pubmed.ncbi.nlm.nih.gov/15855280/.

[25] Dezhi Shang, X. Wu Zheng, Masami Niiya, and X. Long Zheng. Apical sorting of ADAMTS13 in vascular endothelial cells and Madin-Darby canine kidney cells depends on the CUB domains and their association with lipid rafts. *Blood*, 108(7):2207–2215, 2006. ISSN 00064971. doi: 10.1182/blood-2006-02-002139. URL https://pubmed.ncbi.nlm.nih.gov/16597588/.

[26] Stefano Lancellotti, Maria Basso, and Raimondo De Cristofaro. Proteolytic processing of Von Willebrand Factor by Adamts13 and Leukocyte Proteases. *Mediterranean Journal of Hematology and Infectious Diseases*, 5(1), 2013. ISSN 20353006. doi: 10.4084/mjhid.2013.058. URL https://pubmed.ncbi.nlm.nih.gov/24106608/.

[27] National Health Service. What is plasma? URL https://www.blood.co.uk/why-give-blood/how-blood-is-used/blood-components/plasma/.

[28] Tamika M. Burrus, Jay Mandrekar, Eelco F. M. Wijdicks, and Alejandro A. Rabinstein. Renal failure and posterior reversible encephalopathy syndrome in patients with thrombotic thrombocytopenic purpura. *Archives of Neurology*, 67(7):831–834, Jul 2010. ISSN 00039942. doi: 10.1001/archneurol.2010.119. URL https://www.ncbi.nlm.nih.gov/pubmed/20625089.

[29] Harshvardhan Upreti, Jamil Kasmani, Kathryn Dane, Evan M Braunstein, Michael B Streiff, Satish Shanbhag, Alison R Moliterno, C. John Sperati, Rebecca F Gottesman, Robert A Brodsky, Thomas S Kickler, and Shruti Chaturvedi. Reduced ADAMTS13 activity during TTP remission is associated with stroke in TTP survivors. *Blood*, 134 (13):1037–1045, 2019. ISSN 00064971. doi: 10.1182/blood.2019001056. URL https://www.ncbi.nlm.nih.gov/pubmed/31431443.

[30] Jason Aboudi Mouabbi, Rami Zein, Zyad Kafri, Ayad Al-Katib, and Tarik Hadid. Thrombotic thrombocytopenic purpura presenting as acute coronary syndrome. *Clinical Case Reports*, 4(8):736–739, 2016. ISSN 2050-0904. doi: 10.1002/ccr3.606. URL https://pubmed.ncbi.nlm.nih.gov/27525072/.

[31] Szymon L Wiernek, Bo Jiang, Gregory M Gustafson, and Xuming Dai. Cardiac implications of thrombotic thrombocytopenic purpura. *World Journal of Cardiology*, 10 (12):254–266, 2018. ISSN 1949-8462. doi: 10.4330/wjc.v10.i12.254. URL https://pubmed.ncbi.nlm.nih.gov/30622684/.

[32] Jessica A. Reese, Darrshini S. Muthurajah, Johanna A.Kremer Hovinga, Sara K. Vesely, Deirdra R. Terrell, and James N. George. Children and adults with thrombotic thrombocytopenic purpura associated with severe, acquired Adamts13 deficiency: Comparison of incidence, demographic and clinical features. *Pediatric Blood and Cancer*, 60(10):1676–1682, 2013. ISSN 15455009. doi: 10.1002/pbc.24612. URL https://pubmed.ncbi.nlm.nih.gov/23729372/.

[33] Rohit Bakshi, Zubair A. Shaikh, Vernice E. Bates, and Peter R. Kinkel. Thrombotic thrombocytopenic purpura: Brain CT and MRI findings in 12 patients. *Neurology*, 52 (6):1285–1288, 1999. ISSN 00283878. doi: 10.1212/wnl.52.6.1285. URL https://www.ncbi.nlm.nih.gov/pubmed/10214762.

[34] Sara K. Vesely, April S. Kennedy, Qurana F. Lewis, James G. Scott, Johanna A. Kremer Hovinga, Bernhard Lämmle, Deirdra R. Terrell, and James N. George. Cognitive deficits after recovery from thrombotic thrombocytopenic purpura. *Transfusion*, 49(6): 1092–1101, Jun 2009. ISSN 00411132. doi: 10.1111/j.1537-2995.2009.02101.x. URL https://www.ncbi.nlm.nih.gov/pubmed/19222817.

[35] Bowie Han, Evaren E. Page, Lauren M. Stewart, Cassandra C. Deford, James G. Scott, Lauren H. Schwartz, Jedidiah J. Perdue, Deirdra R. Terrell, Sara K. Vesely, and James N. George. Depression and cognitive impairment following recovery from thrombotic thrombocytopenic purpura. *American Journal of Hematology*, 90(8):709–714, 2015. ISSN 10968652. doi: 10.1002/ajh.24060. URL https://pubmed.ncbi.nlm.nih.gov/25975932/.

[36] Antoine Froissart, Marc Buffet, Agnès Veyradier, Pascale Poullin, François Provôt, Sandrine Malot, Michael Schwarzinger, Lionel Galicier, Philippe Vanhille, Jean Paul Vernant, Dominique Bordessoule, Bertrand Guidet, Elie Azoulay, Eric Mariotte, Eric Rondeau, Jean Paul Mira, Alain Wynckel, Karine Clabault, Gabriel Choukroun, Claire Presne, Jacques Pourrat, Mohamed Hamidou, and Paul Coppo. Efficacy and safety of first-line rituximab in severe, acquired thrombotic thrombocytopenic purpura with a suboptimal response to plasma exchange. Experience of the French Thrombotic Microangiopathies Reference Center. *Critical Care Medicine*, 40(1):104–111, 2012. ISSN 00903493. doi: 10.1097/CCM.0b013e31822e9d66. URL https://pubmed.ncbi.nlm.nih.gov/21926591/.

[37] E. Aksay, S. Kiyan, M. Ersel, and O. Hudaverdi. Thrombotic thrombocytopenic purpura

mimicking acute ischemic stroke. *Emergency Medicine Journal*, 23(9), 2006. ISSN 14720213. doi: 10.1136/emj.2006.036327. URL https://www.ncbi.nlm.nih.gov/pubmed/16921072.

[38] Christopher James Doig, Louis Girard, and Deirdre Jenkins. Thrombotic thrombocytopenic purpura masquerading as a stroke in a young man. *Canadian Medical Association Journal*, 191(47):E1306–E1309, 2019. ISSN 0820-3946. doi: 10.1503/cmaj.190981. URL https://www.ncbi.nlm.nih.gov/pubmed/31767706.

[39] Henny H Billett. Chapter 151 Hemoglobin and Hematocrit. *Clinical Methods: The History, Physical, and Laboratory Examinations. 3rd edition*, (151):718–719, 1990. doi: 10.1055/s-2004-821156. URL https://pubmed.ncbi.nlm.nih.gov/21250102/.

[40] Evaren E. Page, Johanna A. Kremer Hovinga, Deirdra R. Terrell, Sara K. Vesely, and James N. George. Thrombotic thrombocytopenic purpura: Diagnostic criteria, clinical features, and long-term outcomes from 1995 through 2015. *Blood Advances*, 1(10):590–600, Apr 2017. ISSN 24739537. doi: 10.1182/bloodadvances.2017005124. URL https://www.ncbi.nlm.nih.gov/pmc/articles/PMC5728353/.

[41] Ernest Beutler and Jill Waalen. The definition of anemia: What is the lower limit of normal of the blood hemoglobin concentration? *Blood*, 107(5):1747–1750, 2006. ISSN 00064971. doi: 10.1182/blood-2005-07-3046. URL https://pubmed.ncbi.nlm.nih.gov/16189263/.

[42] C. Giles. The Platelet Count and Mean Platelet Volume. *British Journal of Haematology*, 48(1):31–37, 1981. ISSN 13652141. doi: 10.1111/j.1365-2141.1981.00031.x. URL https://pubmed.ncbi.nlm.nih.gov/7248189/.

[43] Massimo Franchini and Pier Mannuccio Mannucci. Advantages and limits of ADAMTS13 testing in thrombotic thrombocytopenic purpura. *Blood Transfusion*, 6

(3):127–135, 2008. ISSN 17232007. doi: 10.2450/2008.0056-07. URL https://pubmed.ncbi.nlm.nih.gov/22244722/.

[44] Hiromichi Ishizashi, Hideo Yagi, Masanori Matsumoto, Kenji Soejima, Tomohiro Nakagaki, and Yoshihiro Fujimura. Quantitative Western blot analysis of plasma ADAMTS13 antigen in patients with Upshaw-Schulman syndrome. *Thrombosis Research*, 120 (3):381–386, 2007. ISSN 00493848. doi: 10.1016/j.thromres.2006.07.012. URL https://pubmed.ncbi.nlm.nih.gov/17030346/.

[45] Koichi Kokame, Yuko Nobe, Yoshihiro Kokubo, Akira Okayama, and Toshiyuki Miyata. FRETS-VWF73, a first fluorogenic substrate for ADAMTS13 assay. *British Journal of Haematology*, 129(1):93–100, 2005. ISSN 00071048. doi: 10.1111/j.1365-2141.2005.05420.x. URL https://pubmed.ncbi.nlm.nih.gov/15801961/.

[46] Manfred Rieger, Pier Mannuccio Mannucci, Johanna A. Kremer Hovinga, Andrea Herzog, Gabi Gerstenbauer, Christian Konetschny, Klaus Zimmermann, Inge Scharrer, Flora Peyvandi, Miriam Galbusera, Giuseppe Remuzzi, Martina Böhm, Barbara Plaimauer, Bernhard Lämmle, and Friedrich Scheiflinger. ADAMTS13 autoantibodies in patients with thrombotic microangiopathies and other immunomediated diseases. *Blood*, 106(4):1262–1267, 2005. ISSN 00064971. doi: 10.1182/blood-2004-11-4490. URL https://pubmed.ncbi.nlm.nih.gov/15890682/.

[47] Christoph Klaus, Barbara Plaimauer, Jan Dirk Studt, Friedrich Dorner, Bernhard Lämmle, Pier Mannuccio Mannucci, and Friedrich Scheiflinger. Epitope mapping of ADAMTS13 autoantibodies in acquired thrombotic thrombocytopenic purpura. *Blood*, 103(12):4514–4519, 2004. ISSN 00064971. doi: 10.1182/blood-2003-12-4165. URL https://pubmed.ncbi.nlm.nih.gov/14976043/.

[48] Mari R. Thomas, Rens de Groot, Marie A. Scully, and James T.B. Crawley. Pathogenicity of Anti-ADAMTS13 Autoantibodies in Acquired Thrombotic Thrombocytopenic

Purpura. *EBioMedicine*, 2(8):942–952, 2015. ISSN 23523964. doi: 10.1016/j.ebiom.2015.06.007. URL https://pubmed.ncbi.nlm.nih.gov/26425702/.

[49] Gail A. Rock, Kenneth H. Shumak, Noel A. Buskard, Victor S. Blanchette, John G. Kelton, Rama C. Nair, and Robert A. Spasoff. Comparison of Plasma Exchange with Plasma Infusion in the Treatment of Thrombotic Thrombocytopenic Purpura. *New England Journal of Medicine*, 325(6):393–397, Aug 1991. ISSN 0028-4793. doi: 10.1056/NEJM199108083250604. URL http://www.nejm.org/doi/abs/10.1056/NEJM199108083250604.

[50] James T.B. Crawley and Marie A. Scully. Thrombotic thrombocytopenic purpura: basic pathophysiology and therapeutic strategies. *Hematology / the Education Program of the American Society of Hematology. American Society of Hematology. Education Program*, 2013:292–299, 2013. ISSN 15204383. doi: 10.1182/asheducation-2013.1.292. URL https://pubmed.ncbi.nlm.nih.gov/24319194/.

[51] Christoph Licht, Gianluigi Ardissino, Gema Ariceta, David Cohen, J. Alexander Cole, Christoph Gasteyger, Larry A. Greenbaum, Sally Johnson, Masayo Ogawa, Franz Schaefer, Johan Vande Walle, and Véronique Frémeaux-Bacchi. The global aHUS registry: Methodology and initial patient characteristics. *BMC Nephrology*, 16(1), 2015. ISSN 14712369. doi: 10.1186/s12882-015-0195-1. URL https://pubmed.ncbi.nlm.nih.gov/26654630/.

[52] Miha Furlan, Rodolfo Robles, Beat Morselli, Pierre Sandoz, and Bernhard Lämmle. Recovery and half-life of von Willebrand factor-cleaving protease after plasma therapy in patients with thrombotic thrombocytopenic purpura. *Thrombosis and Haemostasis*, 81(1):8–13, 1999. ISSN 03406245. doi: 10.1055/s-0037-1614408. URL https://pubmed.ncbi.nlm.nih.gov/10348715/.

[53] Haifei Chen, Ailin Fu, Jing Wang, Tianqin Wu, Zhengyang Li, Jieqing Tang, Hong-

shi Shen, Jingjing Zhu, Jie Li, Qian Zhu, and Longmei Qing. Rituximab as first-line treatment for acquired thrombotic thrombocytopenic purpura. *Journal of International Medical Research*, 45(3):1253–1260, 2017. ISSN 14732300. doi: 10.1177/0300060517695646. URL https://pubmed.ncbi.nlm.nih.gov/28639502/.

[54] Matteo Boattini and Gaetano Procaccianti. Stroke due to typical thrombotic thrombocytopenic purpura treated successfully with intravenous thrombolysis and therapeutic plasma exchange. *BMJ Case Reports*, 2013. ISSN 1757790X. doi: 10.1136/bcr-2012-008426. URL https://www.ncbi.nlm.nih.gov/pubmed/23362068.

[55] Hiro Nakao, Akira Ishiguro, Nahoko Ikoma, Kentaro Nishi, Chemin Su, Hisaya Nakadate, Mitsuru Kubota, Masaki Hayakawa, and Masanori Matsumoto. Acquired idiopathic thrombotic thrombocytopenic purpura successfully treated with intravenous immunoglobulin and glucocorticoid. *Medicine (United States)*, 96(14), 2017. ISSN 15365964. doi: 10.1097/MD.0000000000006547. URL https://pubmed.ncbi.nlm.nih.gov/28383422/.

[56] François Beloncle, Marc Buffet, Jean Philippe Coindre, Nicolas Munoz-Bongrand, Sandrine Malot, Frédéric Pène, Jean Paul Mira, Lionel Galicier, Bertrand Guidet, Jean Luc Baudel, Jean François Subra, Aline Tanguy-Schmidt, Jacques Pourrat, Elie Azoulay, Agnès Veyradier, and Paul Coppo. Splenectomy and/or cyclophosphamide as salvage therapies in thrombotic thrombocytopenic purpura: The French TMA Reference Center experience. *Transfusion*, 52(11):2436–2444, 2012. ISSN 00411132. doi: 10.1111/j.1537-2995.2012.03578.x. URL https://pubmed.ncbi.nlm.nih.gov/22404639/.

[57] Alyssa Ziman, Michael Mitri, Ellen Klapper, Samuel H. Pepkowitz, and Dennis Goldfinger. Combination vincristine and plasma exchange as initial therapy in patients with thrombotic thrombocytopenic purpura: One institution's experience and review of the literature. 45(1):41–49, 2005. ISSN 00411132. doi: 10.1111/j.1537-2995.2005.03146.x. URL https://pubmed.ncbi.nlm.nih.gov/15647017/.

[58] Christopher J. Patriquin, Mari R. Thomas, Tina Dutt, Siobhan McGuckin, Piers A. Blombery, Tanya Cranfield, John P. Westwood, and Marie Scully. Bortezomib in the treatment of refractory thrombotic thrombocytopenic purpura. *British Journal of Haematology*, 173(5):779–785, 2016. ISSN 13652141. doi: 10.1111/bjh.13993. URL https://pubmed.ncbi.nlm.nih.gov/27009919/.

[59] Spero R. Cataland, Ming Jin, Shili Lin, Eric H. Kraut, James N. George, and Haifeng M. Wu. Effect of prophylactic cyclosporine therapy on ADAMTS13 biomarkers in patients with idiopathic thrombotic thrombocytopenic purpura. *American Journal of Hematology*, 83(12):911–915, 2008. ISSN 03618609. doi: 10.1002/ajh.21281. URL https://pubmed.ncbi.nlm.nih.gov/18821711/.

[60] Fernando C. Fervenza, Pietro A. Canetta, Sean J. Barbour, Richard A. Lafayette, Brad H. Rovin, Nabeel Aslam, Michelle A. Hladunewich, Maria V. Irazabal, Sanjeev Sethi, Debbie S. Gipson, Heather N. Reich, Paul Brenchley, Matthias Kretzler, Jai Radhakrishnan, Lee A. Hebert, Patrick E. Gipson, Leslie F. Thomas, Ellen T. McCarthy, Gerald B. Appel, J. Ashley Jefferson, Alfonso Eirin, John C. Lieske, Marie C. Hogan, Eddie L. Greene, John J. Dillon, Nelson Leung, John R. Sedor, Dana V. Rizk, Samuel S. Blumenthal, Lada B. Lasic, Luis A. Juncos, Dollie F. Green, James Simon, Amy N. Sussman, David Philibert, and Daniel C. Cattran. A Multicenter Randomized Controlled Trial of Rituximab versus Cyclosporine in the Treatment of Idiopathic Membranous Nephropathy (MENTOR). *Nephron*, 130(3):159–168, 2015. ISSN 22353186. doi: 10.1159/000430849. URL https://pubmed.ncbi.nlm.nih.gov/26087670/.

[61] Flora Peyvandi, Marie Scully, Johanna A. Kremer Hovinga, Spero Cataland, Paul Knöbl, Haifeng Wu, Andrea Artoni, John Paul Westwood, Magnus Mansouri Taleghani, Bernd Jilma, Filip Callewaert, Hans Ulrichts, Christian Duby, and Dominique Tersago. Caplacizumab for acquired thrombotic thrombocytopenic purpura. *New England Journal of*

Medicine, 374(6):511–522, Feb 2016. ISSN 15334406. doi: 10.1056/NEJMoa1505533. URL https://www.ncbi.nlm.nih.gov/pubmed/26863353.

[62] M. Scully, S. R. Cataland, F. Peyvandi, P. Coppo, P. Knöl, J. A. Kremer Hovinga, A. Metjian, J. De La Rubia, K. Pavenski, F. Callewaert, D. Biswas, H. De Winter, and R. K. Zeldin. Caplacizumab treatment for acquired thrombotic thrombocytopenic purpura. *New England Journal of Medicine*, 380(4):335–346, Jan 2019. ISSN 15334406. doi: 10.1056/NEJMoa1806311. URL https://www.ncbi.nlm.nih.gov/pubmed/30625070.

[63] Lova Sun, Johnathan Mack, Ang Li, Justine Ryu, Vivek A. Upadhyay, Lynne Uhl, Richard M. Kaufman, Christopher P. Stowell, Walter S. Dzik, Robert S. Makar, and Pavan K. Bendapudi. Predictors of relapse and efficacy of rituximab in immune thrombotic thrombocytopenic purpura. *Blood Advances*, 3(9):1512–1518, 2019. ISSN 24739537. doi: 10.1182/bloodadvances.2019031039. URL https://pubmed.ncbi.nlm.nih.gov/31076407/.

[64] Sumit Som, Cassandra C. Deford, Mandi L. Kaiser, Deirdra R. Terrell, Johanna A. Kremer Hovinga, Bernhard Lämmle, James N. George, and Sara K. Vesely. Decreasing frequency of plasma exchange complications in patients treated for thrombotic thrombocytopenic purpura-hemolytic uremic syndrome, 1996 to 2011. *Transfusion*, 52(12): 2525–2532, Dec 2012. ISSN 00411132. doi: 10.1111/j.1537-2995.2012.03646.x. URL https://www.ncbi.nlm.nih.gov/pubmed/22501034.

[65] J.G. Hamilton, T.Y. Lee, J.D. Thiessen, and S.H.S. Huang. Compromised blood brain barrier in patients with TTP by CT motivates further investigation using MRI. page 189, London, Ontario, 2019. Imaging Network Ontario. URL https://www.imno.ca/sites/default/files/ImNO2019Proceedings.pdf.

[66] T. Y. Lee, T. G. Purdie, and E. Stewart. CT imaging of angiogenesis. *Quarterly Journal*

of Nuclear Medicine, 47(3):171–187, 2003. ISSN 11243937. URL https://pubmed.ncbi.nlm.nih.gov/12897709/.

[67] Kohsuke Kudo, Satoshi Terae, Chietsugu Katoh, Masaki Oka, Tohru Shiga, Nagara Tamaki, and Kazuo Miyasaka. Quantitative cerebral blood flow measurement with dynamic perfusion CT using the vascular-pixel elimination method: Comparison with H215O positron emission tomography. *American Journal of Neuroradiology*, 24(3): 419–426, 2003. ISSN 01956108. URL https://pubmed.ncbi.nlm.nih.gov/12637292/.

[68] Brian T. Hawkins and Thomas P. Davis. The blood-brain barrier/neurovascular unit in health and disease. *Pharmacological Reviews*, 57(2):173–185, 2005. ISSN 00316997. doi: 10.1124/pr.57.2.4. URL https://pubmed.ncbi.nlm.nih.gov/15914466/.

[69] Aravinthan Varatharaj and Ian Galea. The blood-brain barrier in systemic inflammation. *Brain, Behavior, and Immunity*, 60:1–12, 2017. ISSN 10902139. doi: 10.1016/j.bbi.2016.03.010. URL https://pubmed.ncbi.nlm.nih.gov/26995317/.

[70] Stéphanie Debette and H. S. Markus. The clinical importance of white matter hyperintensities on brain magnetic resonance imaging: Systematic review and meta-analysis. *British Medical Journal*, 341(7767):288, Aug 2010. ISSN 17561833. doi: 10.1136/bmj.c3666. URL https://pubmed.ncbi.nlm.nih.gov/20660506/.

[71] Leonardo Pantoni. Pathophysiology of Age-Related Cerebral White Matter Changes. *Cerebrovascular Diseases*, 13(2):7–10, 2002. ISSN 1015-9770. doi: 10.1159/000049143. URL https://pubmed.ncbi.nlm.nih.gov/11901236/.

[72] P. C. Lauterbur. Image formation by induced local interactions: Examples employing nuclear magnetic resonance. *Nature*, 1973. ISSN 00280836. doi: 10.1038/242190a0. URL https://pubmed.ncbi.nlm.nih.gov/2663289/.

[73] W. S. Hinshaw, P. A. Bottomley, and G. N. Holland. Radiographic thin-section image of the human wrist by nuclear magnetic resonance. *Nature*, 270(5639):722–723, 1977. ISSN 00280836. doi: 10.1038/270722a0. URL https://pubmed.ncbi.nlm.nih.gov/593393/.

[74] Greg J. Stanisz, Ewa E. Odrobina, Joseph Pun, Michael Escaravage, Simon J. Graham, Michael J. Bronskill, and R. Mark Henkelman. T1, T2 relaxation and magnetization transfer in tissue at 3T. *Magnetic Resonance in Medicine*, 54(3):507–512, 2005. ISSN 07403194. doi: 10.1002/mrm.20605. URL https://www.ncbi.nlm.nih.gov/pubmed/16086319.

[75] Jorge Zavala Bojorquez, Stéphanie Bricq, Clement Acquitter, François Brunotte, Paul M. Walker, and Alain Lalande. What are normal relaxation times of tissues at 3 T? *Magnetic Resonance Imaging*, 35:69–80, 2017. ISSN 18735894. doi: 10.1016/j.mri.2016.08.021. URL https://www.ncbi.nlm.nih.gov/pubmed/27594531.

[76] Scott T. Brady and George J. Siegel. *Characteristic composition of myelin*. Lippincott-Raven, 2012. ISBN 0123749476. URL https://www.ncbi.nlm.nih.gov/books/NBK28221/.

[77] Elizabeth R. Sowell, Bradley S. Peterson, Paul M. Thompson, Suzanne E Welcome, Amy L. Henkenius, and Arthur W. Toga. Mapping cortical change across the human life span. *Nature Neuroscience*, 6(3):309–315, 2003. ISSN 10976256. doi: 10.1038/nn1008. URL https://www.ncbi.nlm.nih.gov/pubmed/15271264.

[78] Rachael I Scahill, Chris Frost, Rhian Jenkins, Jennifer L Whitwell, Martin N Rossor, and Nick C Fox. A longitudinal study of brain volume changes in normal aging using serial registered magnetic resonance imaging. *Archives of Neurology*, 60(7):989–994, 2003. ISSN 00039942. doi: 10.1001/archneur.60.7.989. URL https://www.ncbi.nlm.nih.gov/pubmed/12873856.

[79] Mustapha Bouhrara, David A Reiter, Christopher M Bergeron, Linda M Zukley, Luigi Ferrucci, Susan M Resnick, and Richard G Spencer. Evidence of demyelination in mild cognitive impairment and dementia using a direct and specific magnetic resonance imaging measure of myelin content. *Alzheimer's and Dementia*, 14(8):998–1004, 2018. ISSN 15525279. doi: 10.1016/j.jalz.2018.03.007. URL https://www.ncbi.nlm.nih.gov/pubmed/29679574.

[80] Heather S. Spader, Douglas C. Dean, W. Curt LaFrance, Neha P. Raukar, G. Rees Cosgrove, Stephanie A. Eyerly-Webb, Anna Ellermeier, Stephen Correia, Sean C.L. Deoni, and Jeffrey Rogg. Prospective study of myelin water fraction changes after mild traumatic brain injury in collegiate contact sports. *Journal of Neurosurgery*, 130(4): 1321–1329, Apr 2019. ISSN 19330693. doi: 10.3171/2017.12.JNS171597. URL https://www.ncbi.nlm.nih.gov/pubmed/29712487.

[81] E. H. Kolodny. Dysmyelinating and demyelinating conditions in infancy. *Current Opinion in Neurology and Neurosurgery*, 1993. ISSN 09517383. URL https://pubmed.ncbi.nlm.nih.gov/8507907/.

[82] Alex L. MacKay and Cornelia Laule. Magnetic Resonance of Myelin Water: An in vivo Marker for Myelin. *Brain Plasticity*, 2(1):71–91, 2016. ISSN 22136304. doi: 10.3233/bpl-160033. URL https://www.ncbi.nlm.nih.gov/pubmed/29765849.

[83] Alex Mackay, Kenneth Whittall, Julian Adler, David Li, Donald Paty, and Douglas Graeb. In vivo visualization of myelin water in brain by magnetic resonance. *Magnetic Resonance in Medicine*, 1994. ISSN 15222594. doi: 10.1002/mrm.1910310614. URL https://pubmed.ncbi.nlm.nih.gov/29765849/.

[84] Dosik Hwang, Dong Hyun Kim, and Yiping P. Du. In vivo multi-slice mapping of myelin water content using T2* decay. *NeuroImage*, 2010. ISSN 10538119.

doi: 10.1016/j.neuroimage.2010.04.023. URL https://pubmed.ncbi.nlm.nih.gov/20398770/.

[85] Matthew F. Glasser and David C. van Essen. Mapping human cortical areas in vivo based on myelin content as revealed by T1- and T2-weighted MRI. *Journal of Neuroscience*, 2011. ISSN 02706474. doi: 10.1523/JNEUROSCI.2180-11.2011. URL https://pubmed.ncbi.nlm.nih.gov/21832190/.

[86] Joon Yul Choi, In Hye Jeong, Se Hong Oh, Chang Hyun Oh, Na Young Park, Ho Jin Kim, and Jongho Lee. Evaluation of Normal-Appearing White Matter in Multiple Sclerosis Using Direct Visualization of Short Transverse Relaxation Time Component (ViSTa) Myelin Water Imaging and Gradient Echo and Spin Echo (GRASE) Myelin Water Imaging. *Journal of Magnetic Resonance Imaging*, 49(4):1091–1098, 2019. ISSN 15222586. doi: 10.1002/jmri.26278. URL https://www.ncbi.nlm.nih.gov/pubmed/30240519.

[87] Zhe Wu, Berkin Bilgic, Hongjian He, Qiqi Tong, Yi Sun, Yiping Du, Kawin Setsompop, and Jianhui Zhong. Wave-CAIPI ViSTa: highly accelerated whole-brain direct myelin water imaging with zero-padding reconstruction. *Magnetic Resonance in Medicine*, 80(3):1061–1073, 2018. ISSN 15222594. doi: 10.1002/mrm.27108. URL https://www.ncbi.nlm.nih.gov/pubmed/29388254.

[88] Sean C.L. Deoni, Brian K. Rutt, Tarunya Arun, Carlo Pierpaoli, and Derek K. Jones. Gleaning multicomponent T1 and T2 information from steady-state imaging data. *Magnetic Resonance in Medicine*, 60(6):1372–1387, Dec 2008. ISSN 07403194. doi: 10.1002/mrm.21704. URL https://www.ncbi.nlm.nih.gov/pubmed/19025904.

[89] Cornelia Laule, Piotr Kozlowski, Esther Leung, David K.B. Li, Alex L. MacKay, and G. R.Wayne Moore. Myelin water imaging of multiple sclerosis at 7 T: Correlations with histopathology. *NeuroImage*, 40(4):1575–1580, 2008. ISSN 10538119. doi: 10.

1016/j.neuroimage.2007.12.008. URL https://www.ncbi.nlm.nih.gov/pubmed/18321730.

[90] S. A. Montgomery and M. Asberg. A new depression scale designed to be sensitive to change. *British Journal of Psychiatry*, 134(4):382–389, Apr 1979. ISSN 00071250. doi: 10.1192/bjp.134.4.382. URL https://www.ncbi.nlm.nih.gov/pubmed/444788.

[91] Nathan Herrmann, S. E. Black, J Lawrence, C Szekely, and J. P. Szalai. The Sunnybrook stroke study a prospective study of depressive symptoms and functional outcome. *Stroke*, 29(3):618–624, 1998. ISSN 00392499. doi: 10.1161/01.STR.29.3.618. URL https://pubmed.ncbi.nlm.nih.gov/9506602/.

[92] Marie Delacre, Daniël Lakens, and Christophe Leys. Why psychologists should by default use welch's t-Test instead of student's t-Test. *International Review of Social Psychology*, 30(1):92–101, 2017. ISSN 23978570. doi: 10.5334/irsp.82. URL https://www.rips-irsp.com/articles/10.5334/irsp.82/.

[93] Adam Hampshire, Roger R. Highfield, Beth L. Parkin, and Adrian M. Owen. Fractionating Human Intelligence. *Neuron*, 76(6):1225–1237, Dec 2012. ISSN 08966273. doi: 10.1016/j.neuron.2012.06.022. URL https://www.ncbi.nlm.nih.gov/pubmed/23259956.

[94] Kimia Honarmand, Sabhyata Malik, Conor Wild, Laura E. Gonzalez-Lara, Christopher W. McIntyre, Adrian M. Owen, and Marat Slessarev. Feasibility of a web-based neurocognitive battery for assessing cognitive function in critical illness survivors. *PLoS ONE*, 14(4), Apr 2019. ISSN 19326203. doi: 10.1371/journal.pone.0215203. URL https://www.ncbi.nlm.nih.gov/pubmed/30978210.

[95] Carlos Leiva-Salinas and Max Wintermark. Imaging of acute ischemic stroke. *Neuroimaging Clinics of North America*, 20(4):455–468, Nov 2010. ISSN 10525149.

doi: 10.1016/j.nic.2010.07.002. URL https://www.ncbi.nlm.nih.gov/pubmed/20974371.

[96] John P. Mugler and James R. Brookeman. Three-dimensional magnetization-prepared rapid gradient-echo imaging (3D MP RAGE). *Magnetic Resonance in Medicine*, 15 (1):152–157, 1990. ISSN 15222594. doi: 10.1002/mrm.1910150117. URL https://pubmed.ncbi.nlm.nih.gov/2374495/.

[97] Sho Koyasu, Mami Iima, Shigeaki Umeoka, Nobuko Morisawa, David A. Porter, Juichi Ito, Denis Le Bihan, and Kaori Togashi. The clinical utility of reduced-distortion readout-segmented echo-planar imaging in the head and neck region: initial experience. *European Radiology*, 24(12):3088–3096, 2014. ISSN 14321084. doi: 10.1007/s00330-014-3369-5. URL https://pubmed.ncbi.nlm.nih.gov/25117744/.

[98] Jin Woo Choi, Hong Gee Roh, Won-Jin Moon, Young Il Chun, and Chung Hwan Kang. Optimization of MR Parameters of 3D TOF-MRA for Various Intracranial Stents at 3.0T MRI. *Neurointervention*, 6(2):71, Sep 2011. ISSN 20939043. doi: 10.5469/neuroint.2011.6.2.71. URL https://www.ncbi.nlm.nih.gov/pubmed/22125752.

[99] Joseph V. Hajnal, David J. Bryant, Larry Kasuboski, Pradip M. Pattany, Beatrice De Coene, Paul D. Lewis, Jacqueline M. Pennock, Angela Oatridge, Ian R. Young, and Graeme M. Bydder. Use of fluid attenuated inversion recovery (Flair) pulse sequences in mri of the brain. *Journal of Computer Assisted Tomography*, 16(6):841–844, 1992. ISSN 15323145. doi: 10.1097/00004728-199211000-00001. URL https://pubmed.ncbi.nlm.nih.gov/1430427/.

[100] F. Fazekas, J. B. Chawluk, and A. Alavi. MR signal abnormalities at 1.5 T in Alzheimer's dementia and normal aging. *American Journal of Roentgenology*, 149 (2):351–356, 1987. ISSN 15463141. doi: 10.2214/ajr.149.2.351. URL https://www.ncbi.nlm.nih.gov/pubmed/3496763.

[101] Ah Ling Cheng, Saima Batool, Cheryl R. McCreary, M. L. Lauzon, Richard Frayne, Mayank Goyal, and Eric E. Smith. Susceptibility-weighted imaging is more reliable than T2*-weighted gradient-recalled echo mri for detecting microbleeds. *Stroke*, 44(10): 2782–2786, 2013. ISSN 00392499. doi: 10.1161/STROKEAHA.113.002267. URL https://pubmed.ncbi.nlm.nih.gov/23920014/.

[102] Chris Rorden and Matthew Brett. Stereotaxic display of brain lesions. *Behavioural Neurology*, 12(4):191–200, 2000. ISSN 09534180. doi: 10.1155/2000/421719. URL https://pubmed.ncbi.nlm.nih.gov/11568431/.

[103] Andriy Fedorov, Reinhard Beichel, Jayashree Kalpathy-Cramer, Julien Finet, Jean Christophe Fillion-Robin, Sonia Pujol, Christian Bauer, Dominique Jennings, Fiona Fennessy, Milan Sonka, John Buatti, Stephen Aylward, James V. Miller, Steve Pieper, and Ron Kikinis. 3D Slicer as an image computing platform for the Quantitative Imaging Network. *Magnetic Resonance Imaging*, 30(9):1323–1341, 2012. ISSN 0730725X. doi: 10.1016/j.mri.2012.05.001. URL https://www.ncbi.nlm.nih.gov/pmc/articles/PMC3466397/.

[104] Tobias C. Wood. QUIT: QUantitative Imaging Tools. *Journal of Open Source Software*, 3(26):656, 2018. ISSN 24759066. doi: 10.21105/joss.00656. URL https://github.com/spinicist/QUIT.

[105] Stephen M. Smith. Fast robust automated brain extraction. *Human Brain Mapping*, 17(3):143–155, Nov 2002. ISSN 10659471. doi: 10.1002/hbm.10062. URL https://pubmed.ncbi.nlm.nih.gov/12391568/.

[106] Mark Jenkinson, Christian F Beckmann, Timothy E J Behrens, Mark W Woolrich, and Stephen M Smith. FSL - Review. *NeuroImage*, 62(2):782–90, 2012. ISSN 1095-9572. doi: 10.1016/j.neuroimage.2011.09.015. URL http://www.ncbi.nlm.nih.gov/pubmed/21979382.

[107] Yongyue Zhang, Michael Brady, and Stephen Smith. Segmentation of brain MR images through a hidden Markov random field model and the expectation-maximization algorithm. *IEEE Transactions on Medical Imaging*, 20(1):45–57, 2001. ISSN 02780062. doi: 10.1109/42.906424. URL https://pubmed.ncbi.nlm.nih.gov/11293691/.

[108] Sean C.L. Deoni, Brian K Rutt, and Terry M Peters. Rapid combined T1 and T2 mapping using gradient recalled acquisition in the steady state. *Magnetic Resonance in Medicine*, 49(3):515–526, 2003. ISSN 07403194. doi: 10.1002/mrm.10407. URL https://www.ncbi.nlm.nih.gov/pubmed/12594755.

[109] Jean David Jutras, Keith Wachowicz, and Nicola De Zanche. Analytical corrections of banding artifacts in driven equilibrium single pulse observation of T2 (DESPOT2). *Magnetic Resonance in Medicine*, 76(6):1790–1804, Dec 2016. ISSN 15222594. doi: 10.1002/mrm.26074. URL https://www.ncbi.nlm.nih.gov/pubmed/26714609.

[110] Sean C.L. Deoni. Transverse relaxation time (T2) mapping in the brain with off-resonance correction using phase-cycled steady-state free precession imaging. *Journal of Magnetic Resonance Imaging*, 30(2):411–417, Aug 2009. ISSN 10531807. doi: 10.1002/jmri.21849. URL https://pubmed.ncbi.nlm.nih.gov/19629970/.

[111] Daniel J. West, Rui P.A.G. Teixeira, Tobias C. Wood, Joseph V. Hajnal, Jacques Donald Tournier, and Shaihan J. Malik. Inherent and unpredictable bias in multi-component DESPOT myelin water fraction estimation. *NeuroImage*, 195:78–88, Jul 2019. ISSN 10959572. doi: 10.1016/j.neuroimage.2019.03.049. URL https://www.ncbi.nlm.nih.gov/pubmed/30930311.

[112] Sean C.L. Deoni, Lucy Matthews, and Shannon H. Kolind. One component? Two components? Three? the effect of including a nonexchanging "free" water component in multicomponent driven equilibrium single pulse observation of T1 and T2. *Magnetic*

Resonance in Medicine, 70(1):147–154, 2013. ISSN 07403194. doi: 10.1002/mrm.24429. URL https://pubmed.ncbi.nlm.nih.gov/22915316/.

[113] Sean C.L. Deoni and Shannon H. Kolind. Investigating the stability of mcDESPOT myelin water fraction values derived using a stochastic region contraction approach. *Magnetic Resonance in Medicine*, 73(1):161–169, Jan 2015. ISSN 15222594. doi: 10.1002/mrm.25108. URL https://pubmed.ncbi.nlm.nih.gov/24464472/.

[114] Bruce Fischl. FreeSurfer. *NeuroImage*, 62(2):774–781, Aug 2012. ISSN 10538119. doi: 10.1016/j.neuroimage.2012.01.021. URL https://pubmed.ncbi.nlm.nih.gov/22248573/.

[115] Andreas Glatz, Maria C. Valdés Hernández, Alexander J. Kiker, Mark E. Bastin, Ian J. Deary, and Joanna M. Wardlaw. Characterization of multifocal T2*-weighted MRI hypointensities in the basal ganglia of elderly, community-dwelling subjects. *NeuroImage*, 82:470–480, Nov 2013. ISSN 10538119. doi: 10.1016/j.neuroimage.2013.06.013. URL https://pubmed.ncbi.nlm.nih.gov/23769704/.

[116] John T. O'Brien, Timo Erkinjuntti, Barry Reisberg, Gustavo Roman, Tohru Sawada, Leonardo Pantoni, John V. Bowler, Clive Ballard, Charles DeCarli, Philip B. Gorelick, Kenneth Rockwood, Alistair Burns, Serge Gauthier, and Steven T. DeKosky. Vascular cognitive impairment. *Lancet Neurology*, 2(2):89–98, Feb 2003. ISSN 14744422. doi: 10.1016/S1474-4422(03)00305-3. URL https://pubmed.ncbi.nlm.nih.gov/12849265/.

[117] Hong Zhou, Wanjun Lu, Yongmei Shi, Feng Bai, Jinghao Chang, Yonggui Yuan, Gaojun Teng, and Zhijun Zhang. Impairments in cognition and resting-state connectivity of the hippocampus in elderly subjects with type 2 diabetes. *Neuroscience Letters*, 473(1):5–10, Mar 2010. ISSN 03043940. doi: 10.1016/j.neulet.2009.12.057. URL https://pubmed.ncbi.nlm.nih.gov/20123114/.

[118] E. Kövari, G. Gold, F. R. Herrmann, A. Canuto, P. R. Hof, C. Bouras, and P. Giannakopoulos. Cortical microinfarcts and demyelination affect cognition in cases at high risk for dementia. *Neurology*, 68(12):927–931, Mar 2007. ISSN 00283878. doi: 10.1212/01.wnl.0000257094.10655.9a. URL https://pubmed.ncbi.nlm.nih.gov/17372128/.

[119] Statistics Canada. Canadian community health survey: Mental Health. *The Daily*, 2013. URL https://www150.statcan.gc.ca/n1/dai-quo/index-eng.htm.

[120] Giovanna Meloni, Anna Proia, Giovanni Antonini, C. De Lena, V. Guerrisi, S. Capria, S. Maria Trisolini, G. Ferrazza, G. Sideri, and F. Mandelli. Thrombotic thrombocytopenic purpura: Prospective neurologic, neuroimaging and neurophysiologic evaluation. *Haematologica*, 86(11):1194–1199, 2001. ISSN 03906078. URL https://pubmed.ncbi.nlm.nih.gov/11694406/.

[121] Nariman Noorbakhsh-Sabet and Ramin Zand. Thrombotic Thrombocytopenic Purpura with Concomitant Progressive Cerebral Microbleeds. *Journal of Stroke and Cerebrovascular Diseases*, 25(11):e214–e215, Nov 2016. ISSN 15328511. doi: 10.1016/j.jstrokecerebrovasdis.2016.08.037. URL https://pubmed.ncbi.nlm.nih.gov/27693106/.

[122] Ah Park Sun, Kyeong Lee Tae, Bum Sung Ki, and Kyu Park Sung. Extensive brain stem lesions in thrombotic thrombocytopenic purpura: Repeat magnetic resonance findings. *Journal of Neuroimaging*, 15(1):79–81, Jan 2005. ISSN 10512284. doi: 10.1177/1051228404269491. URL https://pubmed.ncbi.nlm.nih.gov/15574579/.

[123] Mustapha Bouhrara, Abinand C. Rejimon, Luis E. Cortina, Nikkita Khattar, Christopher M. Bergeron, Luigi Ferrucci, Susan M. Resnick, and Richard G. Spencer. Adult brain aging investigated using BMC mcDESPOT based myelin water fraction imaging.

Neurobiology of Aging, 2020. ISSN 15581497. doi: 10.1016/j.neurobiolaging.2019.10.003. URL https://pubmed.ncbi.nlm.nih.gov/31735379/.

[124] Jongho Lee, Jae Won Hyun, Jieun Lee, Eun Jung Choi, Hyeong Geol Shin, Kyeongseon Min, Yoonho Nam, Ho Jin Kim, and Se Hong Oh. So You Want to Image Myelin Using MRI: An Overview and Practical Guide for Myelin Water Imaging. *Journal of Magnetic Resonance Imaging*, 2020. ISSN 15222586. doi: 10.1002/jmri.27059. URL https://pubmed.ncbi.nlm.nih.gov/32009271/.

[125] S. Groeschel, B. Vollmer, M. D. King, and A. Connelly. Developmental changes in cerebral grey and white matter volume from infancy to adulthood. *International Journal of Developmental Neuroscience*, 28(6):481–489, Oct 2010. ISSN 07365748. doi: 10.1016/j.ijdevneu.2010.06.004. URL https://pubmed.ncbi.nlm.nih.gov/20600789/.

[126] Burkhard Mädler, Sylvia A Drabycz, Shannon H Kolind, Kenneth P Whittall, and Alexander L. MacKay. Is diffusion anisotropy an accurate monitor of myelination? Correlation of multicomponent T2 relaxation and diffusion tensor anisotropy in human brain. *Magnetic Resonance Imaging*, 26(7):874–888, 2008. ISSN 0730725X. doi: 10.1016/j.mri.2008.01.047. URL https://www.ncbi.nlm.nih.gov/pubmed/18524521.

[127] J. C. Ferré, E. Bannier, H. Raoult, G. Mineur, B. Carsin-Nicol, and J. Y. Gauvrit. Arterial spin labeling (ASL) perfusion: Techniques and clinical use. *Diagnostic and Interventional Imaging*, 94(12):1211–1223, 2013. ISSN 22115684. doi: 10.1016/j.diii.2013.06.010. URL https://pubmed.ncbi.nlm.nih.gov/23850321/.

[128] Joachim Lotz, Christian Meier, Andreas Leppert, and Michael Galanski. Cardiovascular flow measurement with phase-contrast MR imaging: Basic facts and implementation. *Radiographics*, 22(3):651–671, 2002. ISSN 02715333. doi: 10.1148/radiographics.22.3.g02ma11651. URL https://www.ncbi.nlm.nih.gov/pubmed/12006694.

[129] Krishna S. Nayak, Jon Fredrik Nielsen, Matt A. Bernstein, Michael Markl, Peter D. Gatehouse, Rene M. Botnar, David Saloner, Christine Lorenz, Han Wen, Bob S. Hu, Frederick H. Epstein, John N. Oshinski, and Subha V. Raman. Cardiovascular magnetic resonance phase contrast imaging. *Journal of Cardiovascular Magnetic Resonance*, 17 (1), Aug 2015. ISSN 1532429X. doi: 10.1186/s12968-015-0172-7. URL https://www.ncbi.nlm.nih.gov/pubmed/26254979.

[130] David C. Alsop, John A. Detre, Xavier Golay, Matthias Günther, Jeroen Hendrikse, Luis Hernandez-Garcia, Hanzhang Lu, Bradley J. Macintosh, Laura M. Parkes, Marion Smits, Matthias J.P. Van Osch, Danny J.J. Wang, Eric C. Wong, and Greg Zaharchuk. Recommended implementation of arterial spin-labeled Perfusion mri for clinical applications: A consensus of the ISMRM Perfusion Study group and the European consortium for ASL in dementia. *Magnetic Resonance in Medicine*, 73(1):102–116, Jan 2015. ISSN 15222594. doi: 10.1002/mrm.25197. URL https://www.ncbi.nlm.nih.gov/pubmed/24715426.

[131] Hui Zhang, Torben Schneider, Claudia A. Wheeler-Kingshott, and Daniel C. Alexander. NODDI: Practical in vivo neurite orientation dispersion and density imaging of the human brain. *NeuroImage*, 61(4):1000–1016, Jul 2012. ISSN 10538119. doi: 10.1016/j.neuroimage.2012.03.072. URL https://www.ncbi.nlm.nih.gov/pubmed/22484410.

[132] Sjoerd J Finnema, Nabeel B Nabulsi, Tore Eid, Kamil Detyniecki, Shu Fei Lin, Ming Kai Chen, Roni Dhaher, David Matuskey, Evan Baum, Daniel Holden, Dennis D Spencer, Joël Mercier, Jonas Hannestad, Yiyun Huang, and Richard E Carson. Imaging synaptic density in the living human brain. *Science Translational Medicine*, 8(348), 2016. ISSN 19466242. doi: 10.1126/scitranslmed.aaf6667. URL https://pubmed.ncbi.nlm.nih.gov/27440727/.

[133] Romina Mizrahi, Pablo M Rusjan, James Kennedy, Bruce Pollock, Benoit Mulsant,

Ivonne Suridjan, Vincenzo De Luca, Alan A Wilson, and Sylvain Houle. Translocator protein (18 kDa) polymorphism (rs6971) explains in-vivo brain binding affinity of the PET radioligand [18F]-FEPPA. *Journal of Cerebral Blood Flow and Metabolism*, 32 (6):968–972, 2012. ISSN 0271678X. doi: 10.1038/jcbfm.2012.46. URL https://pubmed.ncbi.nlm.nih.gov/22472607/.

[134] Ronald Boellaard, Mike J. O'Doherty, Wolfgang A Weber, Felix M Mottaghy, Markus N Lonsdale, Sigrid G Stroobants, Wim J.G. Oyen, Joerg Kotzerke, Otto S. Hoekstra, Jan Pruim, Paul K Marsden, Klaus Tatsch, Corneline J Hoekstra, Eric P Visser, Bertjan Arends, Fred J Verzijlbergen, Josee M Zijlstra, Emile F.I. Comans, Adriaan A Lammertsma, Anne M Paans, Antoon T Willemsen, Thomas Beyer, Andreas Bockisch, Cornelia Schaefer-Prokop, Dominique Delbeke, Richard P Baum, Arturo Chiti, and Bernd J Krause. FDG PET and PET/CT: EANM procedure guidelines for tumour PET imaging: Version 1.0. *European Journal of Nuclear Medicine and Molecular Imaging*, 37(1):181–200, 2010. ISSN 16197070. doi: 10.1007/s00259-009-1297-4. URL https://pubmed.ncbi.nlm.nih.gov/19915839/.

[135] Ziad S. Nasreddine, Natalie A. Phillips, Valérie Bédirian, Simon Charbonneau, Victor Whitehead, Isabelle Collin, Jeffrey L. Cummings, and Howard Chertkow. The Montreal Cognitive Assessment, MoCA: A brief screening tool for mild cognitive impairment. *Journal of the American Geriatrics Society*, 53(4):695–699, Apr 2005. ISSN 15325415. doi: 10.1111/j.1532-5415.2005.53221.x. URL https://pubmed.ncbi.nlm.nih.gov/15817019/.

Study Approval

Western Research

Date: 1 August 2018

To: Dr. Susan Huang

Project ID: 108273

Study Title: A Prospective Study on the Long-Term Vascular Burden in TTP Patients

Application Type: Continuing Ethics Review (CER) Form

Review Type: Delegated

REB Meeting Date: 21/Aug/2018

Date Approval Issued: 01/Aug/2018

REB Approval Expiry Date: 30/Aug/2019

Dear Dr. Susan Huang,

The Western University Research Ethics Board has reviewed the application. This study, including all currently approved documents, has been re-approved until the expiry date noted above.

REB members involved in the research project do not participate in the review, discussion or decision.

Western University REB operates in compliance with, and is constituted in accordance with, the requirements of the TriCouncil Policy Statement: Ethical Conduct for Research Involving Humans (TCPS 2); the International Conference on Harmonisation Good Clinical Practice Consolidated Guideline (ICH GCP); Part C, Division 5 of the Food and Drug Regulations; Part 4 of the Natural Health Products Regulations; Part 3 of the Medical Devices Regulations and the provisions of the Ontario Personal Health Information Protection Act (PHIPA 2004) and its applicable regulations. The REB is registered with the U.S. Department of Health & Human Services under the IRB registration number IRB 00000940.

Please do not hesitate to contact us if you have any questions.

Sincerely,

Daniel Wyzynski, Research Ethics Coordinator, on behalf of Dr. Joseph Gilbert, HSREB Chair

Note: This correspondence includes an electronic signature (validation and approval via an online system that is compliant with all regulations).

Vita

Name:	Jeffrey Hamilton
Post-Secondary Education:	B.Sc. (Hons) Biology (2018) McGill University, Montreal, QC
Honours and Awards:	Western Certificate in University Teaching and Learning (2020) Western University, London, ON
Graduate Coursework:	*Biophysics Graduate Seminars* (MBP 9700) *Preparing for Scientific Research* (MBP 9513A) *Conceptual MRI* (MBP 9650A) *Preparing for Scientific Review* (MBP 9514A) *Inferencing from Data Analysis* (MBP 9522B) *The Theory and Practice of University Teaching* (SGPS 9500B)
Work Experience:	Graduate Teaching Assistant (2019) Western University *Applied Mathematics for Engineers I* (AM 1413B) *Biology for Sciences I* (Biology 1001A)
Volunteer Experience:	Let's Talk Sciences Volunteer (2019–2020) Lawon's Talks on Mondays Co-Coordinator (2019–2020)
First Author Poster Presentations:	Chronic neurological impairment in patients with TTP J.G. Hamilton, M.T. Jurkiewicz, J.D. Thiessen, and S.H.S. Huang *American Society of Nephrology Kidney Week* 2020 MRI to investigate neurological complications in patients with TTP J.G. Hamilton, M.T. Jurkiewicz, J.D. Thiessen, and S.H.S. Huang *Imaging Network Ontario* 2020 From CT to MRI: imaging chronic neurological impairment in patients with TTP J.G. Hamilton, T.Y. Lee, J.D. Thiessen, and S.H.S. Huang *Imaging Network Ontario* 2019